NUMERICAL SIMULATION OF SHOCK/CAVITATION-STRUCTURE INTERACTION

HO JIN YEE REBECCA
(B. Eng. (Hons.), NUS)

A THESIS SUBMITTED

FOR THE DEGREE OF MASTER OF ENGINEERING

DEPARTMENT OF MECHANICAL ENGINEERING

NATIONAL UNIVERSITY OF SINGAPORE

2005

Acknowledgement

The author would like to thank her supervisors A/Prof. B. C. Khoo and Dr. Liu Tiegang for their guidance and support during the course of the work, particularly Dr. Liu who has contributed tremendously to the discussions on the mathematical derivations. The author would also like to thank Mr Xie Wenfeng for his guidance in the project and Ms. Serena Tan for her recommendations in solid mechanics.

Last but not least, the author would like to thank her husband and family for their support in the duration of this course.

Table of Contents

Title Page i

Acknowledgement ii

Table of Contents iii

Nomenclature vi

List of Tables ix

List of Figures x

Summary xv

Chapter 1 Introduction 1

1.1 Fluid-Structure Interaction 1

1.2 Objectives and Organizational Structure of this work 2

Chapter 2 Background on Previous Work 3

2.1 Compressible fluid medium 3

2.2 The shock tube problem 5

2.3 One-Fluid and two-fluid continuum 6

2.4 Unsteady Cavitation 7

2.5 Interface tracking methods 9

2.6 Eulerian vs Lagrangian 11

2.7 Naviers Equation vs other solid EOS 12

Chapter 3 Methodology:1D System 14

3.1 1D Planar Euler equations 14

3.2 1D Naviers Equation 15

3.3 Level-set method for Interface 19

3.4 Ghost Fluid Method 20

3.5 Riemann solver at the interface 22

3.5.1 Fluid Characteristic Equations 23

3.5.2 Solid Characteristic Equations 24

3.6 Numerical solver 26

3.6.1 Numerical solver for fluid media 26

3.6.2 Numerical solver for solid media 27

3.6.3 Computational Procedures 30

3.7 Analytical Solution 31

3.7.1 Fluid-Solid(shock-shock) 31

3.7.2 Fluid-Solid(Rarefaction-Shock) 36

3.7.3 Fluid-solid(Rarefraction-rarefraction) 39

Chapter 4 Results and Discussion 40

4.1 Test cases 40

4.1.1 Properties of metal 40

4.2 Test cases in comparison with published results 41

4.3 Non Reflection test cases 43

4.4 Other test cases involving gas-solid compressible flows 44

4.5 Other test cases involving water-solid compressible flows 45

4.6 Mesh Refinement test 47

4.7 Water shock tube test 47

Chapter 5 2-D Naviers Equation 71

5.1 General Formulation 71

5.2 Specific 2-D formulation 72

Chapter 6 Conclusion and Future Directions 81

6.1 Conclusion 81

6.2 Future directions 83

References **84**

Nomenclature

English Alphabets:

A	coefficient matrix $\partial F(U)/\partial U$
a	speed of sound in gas
$\bar{a}$	speed of sound in water
B	constant in Tait's equation of state for water
	$\partial G(U)/\partial U$
c	speed of sound in gas, water or solid medium
CFL	CFL number
d, D	derivative operator
E	total flow energy
	Young's modulus
e	Strain
F	inviscid flow flux in the x or radial direction
G	inviscid flow flux in the y direction
H	numerical flux
I	interface position
L	left eigenvector
M	total grid points in the x or radial direction
N	constant in Tait's equation of state for water
P	flow pressure
$\bar{P}$	$P + B$
R	right eigenvector
R^{-1}	left eigenvector

S	source term in the 1D symmetric Euler equation
	Shock speed
t	temporal coordinate
u	flow velocity in the x or radial direction
U	conservative variable vector
V	flow velocity component in the y direction
x	x coordinate
y	y coordinate

Greek Alphabets:

α	longitudinal wave speed
β	shear wave speed
δ	dirac operator
ε	displacement
	very small number
ϕ	level-set distance function
γ	ratio of specific heats
Δ	quantity jump across a shock front
Δt	time step size
Δx	step size in the x direction
λ	$\Delta t/\Delta x$
	eigenvalue
	Lame constant
Λ	eigenvalue matrix
μ	Lame constant

υ	poisson ratio
ρ	flow density
σ	Stress in the solid
$\bar{\sigma}$	Stress vector

Superscript:

l	component index of a column vector
L	flux parameter indicator related to the left characteristic
R	flux parameter indicator related to the right characteristic
T	matrix transposition
n	temporal index

Subscript:

A,B	parameter associated with the coefficient matrices
i	spatial index in the x or radial direction
j	spatial index in the y direction
H	parameter associated with initial high-pressure region

List of Tables

Table 4.1	Properties of metals in imperial units at 20^0C	Pg 40
Table 4.2	Properties of metals in SI units at 20^0C	Pg 40
Table 4.3	Composition of AISI type 431 Steel	Pg 41

List of Figures

Fig. 2.1a	The x-t diagram of rarefraction wave	Pg 5
Fig. 2.1b	The diagram illustrating the Head and Tail of the rarefraction wave	Pg 5
Fig. 2.2	Illustration of the shock tube problem	Pg 6
Fig. 3.1	Illustration of fluid pressure(compressive stress) on solid medium	Pg 17
Fig. 3.2	Illustration of Original Ghost Fluid method without isobaric fixing	Pg 21
Fig. 3.3	Illustration of Original Ghost Fluid Method with isobaric fixing	Pg 22
Fig. 3.4	Illustration of Modified Ghost Fluid Method	Pg 23
Fig. 3.5	Ideal pressure, velocity and density plots in a shock-shock interaction	Pg 31
Fig. 3.6	Ideal pressure, velocity and density plots for a rarefraction-shock interaction	Pg 36
Fig. 4.1a	The distribution of pressure obtained for comparison against the analytical solution (Case 4.1 Gas-solid)	Pg 49
Fig. 4.1b	The distribution of velocity obtained for comparison against the analytical solution (Case 4.1 Gas-solid)	Pg 49
Fig. 4.1c	The distribution of density obtained for comparison against the analytical solution (Case 4.1 Gas-solid)	Pg 50
Fig. 4.1d	The distribution of pressure obtained for comparison between Naviers equation and Hydro-elasto-plastic models	Pg 50

Fig. 4.1e	The distribution of velocity obtained for comparison between Naviers equation and Hydro-elasto-plastic models	Pg 51
Fig. 4.1f	The distribution of density obtained for comparison between Naviers equation and Hydro-elasto-plastic models	Pg 51
Fig. 4.2a	The distribution of pressure obtained for comparison against the analytical solution (Case 4.2 Water-solid)	Pg 52
Fig. 4.2b	The distribution of velocity obtained for comparison against the analytical solution (Case 4.2 Water-solid)	Pg 52
Fig. 4.2c	The distribution of density obtained for comparison against the analytical solution (Case 4.2 Water-solid)	Pg 53
Fig. 4.2d	The distribution of pressure obtained for comparison between Naviers equation and Hydro-elasto-plastic models	Pg 53
Fig. 4.2e	The distribution of velocity obtained for comparison between Naviers equation and Hydro-elasto-plastic models	Pg 54
Fig. 4.2f	The distribution of density obtained for comparison between Naviers equation and Hydro-elasto-plastic models	Pg 54
Fig. 4.3a	The pressure profile for Case 4.3 Gas-Solid shock impedance problem	Pg 55
Fig. 4.3b	The velocity profile for Case 4.3 Gas-Solid shock-impedance problem	Pg 55
Fig. 4.3c	The density profile for Case 4.3 Gas-Solid shock-impedance problem	Pg 56
Fig. 4.4a	The pressure profile for Case 4.4 Water-Solid shock impedance problem	Pg 56

Fig. 4.4b	The velocity profile for Case 4.4 Water-Solid shock impedance problem	Pg 57
Fig. 4.4c	The density profile for Case 4.4 Water-Solid shock impedance problem	Pg 57
Fig. 4.5a	The distribution of pressure obtained for comparison against the analytical solution (Case 4.5 Gas-solid)	Pg 58
Fig. 4.5b	The distribution of velocity obtained for comparison against the analytical solution (Case 4.5 Gas-solid)	Pg 58
Fig. 4.5c	The distribution of density obtained for comparison against the analytical solution (Case 4.5 Gas-solid)	Pg 59
Fig. 4.6a	The distribution of pressure obtained for comparison against the analytical solution (Case 4.6 Gas-solid)	Pg 59
Fig. 4.6b	The distribution of velocity obtained for comparison against the analytical solution (Case 4.6 Gas-solid)	Pg 60
Fig. 4.6c	The distribution of density obtained for comparison against the analytical solution (Case 4.6 Gas-solid)	Pg 60
Fig. 4.7a	The distribution of pressure obtained for comparison against the analytical solution (Case 4.7 Gas-solid)	Pg 61
Fig. 4.7b	The distribution of velocity obtained for comparison against the analytical solution (Case 4.7 Gas-solid)	Pg 61
Fig. 4.7c	The distribution of density obtained for comparison against the analytical solution (Case 4.7 Gas-solid)	Pg 62
Fig. 4.8a	The distribution of pressure obtained for comparison against the analytical solution (Case 4.8 Water-solid)	Pg 62

Fig. 4.8b	The distribution of velocity obtained for comparison against the analytical solution (Case 4.8 Water-solid)	Pg 63
Fig. 4.8c	The distribution of density obtained for comparison against the analytical solution (Case 4.8 Water-solid)	Pg 63
Fig. 4.9a	The distribution of pressure obtained for comparison against the analytical solution (Case 4.9 Water-solid)	Pg 64
Fig. 4.9b	The distribution of velocity obtained for comparison against the analytical solution (Case 4.8 Water-solid)	Pg 64
Fig. 4.9c	The distribution of density obtained for comparison against the analytical solution (Case 4.8 Water-solid)	Pg 65
Fig. 4.10a	The distribution of pressure obtained for comparison against the analytical solution (Case 4.10 Water-solid)	Pg 65
Fig. 4.10b	The distribution of velocity obtained for comparison against the analytical solution (Case 4.9 Water-solid)	Pg 66
Fig. 4.10c	The distribution of density obtained for comparison against the analytical solution (Case 4.9 Water-solid)	Pg 66
Fig. 4.11a	The distribution of pressure obtained for comparison against the analytical solution (Case 4.11 Water-solid)	Pg 67
Fig. 4.11b	The distribution of velocity obtained for comparison against the analytical solution (Case 4.11 Water-solid)	Pg 67
Fig. 4.11c	The distribution of density obtained for comparison against the analytical solution (Case 4.11 Water-solid)	Pg 68
Fig. 4.12	Mesh refinement of the pressure profile for gas-solid (Mesh sizes: 2000, 4000, 8000)	Pg 68

Fig. 4.13	Mesh refinement of the pressure profile for water-solid (Mesh sizes: 2000, 4000, 8000)	Pg 69
Fig. 4.14	Schematic Diagram of water shock tube problem with steel	Pg 47
Fig. 4.14a	Pressure profile at the surface of the steel wall	Pg 69
Fig. 4.14b	Pressure profile at the rigid reflecting-end of tube (without steel)	Pg 70
Fig. 4.14c	Overlapping pressure plots for gas-water and gas-water-steel	Pg 70
Fig. 5.1a	Plane Stress	Pg 74
Fig. 5.1b	Plane Strain	Pg 74

Summary

In current literature, some of the EOS which are used to simulate solid behaviour include the Mie-Gruneisen EOS from Miller and Puckett (1996) and the hydro-elasto-plastic model by Tang and Sotiropoulos (1999). The Naviers equation is based on the theory of elasticity and is well-known in solid mechanics. It only involves two material parameters (Young modulus and Poisson Ratio) which can be found in most material handbooks, unlike the other EOS mentioned above. In this thesis, a novel approach was adopted in which the Naviers equation was used to simulate elastic solid behaviour when the elastic solid is coupled to compressible fluid media. The level-set method was used to track the fluid-solid interface movement and through the implementation of the Modified Ghost Fluid method, which calculates predicted interface values and ghost fluid status using an approximate Riemann solver, the interface boundary conditions could be maintained without specifying the interface position. Due to the nature of the Naviers equation, the mesh over the solid media has to be Lagrangian while the mesh remains Eulerian over the fluid media and in order to ensure stability, the smaller Lagrangian timestep was used. The numerical solver for the fluid medium was the high-order MUSCL scheme with a minmod limiter while for the solid medium, the second-order modified Harten's TVD MUSCL scheme with the incorporation of an artificial compression method(ACM) technique in the immediate region of shock/contact discontinuity from Liu et al. (1999) was applied. Using this method, we were able to capture the shock front over comparably fewer computational cells compared to the MUSCL scheme without ACM technique. As the coupling of the Naviers equation with the Euler equations in a finite difference approach is relatively new, we have also derived the 1D analytical solutions for various scenarios in order to

adequately compare the numerical results. From the non-reflection test cases of 4.3 and 4.4, there are no visible non-physical humps at the interface location, indicating the accuracy and robustness of the interface algorithm in transmitting the full strength of the shock from the left to right media. The 1D numerical solutions for most cases fit very well with the analytical solutions except for cases 4.7 and 4.11 where rarefraction waves occur in both media. Pressure undershoots are seen near the solid rarefraction wave in both test cases. It is suggested from Lin and Ballmann (1993a) that plasticity effects may need to be considered in modeling solid rarefraction waves. In case 4.14 which is similar to the 1D case study in Tang and Huang (1996), results from the gas-water-steel cavitation interaction show similar effects as Wardlaw et al. (2000) in the comparisons between deformable and rigid walls. It is noted that the pressure pulses drop to a lower mean value compared to the case with rigid boundary. Also, less number of cavitation zones were observed in the case with steel structure. In order to ensure compatibility with the Euler system, the Naviers equation in two dimensions has to be re-written in similar form. The formulation of the eigensystem of the re-written Naviers equation in two dimensions was achieved in this thesis.

Chapter 1 Introduction

1.1 Fluid-Structure Interaction

In many varied applications ranging from naval weapon design, naval ship/submarine structure, flow-induced vibration of underwater pipes, sloshing and impact of liquid on retaining structures, water hammer in pipes and many other problems, solving these fluid-structure interaction problems have required multi-disciplinary knowledge in fluid dynamics, solid dynamics and acoustics. Many models simulating the fluid-structure interaction have been proposed. Some of the models include a finite element formulation based on flow velocity model by Kochupillai et al. (2004) for waterhammer effect, and shock-cavitation-structure interaction using commercial GEMINI Euler equation solver-DYNA_N finite element solver coupled hydrocode by Wardlaw et al. (2000).

In Miller and Puckett (1996), they designed a second-order Godunov scheme for materials in condensed phases, i.e. liquids and solids in hydrostatic limit and the model used was based on the Mie-Gruneisen EOS and a linear Hugoniot. In Tang and Sotiropoulos (1999), the behavior of the solid structure was simulated using a hydro-elasto-plastic EOS with the ultimate purpose of computing the unsteady one-dimensional wave problems with fracture and cavitation in coupled solid-water-gas systems in which there are distinct interfaces between different phases. In Fedkiw (2002), springs with some stiffness were used to simulate the strength of a solid structure.

Most of the current studies have used various EOS to represent the unique characteristics of solids. The Naviers equations are differential equilibrium conditions which illustrate most aptly the elastic behaviour of isotropic, homogeneous solids and have been used to describe many solid mechanics problems. The Naviers equations

were also applied in the field of geophysics or more specifically, seismic modelling whereby various applications include surface wave noise analysis in oil and gas exploration (Cohen et al.(1991)).

1.2 Objectives and Organizational Structure of this work

In this work, we seek to develop a new finite difference model coupling the Euler equations for a compressible fluid with the Naviers equations simulating an elastic solid structure. In Chapter 2, we will discuss the background of the previous work done in this area followed by a discourse on the 1D methodology in Chapter 3. We will then validate our new model with other results in Chapter 4, and a discussion on the 2D methodology in Chapter 5. Last but not least, we will end this dissertation with some conclusions in Chapter 6 as well as discussion on possible future research areas.

Chapter 2 Background on Previous Work

2.1 Compressible fluid medium

In compressible fluid medium, a commonly used equation is the time-dependent Euler equations which are a system of non-linear hyperbolic conservation laws that govern the dynamics of a compressible fluid, such as gases or liquids at high pressures, for which the effects of body forces, viscous stresses and heat conductivity are neglected. In the various studies of compressible medium, discussions of shock waves, contact discontinuities and rarefraction waves are commonplace. Shock waves are small transition layers of very rapid changes of physical quantities such as pressure, density and temperature. In fact, they are solutions of the Rankine-Hugoniot relations with non-zero mass flow through the discontinuity. As a result, pressure and normal velocity undergo discontinuous variations while the tangential velocity remains continuous. A system of hyperbolic conservation laws is given as

$$U_t + F(U)_x = 0, \tag{2.1}$$

where $U = (\rho, \rho u, E)^T$, $F(U) = \left(\rho u, \rho u^2 + P, u(E+P)\right)^T$. Together with a discontinuous wave solution of speed S associated with the eigenvalue-characteristic field, the Rankine-Hugoniot condition states that

$$\Delta F = S\Delta U, \tag{2.2a}$$

$$\Delta U = U_R - U_L, \tag{2.2b}$$

$$\Delta F = F_R - F_L, \tag{2.2c}$$

$$F_L = F(U_L), \quad F_R = F(U_R), \tag{2.2d}$$

where *F* denotes the inviscid flow flux and U_L and U_R are the respective states immediately to the left and right of the discontinuity. In addition, the shock wave has to obey the entropy condition below as denoted in Toro (1997).

$$\lambda(u_L) > S > \lambda(u_R), \tag{2.3}$$

In other words, the shock wave speed has to be in-between the propagation speeds of the left and right states.

The contact discontinuity represents an interface across which both pressure and particle velocity are constant but density jumps discontinuously as do variables that depend on density such as specific internal energy, temperature, sound speed and entropy.

The various eigenvalues of the 1D Euler equations are $\lambda_1 = u - a$, $\lambda_2 = u$ or $\lambda_3 = u + a$ where *a* is the sound speed. The rarefraction wave is a smooth wave associated with $\lambda_1 = u - a$ and $\lambda_3 = u + a$ fields across which ρ, u and p change. The wave has a fan-type shape and is enclosed by two bounding characteristics corresponding to the Head and Tail of the wave as depicted in the figure below. Across the wave, the isentropic law applies below for a perfect gas and *s* here denotes the entropy and γ is the ratio of specific heat.

$$\int \frac{a}{\rho} d\rho = \frac{2a}{\gamma - 1}, \tag{2.4}$$

Hence, the characteristics inside the rarefraction wave are governed by these rules.

$$\left.\begin{array}{l} u + \dfrac{2a}{\gamma - 1} = cons\tan t \\ s = cons\tan t \end{array}\right\} across\ \lambda_1 = u - a, \tag{2.5a}$$

$$\left.\begin{array}{l} u - \dfrac{2a}{\gamma - 1} = cons\tan t \\ s = cons\tan t \end{array}\right\} across\ \lambda_3 = u + a, \tag{2.5b}$$

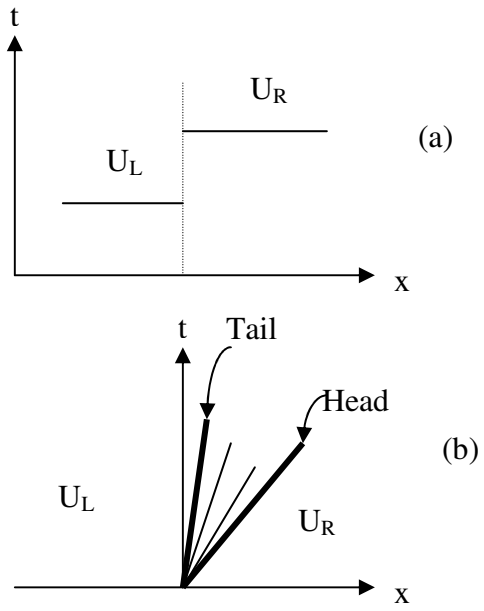

Figure 2-1 (a): x-t diagram of rarefraction wave, (b): Diagram illustrating the Head and Tail of the rarefraction wave

2.2 The shock tube problem

The shock tube problem as seen in Hirsch (1992), is an interesting and difficult test case since it presents an exact solution to the full system of one-dimensional Euler equations comprising at the same time, a shock wave, a contact discontinuity and a rarefraction wave. This problem, also called the Riemann problem, can be realized experimentally by the sudden removal of a diaphragm in a long one-dimensional tube separating two initial gas states at different pressures and densities. The initial conditions are

$$\begin{aligned} &u = u_L, \quad p = p_L, \quad \rho = \rho_L, \quad x < x_0, \quad t = 0 \\ &u = u_R, \quad p = p_R, \quad \rho = \rho_R, \quad x > x_0, \quad t = 0 \end{aligned} \tag{2.6}$$

The diaphragm is located at $x = x_0$ and $p_R < p_L$. In this problem, the two gases are the same. We will assume that viscous effects along the sides of the tube wall are negligible and the length of the tube is infinite, thus avoiding reflections at the tube end.

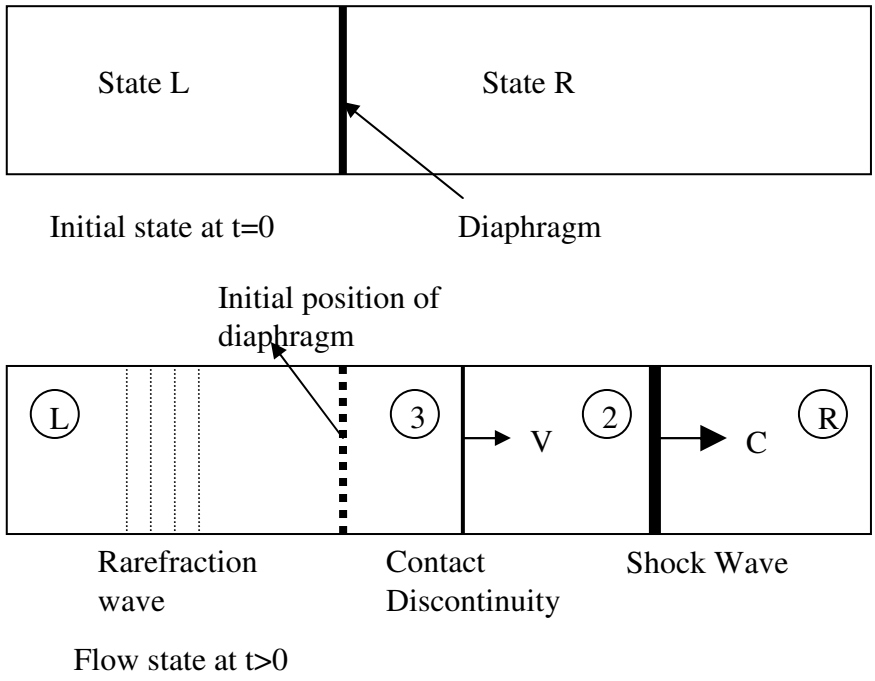

Figure 2-2: Illustration of the shock tube problem

The figure above illustrates the process. At time $t = 0$, the diaphragm is burst and the pressure discontinuity propagates to the right in the low-pressure gas and at the same time, a rarefraction wave propagates to the left in the high-pressure gas. In addition, a contact discontinuity separating the two gas regions propagates to the right in the tube.

2.3 One-Fluid and two-fluid continuum

In the simulation of two different phase media such as gas and water, there are two approaches to the problem in the literature. The first approach is the two-fluid model approach in which it is assumed that both phases co-exist at every point in the flow field and each phase is governed by its own set of differential equations. This model is further developed and explained in greater details by many authors such as Shyue (1998), Saurel and Abgrall (1999a,b) and Allaire et al (2002). The two-fluid model can easily take into account the physical details occurring at the interface such as the mass and energy exchange, thermal transfer and surface tension. But in order to simulate the exchanges at the interface, factors such as exchange rates and viscous friction between

the two phases have to be known a priori. Another disadvantage would be the total number of partial differential equations to be solved which can sometimes be twice that of a single phase flow.

In one-fluid models, the two phase media is treated as a single fluid with only one set of differential equations to solve which makes it similar to a single phase flow. However, at the interface, special techniques would have to be applied in order to prevent nonphysical oscillations at the interface due to smearing out of the density profile and the abrupt change in the equation of state across the interface. One such technique is the Original Ghost Fluid Method (to be discussed in Chapter 3) developed by Fedkiw et al. (1999) and further explored in Liu et al. (2003, 2005).

2.4 Unsteady Cavitation

The definition of cavitation is when a body of liquid under constant temperature, whose pressure is reduced by static or dynamic means, a state is reached ultimately at which cavities(gas-filled bubbles) become visible and grow (Knapp et al. (1970)). The limiting pressure is usually the vapour pressure. Cavitation is a liquid phenomenon which does not occur under any normal circumstances in either a solid or a gas. It is also a dynamic process as it is concerned with the growth and collapse of cavities. Cavitation is a phenomenon that is faced by surface sea-faring vessels as well as hydraulic equipment. When it occurs unexpectedly, damage to the structure may result due to the large forces generated when the cavitation regions collapse (Ventikos and Tzabiras (2000)). In the underwater shock analysis of naval vessels(Aanhold et al.(1998)), simulation of the unsteady cavitation process is critical in understanding more of the process and ultimately, in protecting important sea vessels or strategic oil platforms from the damage resulting. Recently, there has also been keen developments in simulating the process of unsteady cavitation in “super-cavitating” projectiles (Owis

and Nayfeh (2004)). There have also been studies conducted on the effect of cavitation collapse on rigid and deformable cylinder walls with experiments on the effects of an explosion inside a water-filled cylinder (Wardlaw et al.(2000)). In unsteady cavitation which usually occurs in the case of underwater explosion near a structure or free surface, the development of the cavitation boundary is dynamic and can evolve rapidly before finally collapsing and resulting in large sudden forces generated (Liu et al. (2004)). To simulate such cavitating flows, common models in one-fluid modelling are the Cut-off model (Aanhold et al. (1998), Wardlaw et al. (2000)), the vacuum model (Tang and Huang (1996)) and the Schmidt's model (Schmidt et al. (1999), Qin et al. (1999)). In the Cut-off model, when the liquid pressure falls below a specified critical value, the flow pressure is reinforced as a given value and computation continues. This model does not consider phase change within the cavities, making it easy to implement and use. However, the Cut-off model entails some physical violations and the system of equations may not turn out to be conservative as it degenerates non-physically due to the cut-off pressure and its associated density, resulting in zero sound speed in the cavitation regions. The vacuum model assumes zero mass inside the cavitation regions since under most circumstances, only a small amount of liquid will vaporize and the density of vapour is about $O(10^{-4})$ of the liquid density. Schmidt's model is only suitable for use in small cavitation zones under high pressure and it is found that this model does not work consistently in simulating cavitating flows with large vapour-to-liquid density ratios or under low surrounding pressure. Hence, a modified Schmidt's model was developed by Xie et al. (2005) to overcome the shortcomings of the Schmidt's model.

2.5 Interface tracking methods

There are many numerical methods in the literature which are used to track the movement of interfaces in multi-phase flows or fluid-solid interaction. Here, three main types of interface tracking methods are highlighted. They are the Volume-of-fluid(VOF) method, the marker-cell method and the level set method. A brief description of each method is mentioned below and the reader may refer to the references for further information. In the level set method, the interface is not tracked explicitly but is deduced based on a field variable such as the distance function in Chen et al.(1997), the order parameter in Kobayashi(1993) or local enthalpy in Voller and Prakash(1987). The level set method was introduced by Osher and Sethian (1988) as a simple and versatile method for computing and analyzing the motion of an interface Γ in two or three spatial dimensions. The interface Γ may bound a region Ω and the method is capable of computing the subsequent motion of the interface Γ subject to a velocity field v, normal to the interface. The interface remains sharp and retains the jumps in material and flow quantities as sharp discontinuities. The level set approach requires an initial function $\phi(x, t=0)$ with the property that the zero level set of that initial function corresponds to the initial position of the interface. The signed-distance function from each grid point to the initial interface or zero level set is computed. As a rule, only accuracy is required in a few cells near the interface. The level set function can be embedded inside the usual flow solver and advected with the normal velocity field. The new value of the function is then solved to obtain the new interface position which makes the level set function zero.

The marker/string method tracks the motion of 'markers' located at the moving interface as seen in Hirt and Nichols (1973). This method is more commonly utilized in Lagrangian framework. It first discretizes the Lagrangian form of the equations of

motion and the parameterization interval is then divided into intervals to form the 'markers'. The derivatives at these 'markers' are then approximated using the neighboring mesh points. Using Taylor Series expansion for the time and space derivatives and substituting into the equations of motion, the new position of the 'markers' can then be determined and the interface can be remapped. However, for complicated interface motions, the method suffers from instability and topological limitations because they follow a local representation of the front, rather than a global one which takes into account the proper entropy conditions and weak solutions of the equations of motion.

Another approach is the Volume-of-Fluid method from Hirt and Nichols B (1981) and Noh and Woodward (1976) which is based on an Eulerian view. This method does not suffer from the time-step and topological limitations of the marker method due to the Eulerian framework. With a fixed grid on the computational domain, values are assigned to each grid cell based on the fraction of that cell containing material inside the interface. We would need to rely on these cell fractions to characterize the interface location. In order to evolve the interface, the idea is to update the cell fractions on the fixed grid to reflect the front progress. However, there are some disadvantages depicted in Sethian (1996). A significantly large number of cells are required for the computation and in the presence of directional velocity fields, the evolution of the front becomes problematic. Also, there is an inherent inaccuracy in the calculation of the geometric properties of the front (e.g. curvature and normal direction).

In recent years, development has seen that more accurate VOF methods fit the interface through piecewise linear segments, known as the piecewise linear interface construction (PLIC), with major contributions made by Ashgriz and Poo. (1991), Rudman (1998) and He et al.(1999).

2.6 Eulerian vs Lagrangian

Traditionally, the Eulerian framework has been used for fluid dynamics computer simulation particularly in simulating high-speed fluids with strong shocks and large deformation. In the Eulerian framework, the mesh remains stationary and does not move with the fluid, rather like capturing a still shot of the fluid and its properties at that point in time. For the Lagrangian framework, the mesh moves with the local speed of the fluid/solid. Hence, Lagrangian numerical methods have difficulties treating flows with large deformations since this causes large deformations of the mesh and consequently, large numerical errors which can only be removed by complex remeshing or mesh generation techniques which tend to be low-order accurate. Due to their nature, Eulerian methods avoid such pitfalls and in addition, Eulerian shock-capturing schemes are able to capture shocks in a straight-forward way using conservation and robust limiters(Hirsch (1992)). For these methods, the shocks can be modelled with as few as one grid-cell without oscillations. In comparison, the Lagrangian numerical methods usually suffer from some post-shock oscillations until the shock is spread out over about six grid-cells as noted by Benson (1991 & 1992). While Eulerian methods work very well for fluid calculations (Fedkiw (2002)), they perform badly for solid dynamics in problems of solid loading and damage because they do not track changes in material properties at particular positions in time and space which are fundamental in modeling time-history variables. But Lagrangian methods have been proven to work well in modelling solid dynamics and that is why the Lagrangian approach has been adopted for the Naviers equation in the compressible fluid-solid simulation.

2.7 Naviers Equation vs other solid EOS

There are many Equations of State(EOS) developed for simulating the behaviour of solids. Some of these EOS in the literature include the Mie-Gruneisen EOS which has been utilized quite extensively in the simulation of solid material as attested by Miller and Puckett (1996) and Udaykumar et al. (2003) and the hydro-elasto-plastic solid model in Tang and Sotiropoulos (1999). However, till date, there has been no universal EOS for solids. A universal EOS is applicable to all types of solids, irrespective of their bonding characteristics, given the solids possess the desired homogeneity to behave as an elastic continuum. Moreover, many of these EOS require parameters, which are not readily available and either have to be obtained experimentally or derived through other more common parameters, in addition to the standard properties provided in most material handbooks and these additional parameters may also differ under different conditions. This difficulty in obtaining appropriate parameters has sometimes hindered the use of many EOS in the simulation of solid behaviour and thus, affected the acceptance of these by the community. Also, though a few of the EOSs have a partial theoretical support, none of them is derived from fundamental structural energetics and as such, these EOS are essentially empirical in nature according to Bose and Bose (2004).

On the other hand, the Naviers Equations, which are differential conditions of equilibrium, had been developed based on the well-known theory of elasticity for small deformations of the solid. It has been used extensively in the solution for the stresses and strains in many elastic problems, especially in the field of modeling seismic waves in the earth's crust as seen in Minkoff (2002). In addition, the only material parameters required in the Naviers Equations are the Young modulus and the Poisson ratio data, both of which are readily available in most material handbooks. As such, the Naviers

Equations can be utilized to simulate the behaviour of many different solid materials. The limitations would be problems involving large deformations of the solid, and also problems involving plastic flow whereby due to the non-linear constitutive stress-strain relations, the system of governing equations becomes non-linear as well. In addition, the Naviers equation when applied to homogeneous, isotropic medium, consists of a system of PDEs which are hyperbolic in nature. The Euler equation for the fluid medium is hyperbolic in time. As such, high-order, upwind schemes such as MUSCL scheme developed for the Euler equation can also be applicable to the Naviers equation and thus, there is no need to develop new schemes for the Naviers Equation.

Chapter 3 Methodology:1D System

3.1 1D Planar Euler equations

The 1D conservative Euler equations for inviscid with no heat conduction gas-gas and gas-water compressible flows can be written in a quasi-linear form as

$$\frac{\partial U}{\partial t}+\frac{\partial F(U)}{\partial x}=0 \qquad t\in[(0,\infty)\ and\ x\in[x_A,x_B], \tag{3.1a}$$

Where

$$U=\begin{pmatrix}\rho\\ \rho u\\ E\end{pmatrix}, \qquad F(U)=\begin{pmatrix}\rho u\\ \rho u^2+P\\ u(E+P)\end{pmatrix}, \tag{3.1b}$$

The independent variables are time (*t)* and spatial distance (*x)* while the dependent variables are pressure (*P)*, density (ρ*)*, flow velocity (*u)* and total energy per unit volume, (*E)*. $[x_A, x_B]$ is the spatial interval in the computational domain. The source or forcing term in this case is equal to zero and thus, the equations above are homogeneous equations. However, since there are 4 dependent variables and only 3 equations, it is then not mathematically possible to solve for the respective variables. Hence, an EOS or Equation of State is required to close this system of equations in Eqn.(3.1). For compressible gas flows, the equation of state used is the perfect gas law and is given as

$$E=\frac{P}{\gamma-1}+\frac{1}{2}\rho u^2, \tag{3.2}$$

where γ is the specific heat ratio and is set equal to 1.4 for air.

In the case of water, the Tait's equation is utilized as the equation of state(Flores and Holt, 1981). The Tait's equation is simply

$$\frac{\overline{P}}{\overline{P_0}} = \left(\frac{\rho}{\rho_0} \right)^N , \tag{3.3}$$

where $\overline{P} = P + B$, $\overline{P_0} = P_0 + B$; B is constant and is equal to $3.309x10^8\, Pa$ and the initial water pressure, $P_0 = 10^5\, Pa$ and initial water density, $\rho_0 = 1000\, {}^{kg}/_{m^3}$. It should be noted that this equation is only applicable under pressures lower than 20000 atm. The power index, N is set to 7.15. Using Tate's equation, the speed of sound in water is

$$\bar{a} = \sqrt{\frac{d\overline{P}}{d\rho}} = \sqrt{\frac{N\overline{P}}{\rho}}, \tag{3.4}$$

and the total energy of water is given as

$$E = \frac{P + NB}{N - 1} + \frac{1}{2}\rho u^2 , \tag{3.5}$$

There are other equations of state for water such as the Tillotson equation. In Tate's equation, the water pressure is merely a function of the water density. The latter is similar in form to the perfect gas law which is the equation of state for gas medium. In addition, it is noted that if γ is replaced with N and a (where $a = \sqrt{\frac{\gamma P}{\rho}}$ in gas) is seen as the local sound speed in a similar form to the sound speed in water, $\bar{a}$, the equations for gas and water then become similar in form. Hence, the same computational scheme can be applied to both gas and water. This would also make the computer code more generic.

3.2 1D Naviers Equation

For a linearly elastic, isotropic, homogeneous solid material, the Naviers equation from Chung (1996) is given as

$$(\lambda+2\mu)\nabla(\nabla\cdot\vec{\varepsilon})-\mu\nabla\times(\nabla\times\vec{\varepsilon})-\rho\frac{\partial^2\vec{\varepsilon}}{\partial t^2}+\rho f=0\,, \tag{3.6}$$

where λ and μ are Lame constants, *f* represents the body forces and is assumed to be zero and ε represents the displacement of each mesh point in the solid. Supposing $\vec{v}$ is a vector and defined by $\vec{v}=v_x i+v_y j+v_z k$,

$$curl(\vec{v})=\nabla\times\vec{v}=i\left(\frac{\partial v_z}{\partial y}-\frac{\partial v_y}{\partial z}\right)+j\left(\frac{\partial v_x}{\partial z}-\frac{\partial v_z}{\partial x}\right)+k\left(\frac{\partial v_y}{\partial x}-\frac{\partial v_x}{\partial y}\right), \tag{3.6a}$$

$$div(\vec{v})=\nabla\cdot\vec{v}=\frac{\partial v_x}{\partial x}+\frac{\partial v_y}{\partial y}+\frac{\partial v_z}{\partial z}, \tag{3.6b}$$

$grad(s)=\nabla s=i\frac{\partial s}{\partial x}+j\frac{\partial s}{\partial y}+k\frac{\partial s}{\partial z}$ where *s* is a scalar field. (3.6c)

The Naviers Equations are also known as differential conditions of equilibrium. These equations have been developed for the unstrained state of the solid and may only be considered relevant for very small deformations. In addition, since the Lagrangian mesh is used for the solid, large deformations are not allowed as it will result in problems related to meshing. In Eqn. (3.6),

$$\mu=\frac{E}{2(1+\upsilon)} \tag{3.7a}$$

and $\lambda=\frac{\upsilon E}{(1+\upsilon)(1-2\upsilon)}$, (3.7b)

with *E* and υ being the material's Young modulus of elasticity and the Poisson ratio, respectively. They are material constants and depend very much on the type of material used. If the material is symmetric with respect to every plane and every axis, then the elastic properties are identical in all directions. Material which exhibits such a property is said to be isotropic. In a homogeneous material, it is assumed that there are no second phases, voids and nucleations and thus, the density throughout the material is assumed constant.

For 1D, $\mu\nabla\times(\nabla\times\vec{\varepsilon})=0$ in Eqn. (3.6) and the equation becomes

$$(\lambda+2\mu)\nabla(\nabla\cdot\vec{\varepsilon})=\rho\frac{\partial^2\vec{\varepsilon}}{\partial t^2}. \tag{3.8a}$$

Eqn. (3.8a) can be written in the form of

$$\frac{\partial^2\varepsilon}{\partial x^2}=\frac{1}{c_s{}^2}\frac{\partial^2\varepsilon}{\partial t^2}, \tag{3.8b}$$

where $c_s=\sqrt{\frac{\lambda+2\mu}{\rho_s}}$ is defined as the propagation speed of the elastic longitudinal wave in the solid. In order to relate displacements to stresses in the solid, another equation is required. In the case of elastic solids, the most common relationship is the 1D Hooke's law where

$$\sigma=E\frac{\partial\varepsilon}{\partial x}, \tag{3.9a}$$

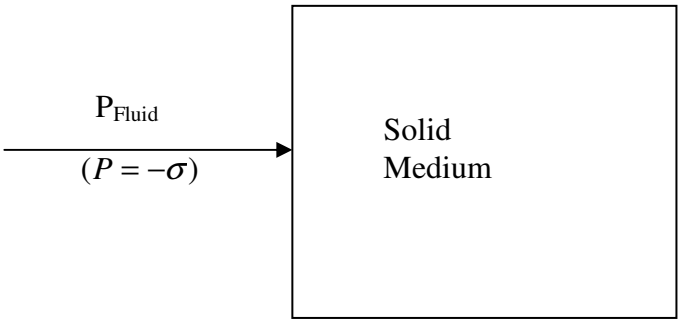

Figure 3-1 : Illustration of fluid pressure(compressive stress) on solid medium

However, in solids, tensile stress is defined as positive which is in opposite direction to the pressure definition in fluids($\sigma=-P$) as seen in Fig. 3-1. Hence, to resolve the contradiction in modelling, the Hooke's law is rewritten as

$$\sigma=-E\frac{\partial\varepsilon}{\partial x} \tag{3.9b}$$

and hence,

$$\therefore\frac{\partial^2\varepsilon}{\partial t^2}=-\left(\frac{2\mu+\lambda}{E\rho_s}\right)\frac{\partial\sigma}{\partial x}, \tag{3.10}$$

Eqn. (3.10) thus shows the Naviers equation in the form relating displacement to stress.

The velocity of each node in the solid is related to the displacement by the following relationship, $u = \frac{\partial \varepsilon}{\partial t}$. This relationship is used to convert Eqn. (3.9b) and Eqn. (3.10) into the equations below relating velocity to pressure.

$\frac{\partial u}{\partial t} + \frac{{c_s}^2}{E}\frac{\partial P}{\partial x} = 0$ relates the velocity to pressure within the solid, (3.11a)

$\frac{\partial P}{\partial t} + E\frac{\partial u}{\partial x} = 0$ is obtained by differentiating Eqn. (3.9b) with respect to time. (3.11b)

Writing the equations in Eqn. (3.11) in a quasi-linear form similar to the Euler equations, we have

$$\frac{\partial U}{\partial t} + \frac{\partial F}{\partial x} = 0 \Rightarrow \frac{\partial U}{\partial t} + A\frac{\partial U}{\partial x} = 0, \tag{3.12}$$

where the variable U and Flux F are defined as $U = \begin{pmatrix} u \\ P \end{pmatrix}$, $F = \begin{pmatrix} \frac{{c_s}^2}{E}P \\ Eu \end{pmatrix}$ and the Jacobian matrix is $A = \begin{pmatrix} 0 & \frac{{c_s}^2}{E} \\ E & 0 \end{pmatrix}$ with the corresponding eigenvalues of $\lambda_1 = c_s \quad or \quad \lambda_2 = -c_s$.

Using linear algebra techniques, the right eigenvector and its determinant is calculated as

$$\overline{R} = \frac{R}{E} = \begin{pmatrix} \frac{1}{E} & \frac{1}{E} \\ \frac{1}{c_s} & -\frac{1}{c_s} \end{pmatrix}, \tag{3.13}$$

$$\det \overline{R} = \begin{vmatrix} \frac{1}{E} & \frac{1}{E} \\ \frac{1}{c_s} & -\frac{1}{c_s} \end{vmatrix} = -\frac{2}{c_s E}, \tag{3.14}$$

whereas the left eigenvector, which is the inverse of the right eigenvector, is

$$L = \begin{pmatrix} \frac{E}{2} & \frac{c_s}{2} \\ \frac{E}{2} & -\frac{c_s}{2} \end{pmatrix}. \tag{3.15}$$

These variables are essential in the implementation of the high-order MUSCL scheme as a numerical solver for the solid.

3.3 Level-set method for Interface

In the Eulerian frame, the grid is fixed and does not move with the fluid. The interface position can be captured using the level-set technique originally developed by Sethian and Osher (1988). In the level-set method, the interface is not captured as a function but rather embedded as a particular level set in a partial differential solution of a fixed domain.

For the 1D planar flow, the level set function is defined as

$$\frac{\partial \phi}{\partial t} + u\frac{\partial \phi}{\partial x} = 0. \tag{3.16}$$

ϕ is initialized as the normal distance measured from the interface, i.e. $\phi(x,0) = x - x_I^0$.

Discretizing Eqn. (3.16) using the second-order upwind difference scheme, we have from Liu et al (2001),

$$\begin{aligned} \phi_j^{n+1} &= \phi_j^n - \lambda\frac{u_j^n + |u_j^n|}{2}\left(\phi_j^n - \phi_{j-1}^n + 0.5g_j^n\right) \\ &- \lambda\frac{u_j^n - |u_j^n|}{2}\left(\phi_{j+1}^n - \phi_j^n - 0.5g_{j+1}^n\right) + 0.5\left(\lambda u_j^n\right)^2 g_j^n \end{aligned}, \tag{3.17a}$$

$$g_j^n = \min\mathrm{mod}\left(\phi_{j+1}^n - 2\phi_j^n + \phi_{j-1}^n, \phi_j^n - 2\phi_{j-1}^n + \phi_{j-2}^n\right), \tag{3.17b}$$

$$\min\mathrm{mod}(a,b) = 0.5\left(sign(a) + sign(b)\right)\min\left(|a|,|b|\right), \tag{3.17c}$$

where $\lambda = \frac{\Delta t}{\Delta x}$ and Δt and Δx are the time and spatial step sizes, respectively.

To obtain the new position of the interface, we simply calculate the x that makes $\phi^{n+1} = 0$. For the 1D multi-medium flow, the scheme for re-initialization is carried out by redefining at time, t^n, $\phi(x) = x - x_I^n$.

3.4 Ghost Fluid Method

For simple illustration, the one-dimensional ghost fluid method is explained. Here, the Ghost Fluid Method is termed as the Original Ghost Fluid Method to distinguish it from other variants which follow. Three quantities are defined in the ghost region in order to define the ghost nodes. Since many problems involve continuous pressure and velocity across the interface, pressure and velocity are two of the three quantities needed and the pressure and velocity of the ghost fluid can be set equal to the pressure and velocity of the real fluid. So we copy node by node, the real fluid values of pressure and velocity onto the ghost fluid values of pressure and velocity. Using this method, the interface boundary conditions for the pressure and velocity can be captured without specifying the location of the interface. The last quantity selected is entropy because since entropy is generally discontinuous across a contact discontinuity, when standard finite difference schemes are applied, large dissipative errors can arise which can lead to spurious oscillations at the interface. These oscillations can be eliminated by using one-sided extrapolation of the entropy, resulting in a continuous entropy profile.

According to Fig. 3-2 below, the zero level of the level set function lies between nodes *i* and *i*+1. The fluid 1 is defined at node *i* and to the left of node *i* while fluid 2 is defined at node *i*+1 and to the right of node *i*+1. In order to update fluid 1, we define ghost fluid values of fluid 1 at nodes to the right and including node *i*+1. For each of

these nodes, we obtain the ghost fluid value by combining fluid 2's pressure and velocity with fluid 1's entropy from node *i* in the process of constant extrapolation.

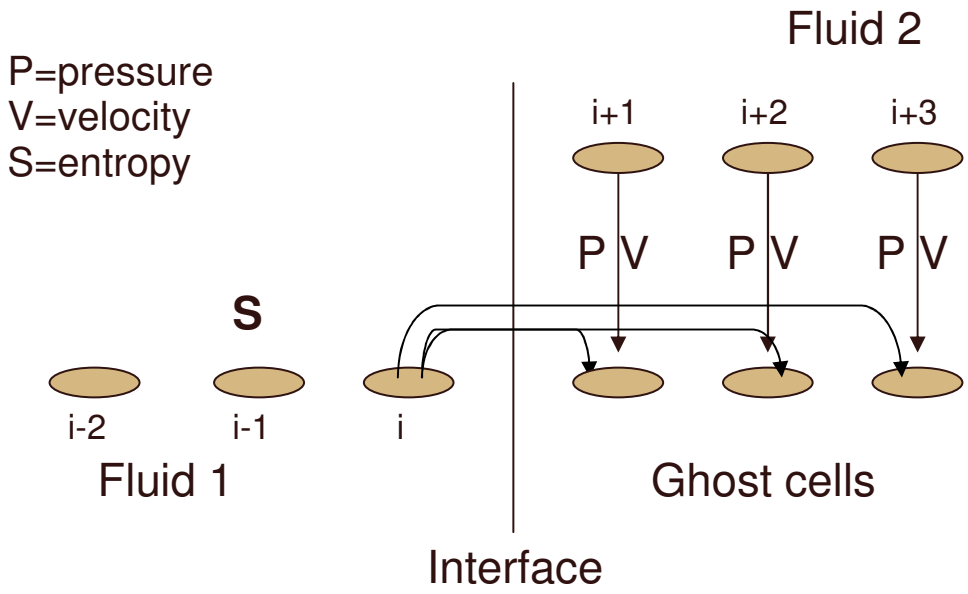

Figure 3-2 : Illustration of Original Ghost Fluid method without isobaric fixing

For the isobaric fix which is used to reduce "overheating" errors, it is illustrated in Fig. 3-3 below and the entropy at node *i* is changed to be equal to the entropy at node *i*-1 without modifying the pressure and velocity values at node *i*. The entropy at node *i*+1 is modified to be equal to node *i*+2. In the Original Ghost Fluid Method, only a band of 3 to 5 ghost cells are needed on each side of the interface depending on the interface movement and stencil used.

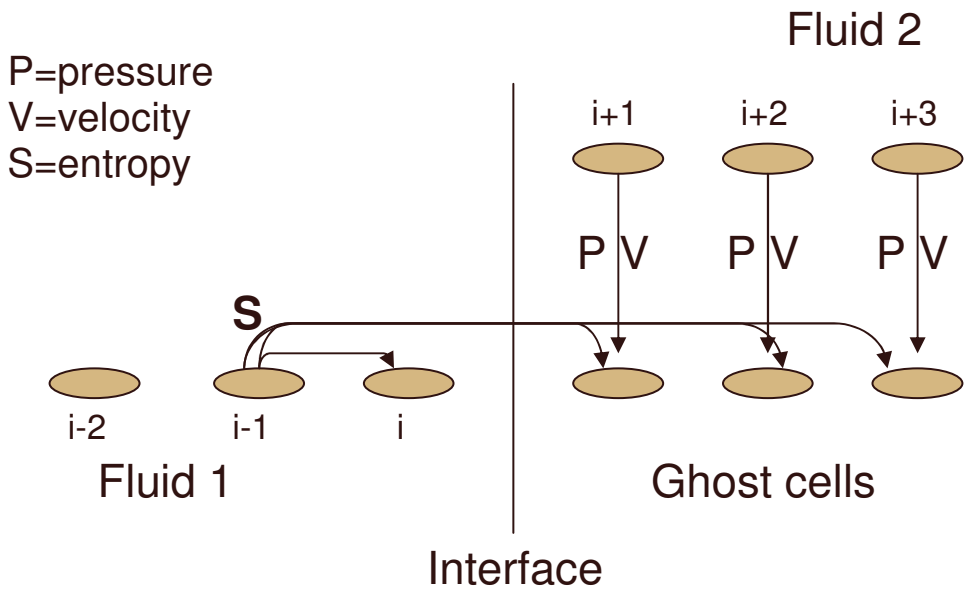

Figure 3-3: Illustration of Original Ghost Fluid Method with isobaric fixing

The Original Ghost Fluid Method in Fedkiw et al. (1999) is simple to implement and does not need to solve an initial boundary value problem, nor the Rankine-Hugoniot jump conditions or a Riemann problem at the interface.

3.5 Riemann solver at the interface

However, it has been shown by Liu et al. (2003) that the Original Ghost Fluid Method does not work very efficiently in the application of a strong shockwave impacting on an interface even though it works well for shock tube problems and moderate shock impacting on an interface problems. In applications with a strong shock impacting, the interface pressure, velocity and entropy may have a sudden jump and the sudden jump in these properties implies that the real fluid pressure and velocity may not be acceptable ghost fluid pressure and velocity. Hence, the ghost fluid pressure and velocity would have to be determined first before the ghost fluid method is applied. By employing the Rankine-Hugoniot conditions, it ensures that the flow dynamic behaviour is correct at the interface (i.e. the continuity of pressure and normal velocity) but by itself, it is still inadequate to fully determine the interfacial status. This is

because at the moment of a strong shock impacting a surface, it creates a singularity where the pressure and velocity values are discontinuous and this singularity has to be correctly decomposed in order to supplement the Rankine-Hugoniot conditions in fully describing the interface state.

3.5.1 Fluid Characteristic Equations

To correctly predict the interface pressure and velocity, the Modified Ghost Fluid Method is developed in Liu et al (2003) whereby Rankine-Hugoniot conditions and implicit characteristic equations are used to solve the Riemann problem at the interface. Fig. 3-4 below illustrates the basic concept of the Modified Ghost Fluid Method.

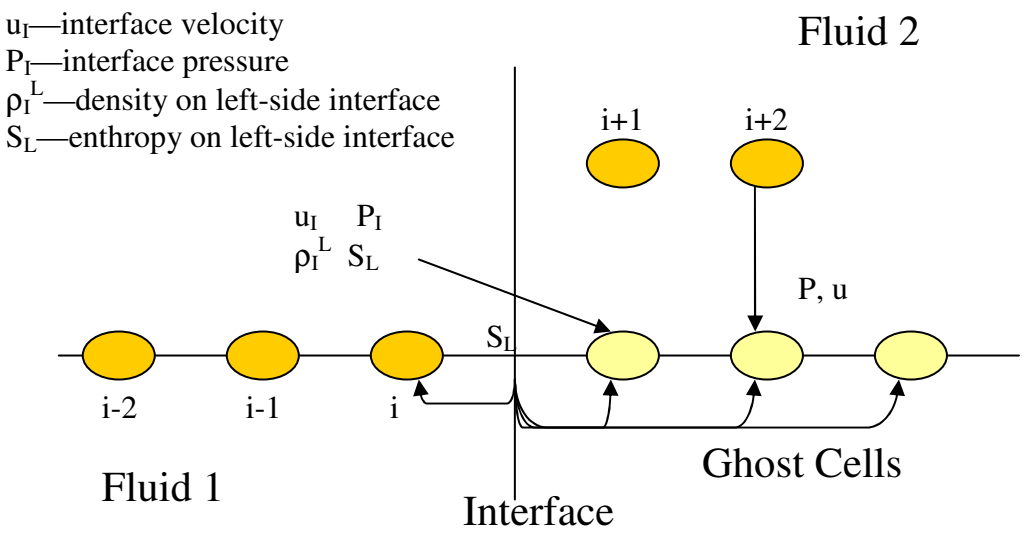

Figure 3-4:Illustration of Modified Ghost Fluid Method

Unlike the Original Ghost Fluid Method, the Modified Ghost Fluid Method is able to calculate predicted interface values and ghost fluid status based on an approximate Riemann solver.

Here, we will directly apply the characteristic equation from the Modified Ghost Fluid Method in order to solve for the interface values. For the fluid, the two nonlinear characteristics are

$$\frac{dP_I}{dt} + \rho_{IL} c_{IL} \frac{du_I}{dt} = 0, \text{ along } \frac{dx}{dt} = u_I + c_{IL}, \tag{3.18a}$$

$$\frac{dP_I}{dt} - \rho_{IR} c_{IR} \frac{du_I}{dt} = 0, \text{ along } \frac{dx}{dt} = u_I - c_{IR}, \tag{3.18b}$$

where $\rho_{IL}(\rho_{IR})$ and $c_{IL}(c_{IR})$ are the density and sound speed to the left(right) of the interface. Depending on the orientation of the fluid with respect to the solid, the corresponding characteristic can be chosen from Eqn. (3.18). To illustrate the Approximate Riemann solver at the interface, the fluid has been chosen to reside on the left and the solid on the right. Hence Eqn. (3.18a) would form the C^+ characteristic line.

3.5.2 Solid Characteristic Equations

As for the solid media, Eqn. (3.10) is formulated using the Hamilton-Jacobi method as

$$\frac{\partial U}{\partial t} + A \frac{\partial U}{\partial x} = 0, \tag{3.19a}$$

and since $A = R \Lambda R^{-1}$,

$$R^{-1} \frac{\partial U}{\partial t} + \Lambda R^{-1} \frac{\partial U}{\partial x} = 0, \tag{3.19b}$$

where R^{-1} is obtained from Eqn. (3.15), $A = \begin{pmatrix} 0 & \frac{c_s^2}{E} \\ E & 0 \end{pmatrix}$, $U = \begin{pmatrix} u \\ P \end{pmatrix}$ and Λ refers to the respective eigenvalues.

For the solid on the right-hand side(i.e. C^- characteristics along $\frac{Dx}{Dt} = -c_s$), Eqn. (3.19b) leads to

$$\frac{D}{Dt}\left(\frac{1}{2}u-\frac{c_s}{2E}P\right)-c_s\frac{D}{Dx}\left(\frac{1}{2}u-\frac{c_s}{2E}P\right)=0,\ for\ \frac{Dx}{Dt}=-c_s, \tag{3.20}$$

$$\Rightarrow\frac{D}{Dt}\left(\frac{1}{2}u-\frac{c_s}{2E}P\right)+\frac{Dx}{Dt}\cdot\frac{D}{Dx}\left(\frac{1}{2}u-\frac{c_s}{2E}P\right)=0. \tag{3.21}$$

Hence the C^- characteristic line is given by

$$\frac{D}{Dt}\left(u-\frac{c_s}{E}P\right)=0\ \text{ along }\ \frac{Dx}{Dt}=-c_s, \tag{3.22}$$

where c_s is the Naviers equation elastic wave propagation speed.

From Eqn. (3.22),

$$u_I-\frac{c_s}{E}P_I=u_s-\frac{c_s}{E}P_s, \tag{3.23}$$

$$\Rightarrow u_I-u_s=\frac{c_s}{E}\left(P_I-P_s\right). \tag{3.24}$$

From the fluid characteristic equation, Eqn. (3.18a) is re-arranged to give

$$\frac{\partial P}{\partial t}+\rho_w C_w\frac{\partial u}{\partial t}=0. \tag{3.25}$$

When discretized, Eqn. (3.25) leads to

$$P_I=P_w-\rho_w C_w\left(u_I-u_w\right). \tag{3.26}$$

Solving Eqn. (3.24) and Eqn. (3.26) simultaneously, the interface velocity can be found from the resulting equation below as

$$u_I=\frac{\frac{c_s}{E}\left(P_w-P_s\right)+\frac{c_s}{E}\rho_w C_w u_w+u_s}{\frac{c_s}{E}\rho_w C_w+1}, \tag{3.27}$$

Here the subscript *w* and *s* refers to the fluid and solid values, respectively and the interface pressure can be found by substituting the value of u_I back into Eqn. (3.26).

3.6 Numerical solver

3.6.1 Numerical solver for fluid media

In this thesis, simulations of compressible fluid-solid interaction are carried out and often, these simulations deal with shock which requires high order schemes in order to capture the shock front over a few computational cells. Such high-resolution upwind schemes include TVD scheme (Harten, 1983) and ENO scheme (Harten et al, 1986, 1987).

The reader is referred to more details of the TVD scheme in Leer(1979) and Harten(1989); these are briefly given below as

$$U_j^{n+1} = U_j^n - \frac{\Delta t}{\Delta x}\left(H_{j+\frac{1}{2}}^n - H_{j-\frac{1}{2}}^n\right), \tag{3.28}$$

$$H_{j+\frac{1}{2}}^n = \frac{1}{2}\left[F\left(U_{L_{j+\frac{1}{2}}}^n\right) + F\left(U_{R_{j+\frac{1}{2}}}^n\right) - \left|A_{LR_{j+\frac{1}{2}}}\right|\left(U_{R_{j+\frac{1}{2}}}^n - U_{L_{j+\frac{1}{2}}}^n\right)\right], \tag{3.29}$$

$$U_{L_{j+\frac{1}{2}}}^n = U_j^n + \frac{1}{2}R_{j+\frac{1}{2}}\Phi_{j+\frac{1}{2}}^L, \tag{3.30}$$

$$U_{R_{j+\frac{1}{2}}}^n = U_{j+1}^n - \frac{1}{2}R_{j+\frac{1}{2}}\Phi_{j+\frac{1}{2}}^R, \tag{3.31}$$

$$\Phi_{j+\frac{1}{2}}^L = \left[\phi_{j+\frac{1}{2}}^{L,1}, \quad \phi_{j+\frac{1}{2}}^{L,2}, \quad \phi_{j+\frac{1}{2}}^{L,3}\right]^T, \tag{3.32}$$

$$\Phi_{j+\frac{1}{2}}^R = \left[\phi_{j+\frac{1}{2}}^{R,1}, \quad \phi_{j+\frac{1}{2}}^{R,2}, \quad \phi_{j+\frac{1}{2}}^{R,3}\right]^T, \tag{3.33}$$

$$\phi_{j+\frac{1}{2}}^{L,l} = \left(1 - \lambda_{j+\frac{1}{2}}^l\right)g_{j+\frac{1}{2}}^l, \tag{3.34}$$

$$\phi_{j+\frac{1}{2}}^{R,l} = \left(1 + \lambda_{j+\frac{1}{2}}^l\right)g_{j+\frac{1}{2}}^l, \tag{3.35}$$

$$g_{j+\frac{1}{2}}^l = \min\mathrm{mod}\left(\alpha_{j+\frac{1}{2}}^l, \alpha_{j+\frac{3}{2}}^l\right), \tag{3.36}$$

$$\left(\alpha_{j+\frac{1}{2}}^1, \quad \alpha_{j+\frac{1}{2}}^2, \quad \alpha_{j+\frac{1}{2}}^3\right)^T = R_{j+\frac{1}{2}}^{-1}\left(U_{j+1}^n - U_j^n\right), \tag{3.37}$$

$$l = 1, 2, 3; \quad j = 2 \ldots I.$$

where *I* is the interface between the fluid and solid media and $A_{LR_{j+\frac{1}{2}}}$ satisfies Roe's average condition,

$$F\left(U^{n}_{R\,j+\frac{1}{2}}\right)-F\left(U^{n}_{L\,j+\frac{1}{2}}\right)=A_{LR_{j+\frac{1}{2}}}\left(U^{n}_{R\,j+\frac{1}{2}}-U^{n}_{L\,j+\frac{1}{2}}\right). \tag{3.38}$$

Here $A=\dfrac{\partial F(U)}{\partial U}$ and $R_{j+\frac{1}{2}}$, $R^{-1}_{j+\frac{1}{2}}$ and $\lambda^{l}_{j+\frac{1}{2}}$ are the right eigenvector, left eigenvector and eigenvalues of matrix *A,* respectively. For the fluid media, $\lambda^{1}_{j+\frac{1}{2}}=u$, $\lambda^{2}_{j+\frac{1}{2}}=u+c$ and $\lambda^{3}_{j+\frac{1}{2}}=u-c$ .To ensure stability for the TVD scheme, a stability condition is normally enforced. The CFL condition for the fluid media is set as

$$\Delta t_{f}=CFL\frac{\Delta x}{\max\left(\left|u_{j}\right|+c_{j}\right)}. \tag{3.39}$$

where u_j and c_j are the velocity and sound speed of each mesh point, respectively.

3.6.2 Numerical solver for solid media

For the solid media, the scheme is similar to the earlier MUSCL scheme for the fluid media. The difference lies in the limiter applied. Different limiters would apply different extents of dissipation at the location of large gradients. The limiter used for the fluid media is the minmod limiter which works well for fluid but diffuses the shock in the solid media. A more compressive limiter should be applied to sharpen the shock in the solid media.

For the solid media, the second-order modified Harten's TVD MUSCL scheme with the incorporation of an artificial compression method(ACM) technique in the immediate region of shock/contact discontinuity from Liu et al. (1999) was applied. This modified scheme is able to accurately capture shock fronts and especially contact discontinuities well by increasing the resolution only in the region near the shock/contact discontinuity and it is able to do so without changing the properties and

attributes of the original scheme. The rest of the solution follows the TVD-MUSCL scheme because the use of ACM technique in smooth regions will distort the solution and hence the application of this ACM technique is limited to the immediate region surrounding the shock/contact discontinuity. Using the modified MUSCL scheme with ACM technique as the solid solver, we are able to capture the shock front over comparably fewer computational cells compared to just using the MUSCL scheme without ACM technique. Hence, the modified MUSCL scheme with ACM technique is applied as the solid solver in the steps below.

$$U_j^{n+1} = U_j^n - \frac{\Delta t}{\Delta x}\left(H_{j+\frac{1}{2}}^n - H_{j-\frac{1}{2}}^n\right) \tag{3.40}$$

$$H_{j+\frac{1}{2}}^n = \frac{1}{2}\left[F\left(U_{L_{j+\frac{1}{2}}}^n\right) + F\left(U_{R_{j+\frac{1}{2}}}^n\right) - \left|A_{LR_{j+\frac{1}{2}}}\right|\left(U_{R_{j+\frac{1}{2}}}^n - U_{L_{j+\frac{1}{2}}}^n\right)\right] \tag{3.41}$$

$$U_{L_{j+\frac{1}{2}}}^n = U_j^n + \frac{1}{2}R_{j+\frac{1}{2}}\Phi_{j+\frac{1}{2}}^L \tag{3.42a}$$

$$U_{R_{j+\frac{1}{2}}}^n = U_{j+1}^n - \frac{1}{2}R_{j+\frac{1}{2}}\Phi_{j+\frac{1}{2}}^R \tag{3.42b}$$

$$\Phi_{j+\frac{1}{2}}^L = \begin{pmatrix}\phi_{j+\frac{1}{2}}^{L,1}\\ \phi_{j+\frac{1}{2}}^{L,2}\end{pmatrix}, \quad \Phi_{j+\frac{1}{2}}^R = \begin{pmatrix}\phi_{j+\frac{1}{2}}^{R,1}\\ \phi_{j+\frac{1}{2}}^{R,2}\end{pmatrix} \tag{3.43}$$

$$\begin{cases}\phi_{j+\frac{1}{2}}^{L,l} = \left(1-\lambda_{j+\frac{1}{2}}^l\right)g_{j+\frac{1}{2}}^{H,l}\\ \phi_{j+\frac{1}{2}}^{R,l} = \left(1+\lambda_{j+\frac{1}{2}}^l\right)g_{j+\frac{1}{2}}^{H,l}\end{cases} \Rightarrow g_j^{H,l} = \left(1+q_{j+\frac{1}{2}}^l\right)g_{j+\frac{1}{2}}^l, \tag{3.44}$$

$$q_{j+\frac{1}{2}}^l = S_{j+\frac{1}{2}} \times \frac{\left|\alpha_{j+\frac{1}{2}}^1 - \alpha_{j-\frac{1}{2}}^1\right|}{\left|\alpha_{j+\frac{1}{2}}^1\right| + \left|\alpha_{j-\frac{1}{2}}^1\right|} \times \frac{\varphi\left(\xi_r\lambda_{j+\frac{1}{2}}^l\right)}{\sigma\left(\xi_r\lambda_{j+\frac{1}{2}}^l\right)}, \tag{3.45}$$

$$S_{j+\frac{1}{2}} = \frac{1}{2}\left|sign\left(\lambda_{j+\frac{1}{2}}^1 - \lambda_{j-\frac{1}{2}}^1\right) - sign\left(\lambda_{j+\frac{1}{2}}^2 - \lambda_{j-\frac{1}{2}}^2\right)\right|, \tag{3.46}$$

$$\varphi(x) = \begin{cases}|x| & if\ |x| \geq 2\varepsilon,\\ \dfrac{x^2+4\varepsilon^2}{4\varepsilon} & otherwise,\end{cases} \tag{3.47}$$

$$\sigma(x)=\frac{1}{2}\varphi(x)-\frac{1}{2}x^2. \tag{3.48}$$

$$\begin{pmatrix}\alpha^1_{j+\frac{1}{2}}\\ \alpha^2_{j+\frac{1}{2}}\end{pmatrix}=R^{-1}_{j+\frac{1}{2}}\left(U^n_{j+1}-U^n_j\right) \tag{3.49}$$

$$l=1,2;\quad j=I+1\ldots M-1.$$

where ε is a very small number, typically of the order of 10^{-3}.

Similarly, the CFL condition is enforced for the solid media, using the Lagrangian approach.

$$\Delta t_s=CFL\frac{\Delta x}{\max\left(c_j\right)}. \tag{3.50}$$

where c_j is the sound speed of each mesh point.

However, since there can only be one Δt, the time step is chosen such that it is the smaller of the 2 values in order to ensure stability. That is,

$$\Delta t=\min\left\{\left(CFL\frac{\Delta x}{\max\left(\left|u_j\right|+c_j\right)}\right)_f,\left(CFL\frac{\Delta x}{\max\left(c_j\right)}\right)_s\right\}. \tag{3.51}$$

$$f-fluid,\quad s-solid$$

Since the wave speed propagation in solids is usually much higher than the sound speed in fluids, the timestep size employed follows that of the solid timestep which is relatively small. The timestep limitation thus becomes one of the factors for consideration in multi-dimensional simulations.

Also, since the Lagrangian approach is applied to the solid mesh, the mesh nodes would move with the local velocity and new positions of the nodes are updated at every single timestep according to:

$$X_{new}=X_{old}+\left(u_{new}-u_{old}\right)\Delta t. \tag{3.52}$$

This is only applicable to the mesh on the solid side.

3.6.3 Computational Procedures

The computational steps in the program are briefly summarized below. Firstly, it was assumed that the various variables at time $t = t^n$ are known and then the steps below are used to obtain quantities at the next time step.

1. The level set function, ϕ, is advanced to the next time step and the identification matrix, S_k^{n+1} for each medium is updated for the whole domain.
2. The computational domain for each medium is then defined based on the identification matrix.
3. The previous flow field is then mapped onto the working domain and the Modified Ghost Fluid Method is applied to the three points nearest the interface.
4. Using the Method of Characteristics, the quantities P_I^{n+1}, u_I^{n+1} are obtained from eqn.(3.26) and eqn.(3.27) respectively.
5. The quantity U_k^{n+1} is obtained using the numerical solver for each medium and update U^{n+1} using the relation $U^{n+1} = U^{n+1} + S_k^{n+1} U_k^{n+1}$ (U^{n+1} is initialized to zero at the beginning).
6. The whole cycle is repeated using the new calculated time step size.

3.7 Analytical Solution

Since coupling the Naviers equation with the Eulers equation in a finite difference scheme is relatively new, the numerical solution can be verified by comparison with the analytical solution for each case. However, this method can only work for one-dimensional problems as the analytical solutions for multi-dimensions are difficult to obtain. Here this section covers the derivation of the analytical solutions for specific scenarios. In all the analytical problems, it is assumed that the shock tube is open at both ends and that no reflection takes place at the boundaries.

3.7.1 Fluid-Solid(shock-shock)

In compressible fluid dynamics, when a moving shock impacts on a fluid-solid interface, part of the shock is reflected back into the fluid and part of the shock is transmitted into the solid media.

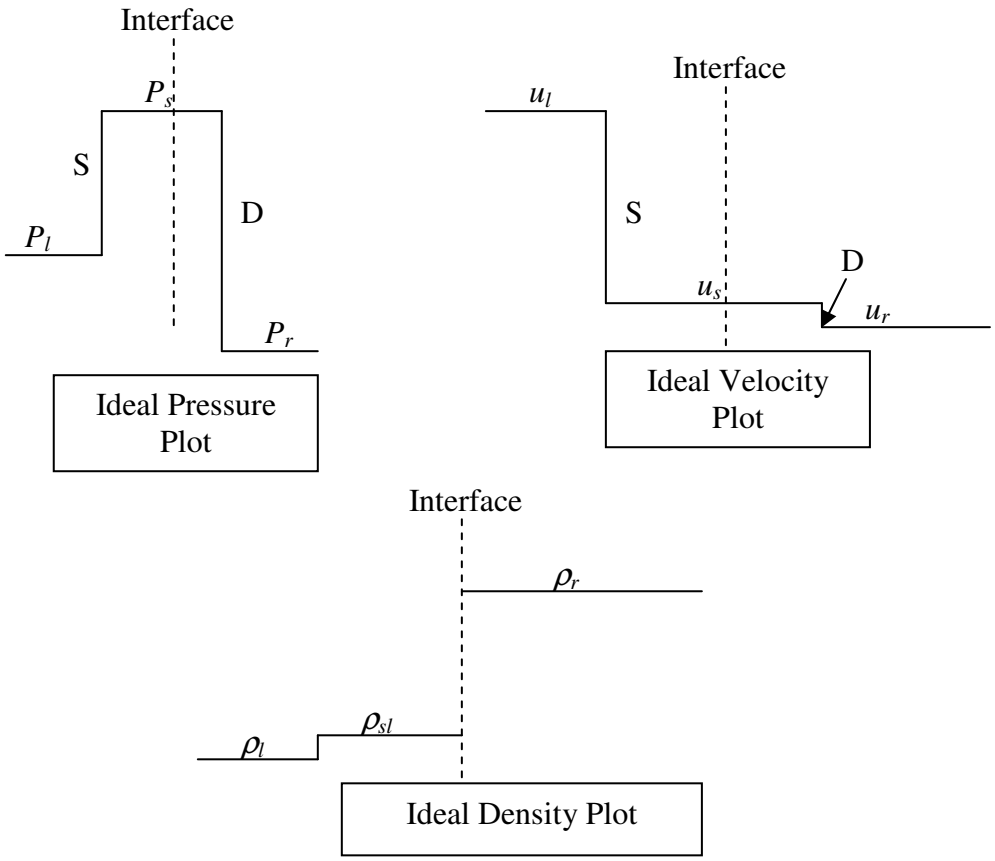

Figure 3-5: Ideal pressure, velocity and density plots in a shock-shock interaction

The nomenclature of the various quantities is in accordance with the ideal plots above. For the case of a shockwave in both the gas and the solid where the shock speed in gas is denoted by S and the shock speed in solid is denoted by D, the Rankine-Hugoniot conditions for the gas are as follows,

$$\rho_l(u_l - S) = \rho_{sl}(u_s - S), \tag{3.53a}$$

$$P_l + \rho_l(u_l - S)^2 = P_s + \rho_{sl}(u_s - S)^2, \tag{3.53b}$$

$$\frac{h_l}{\rho_l} + \frac{1}{2}(u_l - S)^2 = \frac{h_s}{\rho_{sl}} + \frac{1}{2}(u_s - S)^2, \tag{3.53c}$$

where $h = \dfrac{e+P}{\rho}$ is the entropy of each medium.

The perfect gas law is applied as the EOS for the gas medium and it is expressed in the fluid as

$$\frac{\rho_{sl}}{\rho_l} = \frac{\frac{\gamma+1}{\gamma-1}\frac{P_s}{P_l} + 1}{\frac{P_s}{P_l} + \frac{\gamma+1}{\gamma-1}}. \tag{3.54}$$

The shock speed can be derived from Eqn. (3.53a) to obtain the expression:

$$S = \frac{u_s - \frac{\rho_l}{\rho_{sl}}u_l}{1 - \frac{\rho_l}{\rho_{sl}}}. \tag{3.55}$$

From Eqn. (3.53b), the following relation is obtained as

$$u_l - u_s = \sqrt{(P_s - P_l)\left(\frac{1}{\rho_l} - \frac{1}{\rho_{sl}}\right)}. \tag{3.56}$$

By substituting Eqn. (3.54) into Eqn. (3.56), the equation resulting from the shock resolution in the gas is

$$u_l - u_s = \sqrt{\frac{P_s - P}{\rho_l}\left(\frac{\frac{2}{\gamma-1}\left(\frac{P_s}{P_l} - 1\right)}{\frac{\gamma+1}{\gamma-1}\frac{P_s}{P_l} + 1}\right)} = \sqrt{\frac{2}{(\gamma-1)\rho_l}}\frac{P_s - P_l}{\sqrt{\left(\frac{\gamma+1}{\gamma-1}\frac{P_s}{P_l} + 1\right)P_l}} = \sqrt{\frac{2P_l}{(\gamma-1)\rho_l}}\frac{\frac{P_s}{P_l} - 1}{\sqrt{\frac{\gamma+1}{\gamma-1}\frac{P_s}{P_l} + 1}}. \tag{3.57}$$

In the solid, the jump relationships for the re-written Naviers equation eigensystem in (3.11a, 3.11b) are shown below.

$$(u_s - u_r)D = \frac{c^2}{E}(P_s - P_r), \tag{3.58a}$$

$$(P_s - P_r)D = E(u_s - u_r), \tag{3.58b}$$

where D refers to the shock speed in the solid. Multiplying the left-hand side of eqn.(3.58a) to the left-hand side of eqn.(3.58b) and similarly for the right-hand sides shows that $D = \pm c$. This is not unexpected as the discontinuity can only propagate along the characteristic line at the speed of the respective eigenvalues and in this case, the eigenvalues in the solid medium correspond to $\pm c$.

In combination with the equation from the gas medium, we have

$$\begin{cases} u_l - u_s = \sqrt{(P_s - P_l)\left(\frac{1}{\rho_l} - \frac{1}{\rho_{sl}}\right)}, \\ (u_s - u_r) = \frac{c}{E}(P_s - P_r). \end{cases} \tag{3.59}$$

The equations from Eqn. (3.59) combine to give the following result,

$$u_l - u_r = \sqrt{(P_s - P_l)\left(\frac{1}{\rho_l} - \frac{1}{\rho_{sl}}\right)} + \frac{c}{E}(P_s - P_r). \tag{3.60}$$

Re-arranging and squaring both sides, the above equation becomes

$$\left[\sqrt{(P_s - P_l)\left(\frac{1}{\rho_l} - \frac{1}{\rho_{sl}}\right)}\right]^2 = \left[\left(u_l - u_r + \frac{c}{E}P_r\right) - \frac{c}{E}P_s\right]^2. \tag{3.61}$$

Further manipulation leads to:

$$\frac{2}{(\gamma-1)\rho_l}\frac{(P_s - P_l)^2}{\left(\frac{\gamma+1}{\gamma-1}\frac{P_s}{P_l} + 1\right)} = \left(u_l - u_r + \frac{c}{E}P_r\right)^2 - \frac{2c}{E}\left(u_l - u_r + \frac{c}{E}P_r\right)P_s + \frac{c^2}{E^2}P_s^2. \tag{3.62}$$

The final equation is obtained via re-arranging the various terms in descending order in powers of P_s.

$$\frac{c^2}{E^2}\frac{\gamma+1}{\gamma-1}P_s^3+\left[-\frac{2c}{E}\left(u_l-u_r+\frac{c}{E}P_r\right)\left(\frac{\gamma+1}{\gamma-1}\right)+\frac{c^2}{E^2}P_l-\frac{2}{(\gamma-1)\rho_l}\right]P_s^2$$
$$+\left[\left(u_l-u_r+\frac{c}{E}P_r\right)^2\left(\frac{\gamma+1}{\gamma-1}\right)-\frac{2c}{E}\left(u_l-u_r+\frac{c}{E}P_r\right)P_l+\frac{4P_l}{(\gamma-1)\rho_l}\right]P_s+\left[\left(u_l-u_r+\frac{c}{E}P_r\right)^2P_l-\frac{2P_l^2}{(\gamma-1)\rho_l}\right]=0 \tag{3.63}$$

Due to the complexity of the equation, the software Mathematica is utilized in solving for the parameter, P_s which is the interface pressure. Multiple values of P_s are obtained from this equation. The true P_s has to obey the following conditions for the test cases in the next section:

1) $P_s>0$, (3.64a)

2) $P_s>\max(P_l,\ P_r)$ only in shock-shock interactions, (3.64b)

3a) $P_s<P_s^*$, *where* $u_l^2=\left(P_s^*-P_l\right)\left(\frac{1}{\rho_l}-\frac{1}{\rho_{sl}}\right)$ for shock-shock or shock-rarefraction interaction, (3.64c)

3b) $P_s<P_s^*$, *where* $u_l=\frac{2}{\gamma-1}\left[\sqrt{\frac{\gamma P_l}{\rho_l}}-\sqrt{\frac{\gamma P_s^*}{\rho_{sl}}}\right]$ for rarefraction-shock or rarefraction-rarefraction interaction. (3.64d)

The interface velocity is then obtained from

$$u_s=\frac{c}{E}\left(P_s-P_r\right)+u_r, \tag{3.65}$$

and the solid shock speed is given by

$$D=\frac{c^2}{E}\frac{\left(P_s-P_r\right)}{\left(u_s-u_r\right)}. \tag{3.66}$$

In essence, the whole plot can be determined from the following conditions,

$$U(x,t)=\begin{cases}P_l,u_l,\rho_l & if\ \ x-x_0<St,\\ P_s,u_s,\rho_{sl} & if\ \ St\le x-x_0<u_st,\\ P_s,u_s,\rho_r & if\ \ u_st\le x-x_0<Dt,\\ P_r,u_r,\rho_r & if\ \ x-x_0\ge Dt,\end{cases} \tag{3.67}$$

where x_0 is the initial location of the interface.

In water, the same Rankine-Hugoniot relations apply across the shock wave.

The main difference would be the difference in the EOS parameters. For water, the following relation holds,

$$\rho_{sl} = \rho_l \left(\frac{\overline{P_s}}{\overline{P_l}} \right), \quad \overline{P} = P + B, \tag{3.68}$$

And Eqn. (3.60) is also applicable to water. Re-arranging and squaring both sides yields

$$\left[\sqrt{\frac{\left(\overline{P_s} - \overline{P_l}\right)}{\rho_l} \left(1 - \left(\frac{\overline{P_l}}{\overline{P_s}} \right)^{\frac{1}{N}} \right)} \right]^2 = \left[\left(u_l - u_r + \frac{c}{E} P_r \right) - \frac{c}{E} P_s \right]^2 . \tag{3.69}$$

Thus, it leads to the final equation below given as

$$\left(\overline{P_l}\right)^{\frac{1}{N}} \left(\overline{P_s}\right)^{\frac{N-1}{N}} - \left(\overline{P_l}\right)^{\frac{N+1}{N}} \left(\overline{P_s}\right)^{\frac{-1}{N}} + \frac{c^2}{E^2} \rho_l P_s^{\,2} - \frac{2c}{E} \left(u_l - u_r + \frac{c}{E} P_r \right) P_s - \overline{P_s} + \overline{P_l} + \rho_l \left(u_l - u_r + \frac{c}{E} P_r \right)^2 = 0$$

. (3.70)

This equation is then solved to obtain P_s which obeys Conditions (1), (2) and (3a) above.

3.7.2 Fluid-Solid(Rarefaction-Shock)

Similarly, when a rarefraction wave impacts on the fluid-solid interface, a rarefraction wave is reflected back into the fluid media while a shock wave is transmitted into the solid media.

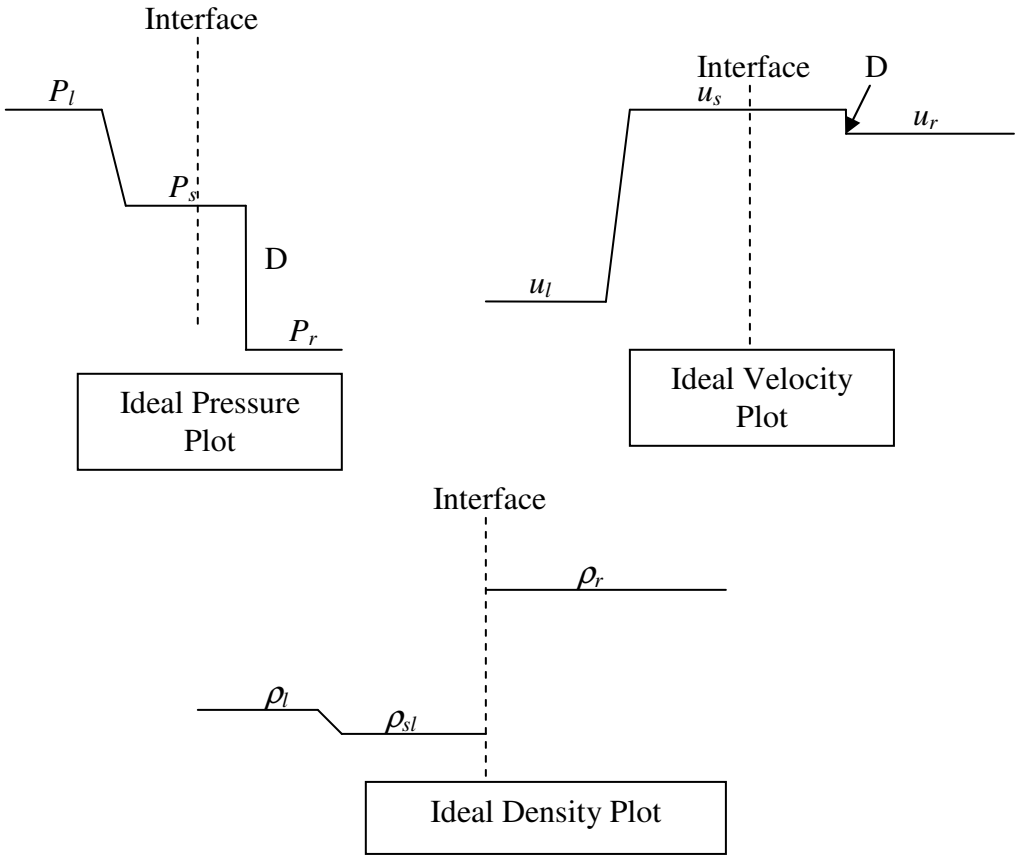

Figure 3-6: Ideal pressure, velocity and density plots for a rarefraction-shock interaction

When a rarefaction fan occurs in the gas medium, the isentropic gas law is applied to obtain the analytical solution. a_l and a^* denotes the sound speed on the left and right states bounding the left rarefraction wave,

$$a_l = \sqrt{\frac{\gamma P_l}{\rho_l}}, a^* = \sqrt{\frac{\gamma P_s}{\rho_{sl}}}, \tag{3.71}$$

$$u_l + \frac{2a_l}{\gamma - 1} = u_s + \frac{2a^*}{\gamma - 1}. \tag{3.72}$$

Combining the equation from the gas medium and the Naviers equation, we have

$$\begin{cases} u_l - u_s = \dfrac{2a^*}{\gamma-1} - \dfrac{2a_l}{\gamma-1}, \\ (u_s - u_r) = \dfrac{c}{E}(P_s - P_r), \end{cases} \tag{3.73}$$

From Eqn. (3.73), re-arrangement of the terms yields

$$u_l - u_r = \frac{c}{E}(P_s - P_r) + \frac{2a^*}{\gamma-1} - \frac{2a_l}{\gamma-1}. \tag{3.74}$$

Substituting Eqn. (3.71) into Eqn. (3.74), we have

$$u_l - u_r = \frac{c}{E}(P_s - P_r) + \frac{2}{\gamma-1}\left[\sqrt{\frac{\gamma P_s}{\rho_{sl}}} - \sqrt{\frac{\gamma P_l}{\rho_l}}\right], \tag{3.75}$$

using the isentropic law,

$$\rho_{sl} = \rho_l \left(\frac{P_s}{P_l}\right)^{\frac{1}{\gamma}}. \tag{3.76}$$

Next, Eqn. (3.76) is substituted into Eqn. (3.75) to yield, in terms of descending powers of P_s,

$$\left(\frac{2}{\gamma-1}\sqrt{\gamma\frac{P_l^{1/\gamma}}{\rho_l}}\right)P_s^{\frac{\gamma-1}{2\gamma}} + \frac{c}{E}P_s - \frac{2}{\gamma-1}\sqrt{\frac{\gamma P_l}{\rho_l}} - \frac{c}{E}P_r + u_r - u_l = 0. \tag{3.77}$$

Mathematica software was used to derive the multiple solutions to the equation. Some of the conditions for P_s in Section 3.7.1 applies here. The applicable conditions are Condition(1) and Condition(3b).

The plot of the analytical solution follows the rules below,

$$U(x,t) = \begin{cases} U_l & if\ x - x_0 < (u_l - a_l)t, \\ U_l\left(\dfrac{x-x_0}{t}\right) & if\ (u_l - a_l)t \le x - x_0 < (u_s - a^*)t, \\ U_{sl} & if\ (u_s - a^*)t \le x - x_0 < u_s t, \\ U_{sr} & if\ u_s t \le x - x_0 < Dt, \\ U_r & if\ x - x_0 \ge Dt, \end{cases} \tag{3.78}$$

where x_0 is the initial location of the interface. Similarly, for rarefraction wave in water, the same equations apply except for a different definition of a_l and a^* according to the Tate's equation which is the EOS for water. The relationships for Tate's Equation are

$$\left(\frac{\rho_{sl}}{\rho_l}\right)^N = \frac{P_s + B}{P_l + B}, \tag{3.79}$$

$$a_l = \sqrt{\frac{N(P_l + B)}{\rho_l}}, \quad a^* = \sqrt{\frac{N(P_s + B)}{\rho_{sl}}}. \tag{3.80}$$

Substituting Eqn. (3.80) into Eqn. (3.74), we have

$$u_l - u_r = \frac{c}{E}(P_s - P_r) + \frac{2}{N-1}\left[\sqrt{\frac{N(P_s + B)}{\rho_{sl}}} - \sqrt{\frac{N(P_l + B)}{\rho_l}}\right]. \tag{3.81}$$

And Eqn. (3.79) is substituted next into Eqn. (3.81), and the resulting Eqn. (3.81) is re-arranged in terms of descending powers of P_s to give,

$$\frac{2\sqrt{N}}{N-1}\sqrt{\frac{(P_l + B)^{1/N}}{\rho_l}}\left[P_s + B\right]^{\frac{N-1}{2N}} + \frac{c}{E}P_s - \frac{c}{E}P_r + u_r - u_l - \frac{2}{N-1}\sqrt{\frac{N(P_l + B)}{\rho_l}} = 0. \tag{3.82}$$

This equation is then solved to obtain P_s.

3.7.3 Fluid-solid(Rarefraction-rarefraction)

There are certain problems where a rarefraction wave at the fluid-solid interface results in a rarefraction wave reflected back into the fluid media and a very weak shock/rarefraction wave is transmitted into the solid media.

To solve for rarefraction wave in the solid, the same Naviers equation is used and the overall equation for the interface pressure turns out to be the same as in Eqn. (3.77) for gas and Eqn. (3.82) for water. The plot in this case follows,

$$U(x,t)=\begin{cases} U_l & if\ x-x_0<(u_l-a_l)t, \\ U_l\left(\dfrac{x-x_0}{t}\right) & if\ (u_l-a_l)t\le x-x_0<(u_s-a^*)t, \\ U_{sl} & if\ (u_s-a^*)t\le x-x_0<u_s t, \\ U_{sl} & if\ u_s t\le x-x_0<(u_s+C)t, \\ U_r\left(\dfrac{x-x_0}{t}\right) & if\ (u_s+C)t\le x-x_0<(u_r+C)t, \\ U_r & if\ x-x_0\ge(u_r+C)t, \end{cases} \tag{3.83}$$

where *C* is the sound speed in the solid and x_0 is the initial location of the interface.

Chapter 4 Results and Discussion

4.1 Test cases

In order to validate the one-dimensional fluid-solid code constructed using Naviers equation, the code is used to run a series of test cases exploring various scenarios and the numerical results are then compared with the analytical solution. In a few of the test cases, the numerical solution(Naviers equation) would be compared to the published results in Tang and Sotiropoulos (1999).

4.1.1 Properties of metal

The properties of a typical stainless steel grade AISI Type 431are chosen for the solid. These properties are taken from Davies (1997).

Metal	Young's Modulus(E), 10^6 psi	Bulk Modulus(K), 10^6 psi	Shear Modulus(G), 10^6 psi	Poisson ratio
Mild Steel	30.7	24.5	11.9	0.291
Stainless Steel(2Ni-18Cr) AISI Type 431	31.2	24.1	12.2	0.283

Table 4-1 Properties of metals in imperial units at 20^0C

Upon conversion to SI units,

Metal	Young's Modulus(E), GPa	Bulk Modulus(K), GPa	Shear Modulus(G), GPa	Poisson ratio
Mild Steel	211.67	168.92	82.04	0.291
Stainless Steel(2Ni-18Cr) AISI Type 431	215.116	166.16	84.12	0.283

Table 4-2 Properties of metals in SI units at 20^0C

From another table, the typical density of AISI Type 431 alloy is $7.7\,{}^{g}\!/_{cm^3}$.

Designation		Composition(max),wt%						
UNIS No.	AISI Type	C	Mn	Si	P	S	Cr	Ni
S43100	431	0.20	1.00	1.00	0.040	0.030	15.00-17.00	1.25-2.50

Table 4-3 Composition of AISI type 431 Steel

The properties of the steel modeled in Tang and Sotiropoulos (1999) were derived under the specific conditions of the Hydro-elasto-plastic model(i.e. high pressure and large deformation with plasticity effect) and these properties are different from those under normal conditions. For the Naviers equation, it was based on the assumption of small strains in the elastic zone. Hence, the steel properties used in the modeling had to be different due to the different fundamentals of each model. In the results below, the various quantities are non-dimensionalised with respect to the following reference parameters. $\rho_{ref} = 1000\,{}^{kg}/_{m^3}$, $P_{ref} = 10^5\,Pa$, $L_{ref} = 1.0m$, $u_{ref} = \sqrt{\frac{P_{ref}}{\rho_{ref}}}$ and $t_{ref} = \frac{L_{ref}}{u_{ref}}$.

4.2 Test cases in comparison with published results

Case 4.1(Gas-Steel): This case is similar to the Riemann Problem(III) case in Tang and Sotiropoulos (1999) whereby a high pressure gas impacts at a high velocity on an unmoving steel, resulting in a strong shock transmitted through the steel and a strong shock reflected back into the gas medium. However, the properties of steel used in this paper differ from that of the typical steel grade used in the present model. The reason being that in the Hydro-elasto-plastic model used by Tang and Sotiropoulos, the model assumes that the steel is under very high pressure and behaves almost like a fluid, effectively describing the transition between solid state and liquid state. The initial conditions are $u_l = 50.0$, $p_l = 10000.0$, $\rho_l = 0.05$; $u_r = 0.0$, $p_r = 1.01325$. The density of the steel differs for the models: $\rho_r = 7.8$ for Hydro-elasto-plastic model and

$\rho_r = 7.7$ for the Naviers equation model. The CFL number is chosen as 1.0 for both models. The computational domain is from 0.0 to 10.0 and the initial interface is located at 5.0. Both ends of the domain are kept open. The computation time is $4.45x10^{-3}$ for both models. The number of grid points for both models is 2201 in lieu of the large computational domain. Figs. 4-1a to 4-1c depict the comparison between the Naviers equation model and the analytical solution. Figs 4-1d to Figs 4-1f show the comparison between the Naviers equation model and the Hydro-elasto-plastic model. As seen from Figs 4-1d and 4-1e, the elastic shock is travelling at a slightly faster speed in the Hydro-elasto-plastic model as compared to the Naviers equation model. In fact, the numerical values of the steel shock speed are $C_{HEP} = 656.5580$ and $C_{NE} = 599.7806$ for the Hydro-elasto-plastic model and Naviers equation model, respectively. This is physically consistent with the basic fundamentals of the models. From the results, it is shown that the interface in the Naviers equation model has moved only a few mesh spaces. This is expected as there should only be small deformations of the elastic solid.

Case 4.2(water-steel): This case is taken from Tang and Sotiropoulos (1999)'s Riemann Problem II where water at high velocity going from left to right and pressure impacts on incoming steel moving from right to left. The initial conditions are $u_l = 30.0$, $p_l = 25000.0$, $\rho_l = 1.0$; $u_r = -30.0$, $p_r = 25.0$. The density of the steel differs for the models: $\rho_r = 7.8$ for Hydro-elasto-plastic model and $\rho_r = 7.7$ for the Naviers equation model. The CFL number is chosen as 1.0 for both models. The computational domain is from 0.0 to 10.0 and the initial interface is located at 5.0. Both ends of the domain are kept open. The computation time is $4.45x10^{-3}$ for both models. The grid points for both models is 2201 in lieu of the large computational

domain. From Figs 4-2d to 4-2f, the Hydro-elasto-plastic model is able to capture an additional shockwave(plastic shock) apart from the elastic shockwave compared to the Naviers equation model. The Naviers equation model (Figs 4-2a to 4-2c) is insufficient to capture the characteristics of plastic flow as elastic-plastic behaviour is essentially non-linear and the Naviers equation is derived from the linear elastic relationship between stress and strain.

4.3 Non Reflection test cases

These test cases are specially designed such that the shock refraction on the interface does not produce any reflected wave. The ideal interface algorithm should be robust and accurately transmit shock forces to media on either side. In order to prove the robustness and accuracy of the fluid-solid interface characteristics equations, non-reflection or shock impedance matching cases are computed. If the interface algorithm under-predicts or over-predicts any physical quantities, non-physical humps would appear at the interface location as seen in Liu et al (2003).

Case 4.3(Gas-steel): The initial conditions are $u_l = 2.78789$, $p_l = 10000.0$, $\rho_l = 0.05$; $u_r = 0.0$, $p_r = 1.01325$, $\rho_r = 7.7$. The CFL number remains at 1.0 and the initial interface location is 5.0. The computational domain is from 0.0 to 10.0 and the initial interface is located at 5.0. Both ends of the domain are kept open. The number of grid points is 2201 in lieu of the large computational domain. The computation time is $4.45x10^{-3}$. As can be seen from Figs 4-3a to 4-3c, there are no visible non-physical humps at the interface location, indicating the accuracy and robustness of the interface algorithm.

Case 4.4(Water-steel): The initial conditions are $u_l = 6.96346$, $p_l = 25000.0$, $\rho_l = 1.0$; $u_r = 0.0$, $p_r = 25.0$, $\rho_r = 7.7$. The CFL number remains at 1.0 and the initial interface location is 5.0. The computational domain is from 0.0 to 10.0 and the initial interface is located at 5.0. Both ends of the domain are kept open. The number of grid points is 2201 in lieu of the large computational domain. The computation time is $4.45x10^{-3}$. Again, from Figs. 4-4a to.4-4c, no non-physical humps were spotted.

4.4 Other test cases involving gas-solid compressible flows

More gas-solid compressible flow case scenarios are designed in order to validate the effectiveness of the Naviers equation model in simulating shocks/rarefraction waves in steel when coupled to a fluid such as gas. The numerical solutions are compared to the analytical solutions.

Case 4.5: In this case, gas at moderate pressure and moderate velocity impacts on a still steel. The initial conditions for this case are $u_l = 20.0$, $p_l = 1000.0$, $\rho_l = 0.2$; $u_r = 0.0$, $p_r = 1.0$, $\rho_r = 7.7$, CFL=1.0. The number of grid points is 2201. The program is run till $4.45x10^{-3}$. The solution for this scenario should see shockwaves occurring in both the gas medium and the steel. Figs. 4-5a to 4-5c show good matching of the numerical solution to the exact solution.

Case 4.6: The solution type of this case is a rarefaction wave in gas and a shock wave in solid. The initial conditions for this case are $u_l = -10.0$, $p_l = 1800.0$, $\rho_l = 0.2$; $u_r = 0.0$, $p_r = 1.0$, $\rho_r = 7.7$, CFL=1.0. The program is run to $4.45x10^{-3}$.

The number of grid points is 2201. From Figs. 4-6a to 4-6c, the numerical solution is a good fit to the analytical solution and the locations of the rarefraction wave and shock wave are accurately calculated/captured by the numerical solution.

Case 4.7: The solution type of this case is a rarefaction wave in gas and a rarefaction wave in solid. The initial conditions for this case are $u_l = -10.0$, $p_l = 8000.0$, $\rho_l = 1.2$; $u_r = 0.0$, $p_r = 8000.0$. The computation is run to a final time of 3.45×10^{-3}. From Figs. 4-7a, a pressure undershoot is seen near the rarefraction wave in the steel.

4.5 Other test cases involving water-solid compressible flows

Similarly, more test cases for water-steel are designed to test the solid phase algorithm in the simulation of shockwaves/rarefraction waves accurately.

Case 4.8: The solution type is also a shock wave in water and a shock wave in solid. The initial conditions are $u_l = 30.0$, $p_l = 25000.0$, $\rho_l = 1.0$, $u_r = -10.0$, $p_r = 25.0$, $\rho_r = 7.7$, CFL=1.0. The number of grid points is 2201. The program is run to $4.45x10^{-3}$. From Figs. 4-8a to 4-8c, it seems that the numerical solution follows the exact solution closely.

Case 4.9: In this case, the initial pressure of the water stream impacting the steel is quite low. The initial conditions for this case are $u_l = 10.0$, $p_l = 800.0$, $\rho_l = 1.0$ $u_r = 0.0$, $p_r = 1.0$, $\rho_r = 7.7$, CFL=1.0. The number of grid points is 2201. The program is run till $4.45x10^{-3}$. From Figs. 4-9a to 4-9c, the numerical solution of the Naviers equation model compares favorably well with the analytical solution. In fact, the Naviers equation model seems to have no difficulty in modeling water-steel cases

with low pressure. On the other hand, the Hydro-elasto-plastic model is unable to simulate for cases with $p_l < 750.0$.

Case 4.10: In this test case, a rarefraction wave occurs in the water and a shock occurs in the solid. The initial conditions are $u_l = -10.0$, $p_l = 25000.0$, $\rho_l = 1.0$, $u_r = 0.0$, $p_r = 25$, $\rho_r = 7.7$, CFL=1.0. The number of grid points is kept to 2201. The program is run to $4.45x10^{-3}$. From Figs. 4-10a to 4-10c, the numerical solution is very close to the analytical solution and is able to accurately simulate the locations of the rarefraction and shock waves in the water and solid media, respectively.

Case 4.11: The solution type is a rarefraction wave in water and a rarefraction wave in solid. The initial conditions are $u_l = -10.0$, $p_l = 30000.0$, $\rho_l = 1.0$, $u_r = 0.0$, $p_r = 25000$, $\rho_r = 7.7$, CFL=1.0 The number of grid points is 2201. The program is run till $3.45x10^{-3}$. As seen in Case 4.7, there is also a pressure undershoot near the rarefraction wave in the steel in Fig. 4-11a; this pressure undershoot is magnified in this case as both the Tait's equation and the Naviers equation is quite stiff. From Lin and Ballmann (1993a), the authors see a family of centered plastic waves as the form of the rarefraction wave in solid material. Since the Naviers equation only considers the elasticity of materials, it is insufficient to effectively model the rarefraction waves in the solid. Plasticity effects would have to be included in order to model rarefraction waves in solid as was done in Lin and Ballmann (1993a).

4.6 Mesh Refinement test

Case 4.12: For a gas-solid scenario, the initial conditions are $u_l = 50.0$, $p_l = 10000.0$, $\rho_l = 0.05$; $u_r = 0.0$, $p_r = 1.01325$ and $\rho_r = 7.7$. The program is run till $4.45x10^{-3}$. The mesh size is varied in order to determine the effect of mesh refinement on the numerical solution. Three mesh sizes were used. As seen from Fig. 4-12, as the mesh resolution increases, the shock in the solid steepens as expected in usual mesh refinement exercises.

Case 4.13: In water-solid cases, given the following initial conditions, $u_l = 30.0$, $p_l = 25000.0$, $\rho_l = 1.0$, $u_r = 0.0$, $p_r = 25.0$, $\rho_r = 7.7$, the computation is run till $3.45x10^{-3}$ with CFL=1.0 for three mesh sizes. From Fig. 4-13, it is noted that shock steepening occurs as mesh resolution increases, similar to Case 4.11.

4.7 Water shock tube test

Case 4.14: This case is similar to the 1D case study in Tang and Huang (1996). At the right end of the tube, instead of a rigid end, a steel structure is placed at the end before the rigid wall. The properties of a typical steel grade AISI type 431 were used for the simulation. The shock tube setup is illustrated in the figure below.

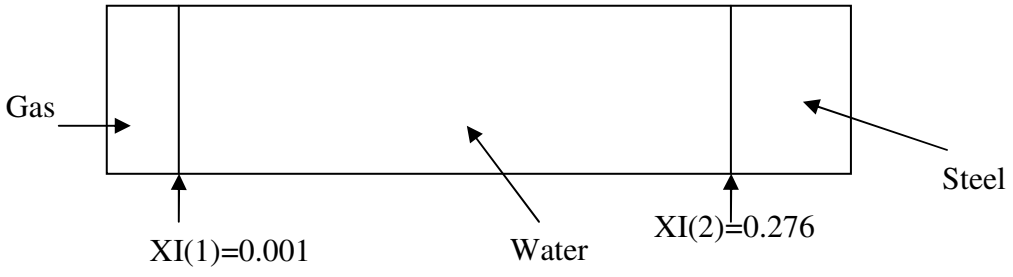

Figure 4-14: Schematic Diagram of water shock tube problem with steel

The whole domain is from $x = 0$ to $x = 0.3$. The total number of cells is 3000. The initial conditions are: $\rho_g = 0.070735$, $u_g = 0.0$, $P_g = 1006.929853$, $\rho_w = 1.0$, $u_w = 0.0$, $P_w = 1.01325$, $\rho_s = 7.7$, $u_s = 0.0$, $P_s = 1.0$. The program is run till $3.00x10^{-2}$.

The Modified Schmidt's model for cavitation (Xie et al.(In Press))is added to the fluid-solid algorithm in order to simulate the cavitation which occurs in the process. The gas-water-solid cavitation plot in Fig. 4-14a was compared with the case(Fig.4-14b) in which the right-end boundary is a reflecting wall. In the latter case, the computational domain was from $x = 0$ to $x = 0.276$ and the total number of cells was 2760 with the same initial conditions and computed for the same length of time. As seen from Fig. 4-14c which displays the overlapping plots, the first peak pressure is around the same but for the case with steel structure, it is noted that the pressure pulses drop to a lower mean value compared to the case with rigid boundary. Also, there appear to be less number of cavitation zones in the case with steel structure.

However, the present computation is based on a simple, one-dimensional model, ignoring possible secondary flow effects and hence, it may not truly explain all the features of a water shock tube flow problem. The experimental results of the paper from Wardlaw et al. (2000) seem to show that the pressure pulses on the cylinder wall is much lower for the deformable cylinder compared to the rigid cylinder. The same effect is also noted in our 1D computation in Fig. 4-14c even though the case in the above-mentioned paper was a three-dimensional experiment. However, work on extension to multi-dimensions is recommended in order to further validate the gas-water-solid algorithm in simulating unsteady cavitation and the effect of cavitation collapse on different solid structures.

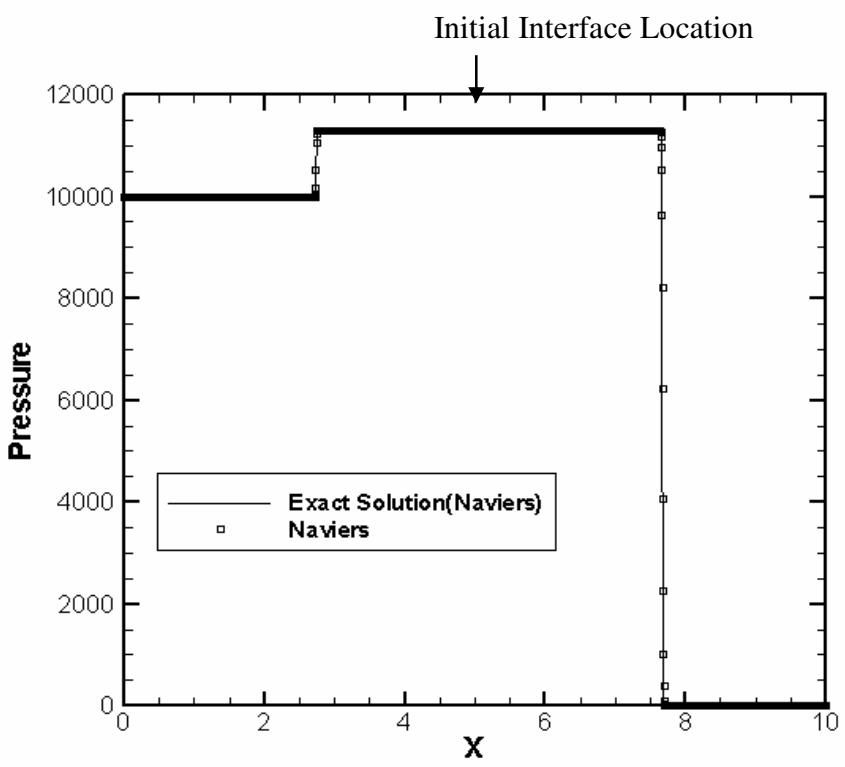

Figure 4-1a: The distribution of pressure obtained for comparison against the analytical solution (Case 4.1 Gas-solid)

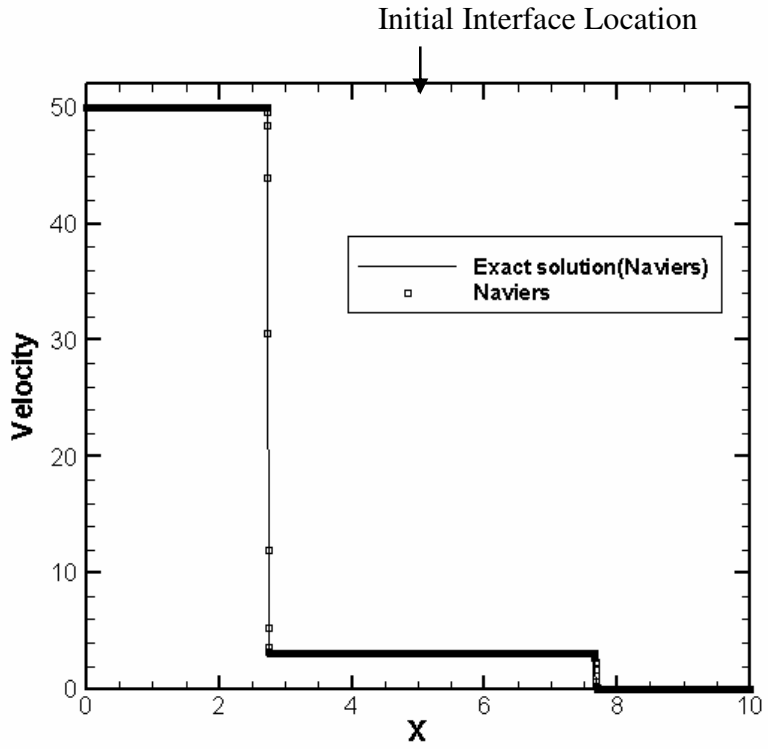

Figure 4-1b: The distribution of velocity obtained for comparison against the analytical solution (Case 4.1 Gas-solid)

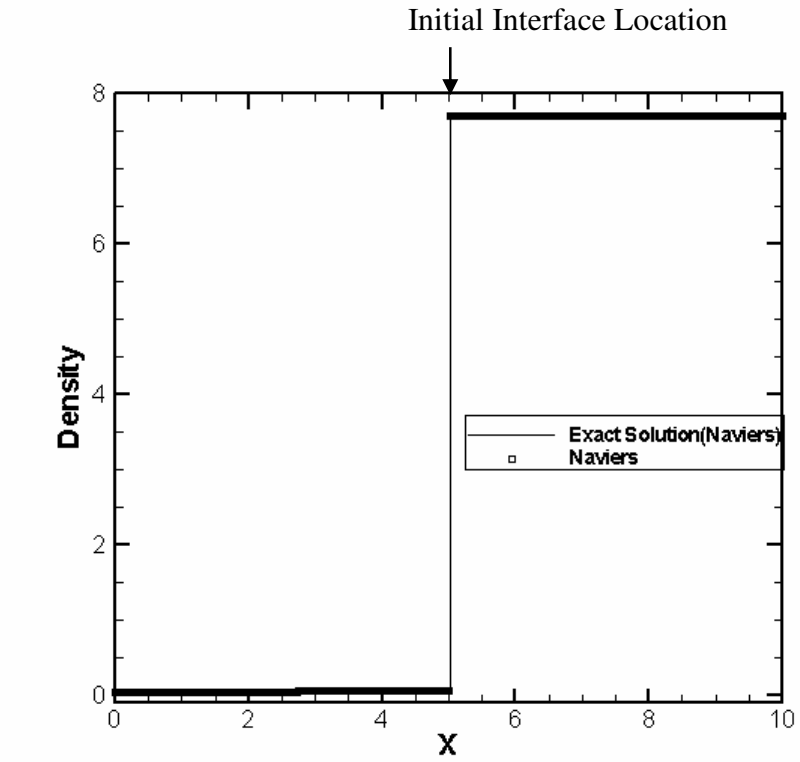

Figure 4-1c: The distribution of density obtained for comparison against the analytical solution (Case 4.1 Gas-solid)

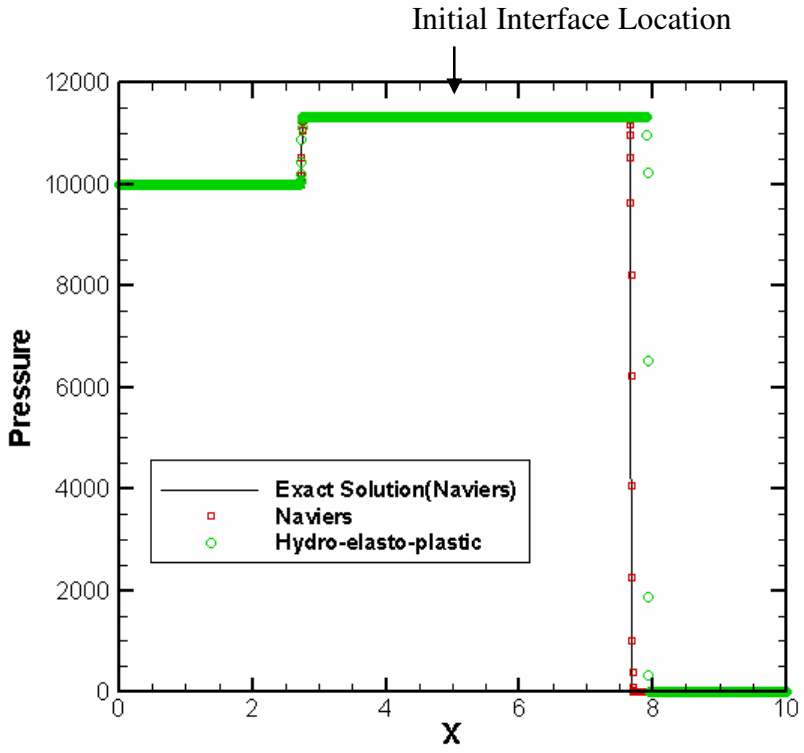

Figure 4-1d: The distribution of pressure obtained for comparison between Naviers equation and Hydro-elasto-plastic models

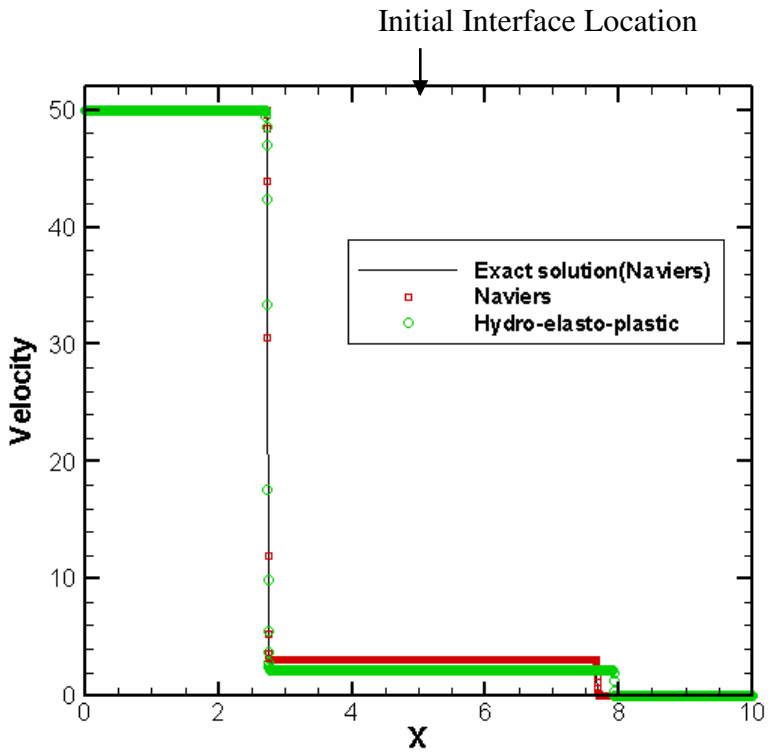

Figure 4-1e: The distribution of velocity obtained for comparison between Naviers equation and Hydro-elasto-plastic models

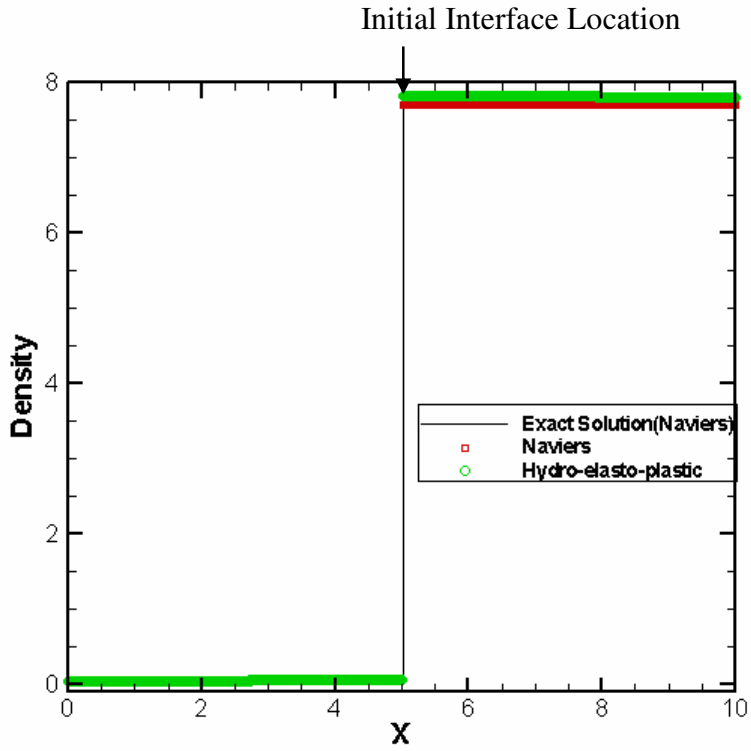

Figure 4-1f: The distribution of density obtained for comparison between Naviers equation and Hydro-elasto-plastic models

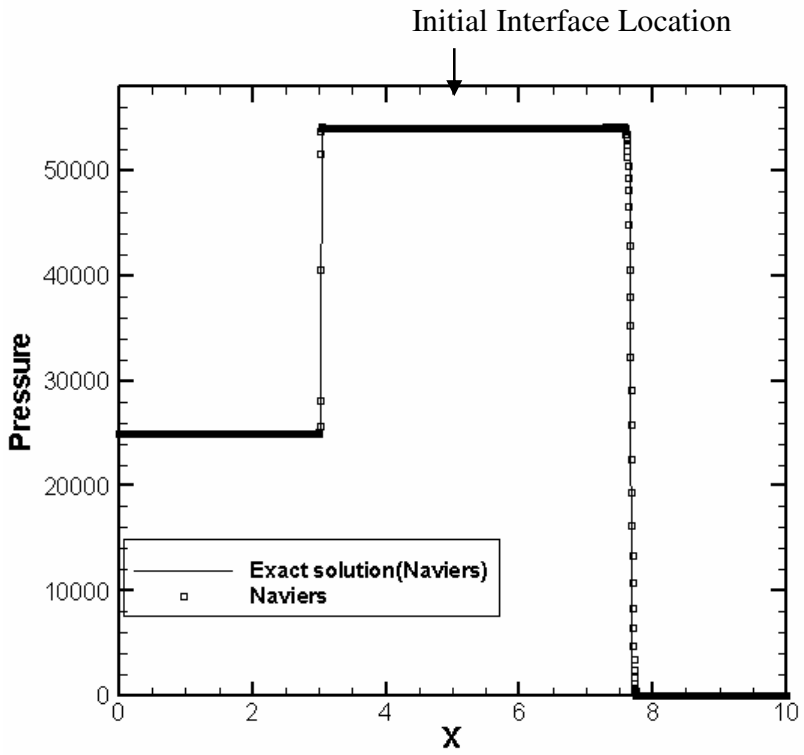

Figure 4-2a: The distribution of pressure obtained for comparison against the analytical solution (Case 4.2 Water-solid)

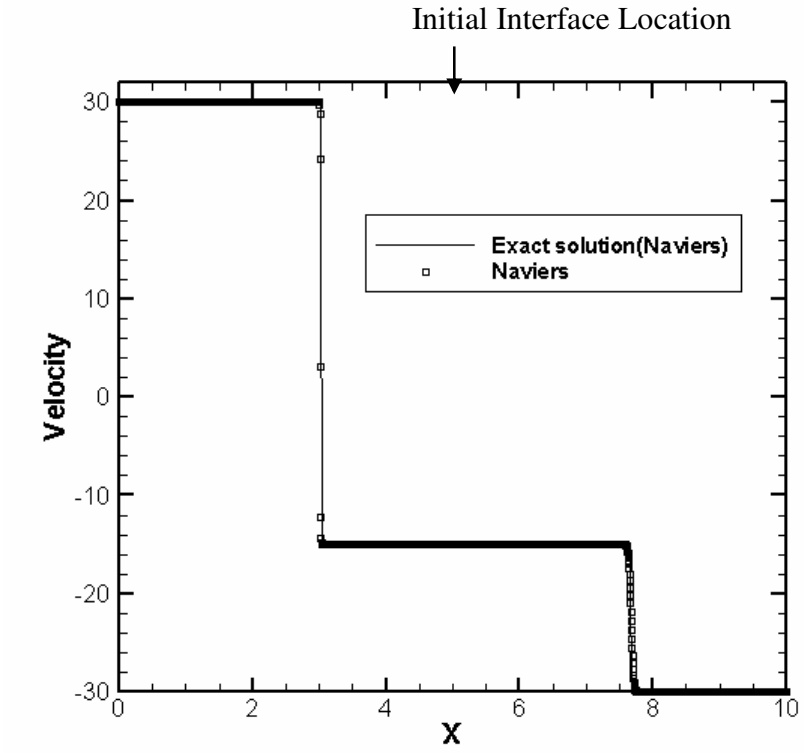

Figure 4-2b: The distribution of velocity obtained for comparison against the analytical solution (Case 4.2 Water-solid)

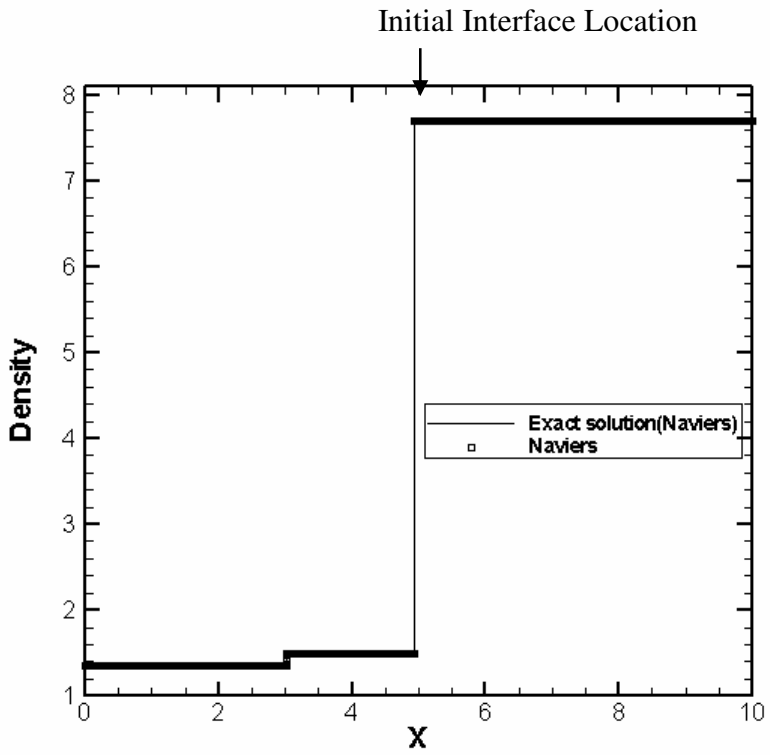

Figure 4-2c: The distribution of density obtained for comparison against the analytical solution (Case 4.2 Water-solid)

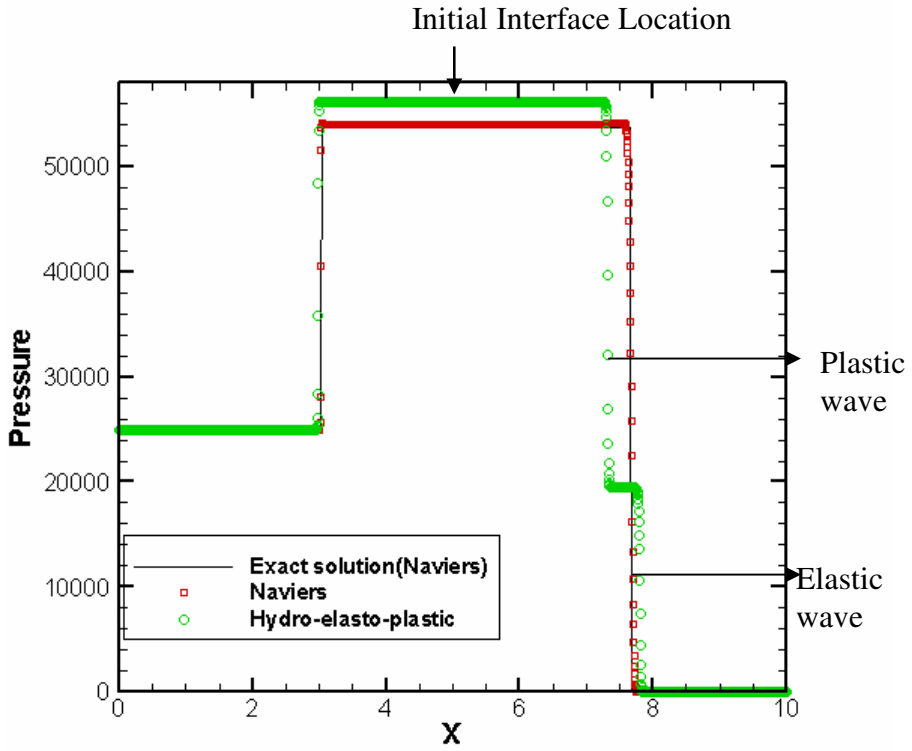

Figure 4-2d: The distribution of pressure obtained for comparison between Naviers equation and Hydro-elasto-plastic models

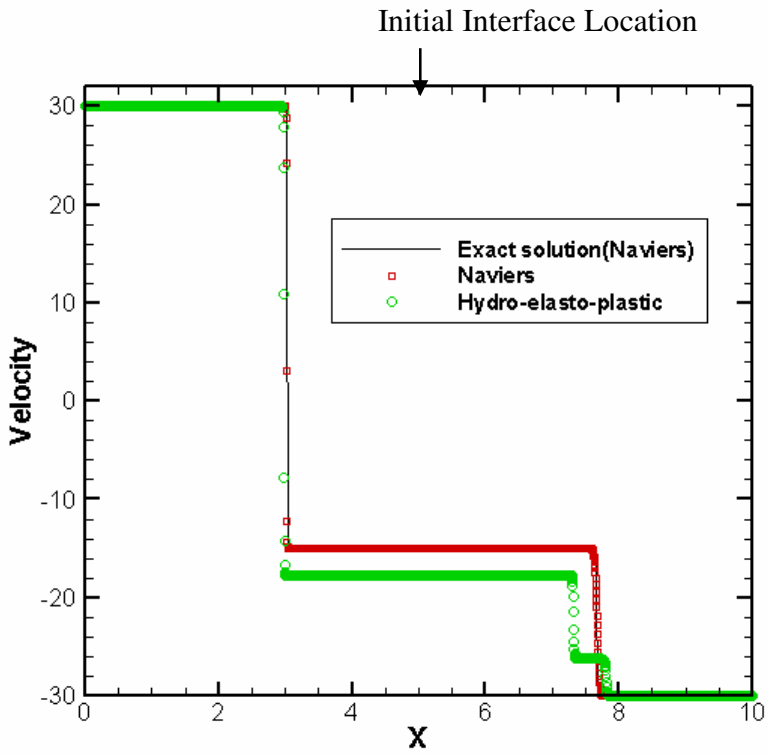

Figure 4-2e: The distribution of velocity obtained for comparison between Naviers equation and Hydro-elasto-plastic models

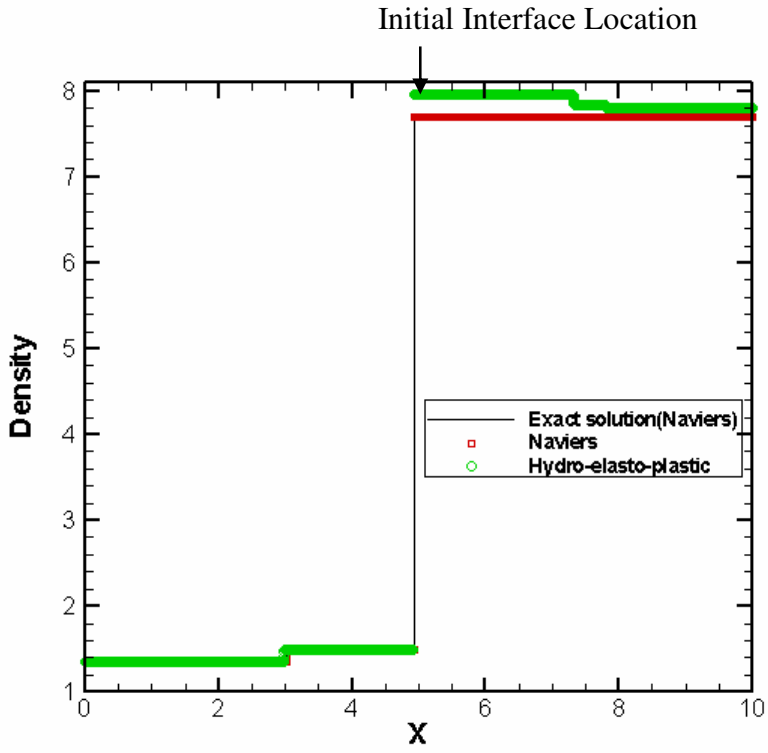

Figure 4-2f: The distribution of velocity obtained for comparison between Naviers equation and Hydro-elasto-plastic models

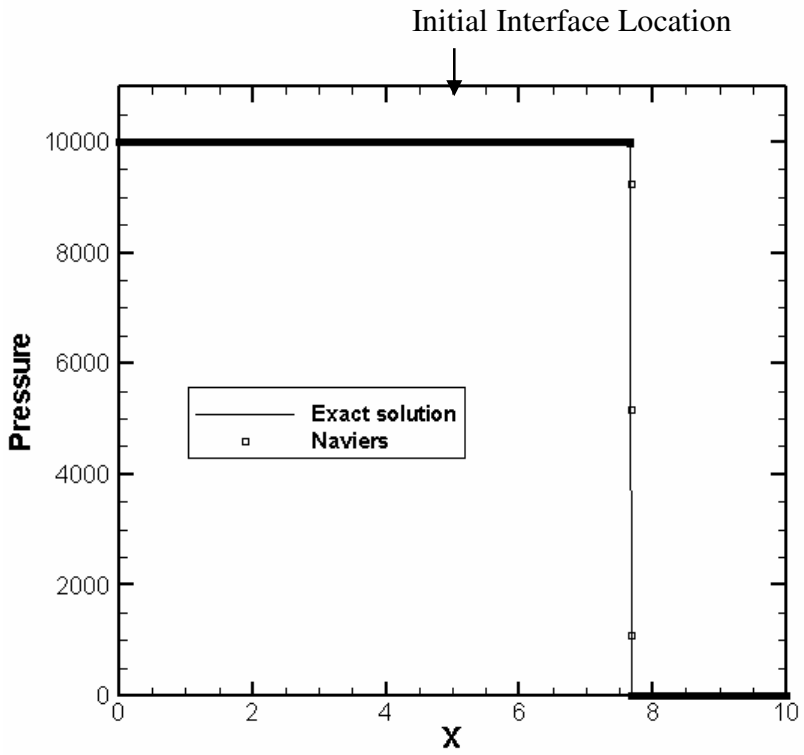

Figure 4-3a: The pressure profile for Case 4.3 Gas-Solid shock impedance problem

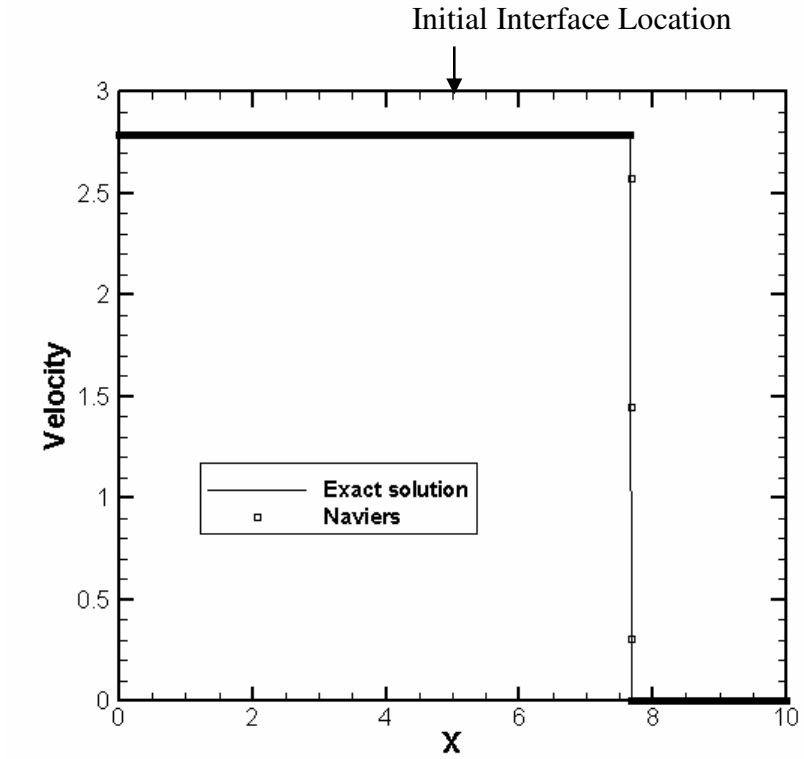

Figure 4-3b: The velocity profile for Case 4.3 Gas-Solid shock-impedance problem

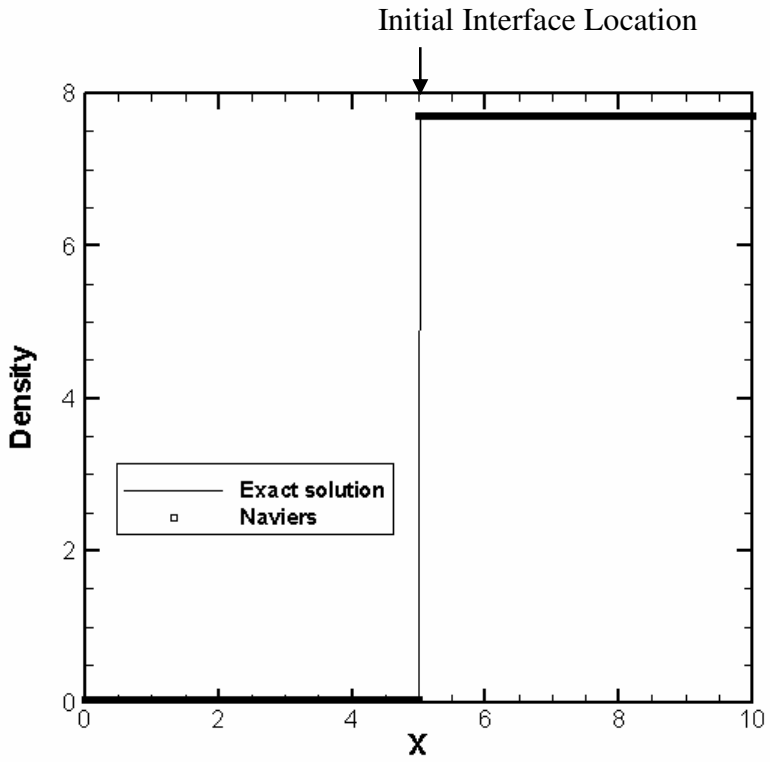

Figure 4-3c: The density profile for Case 4.3 Gas-Solid shock-impedance problem

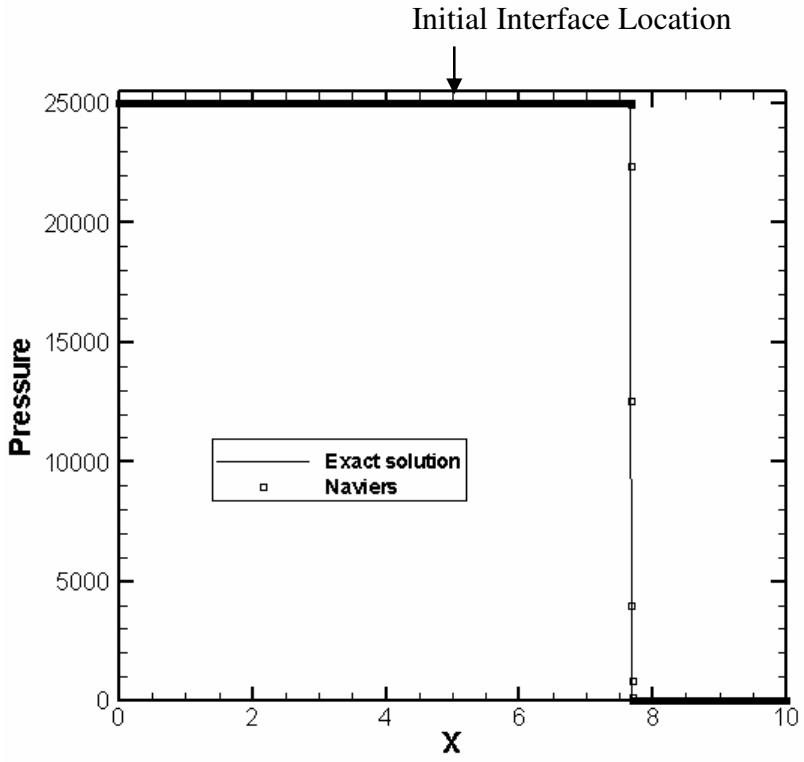

Figure 4-4a: The pressure profile for Case 4.4 Water-Solid shock impedance problem

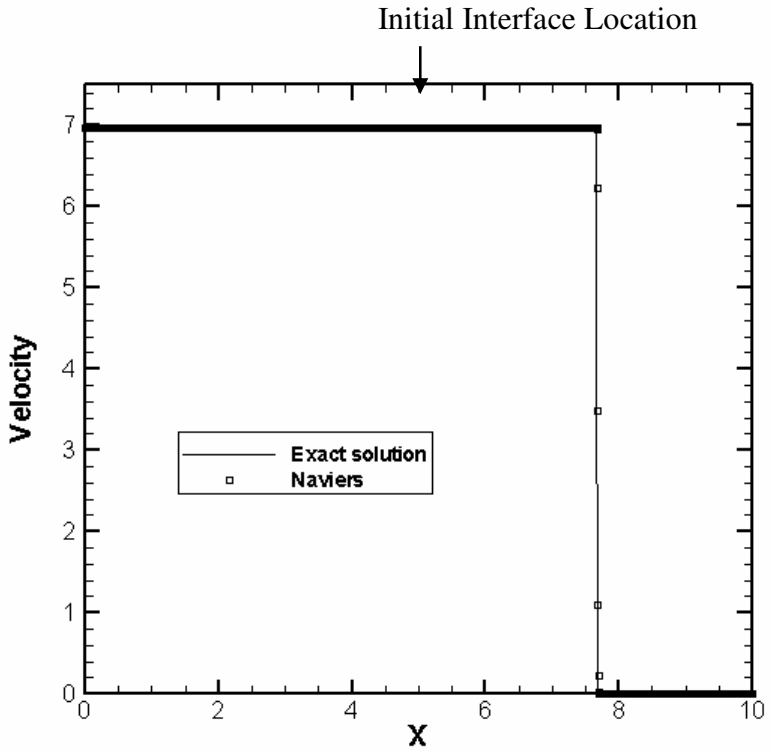

Figure 4-4b: The velocity profile for Case 4.4 Water-Solid shock impedance problem

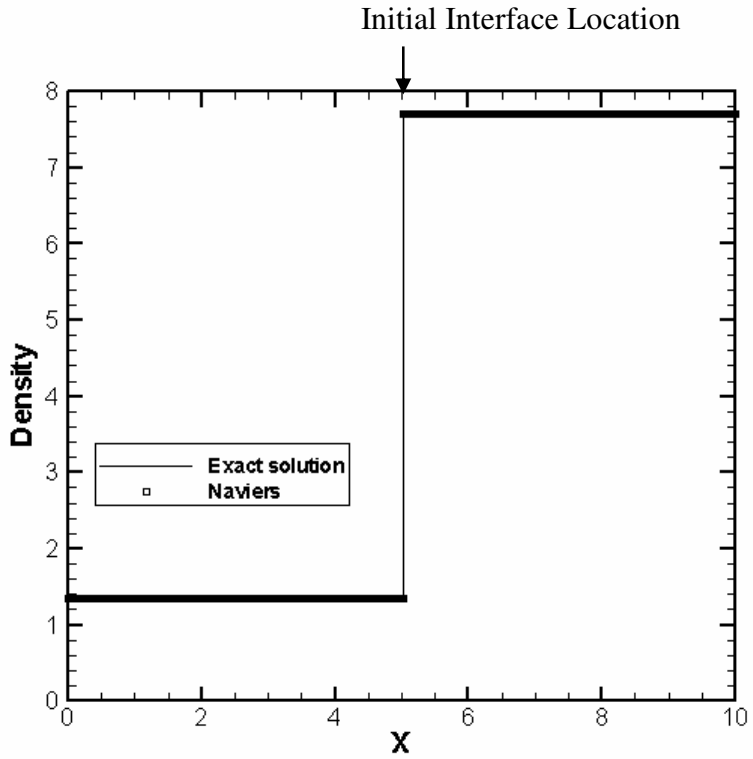

Figure 4-4c: The density profile for Case 4.4 Water-Solid shock impedance problem

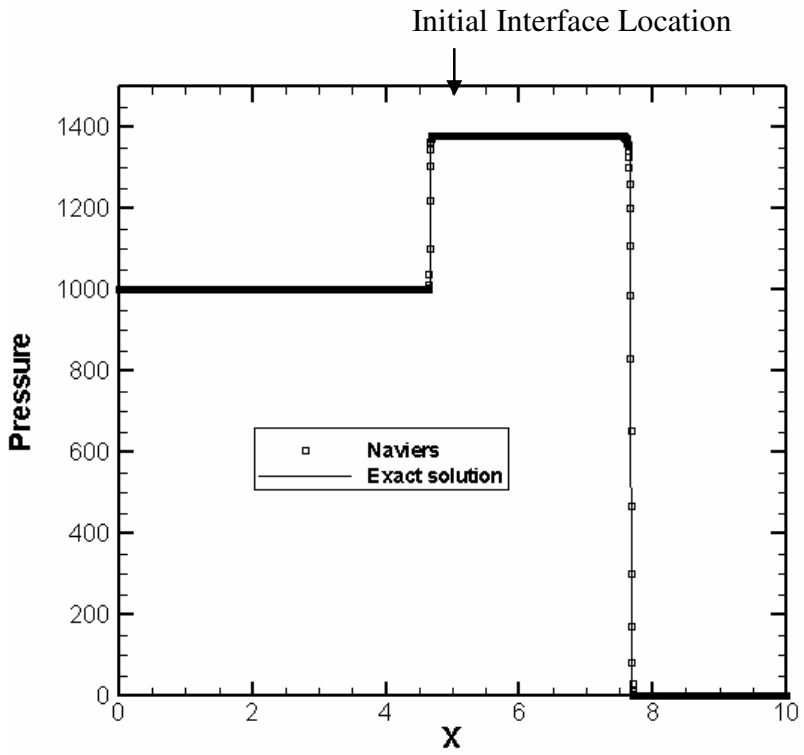

Figure 4-5a: The distribution of pressure obtained for comparison against the analytical solution (Case 4.5 Gas-solid)

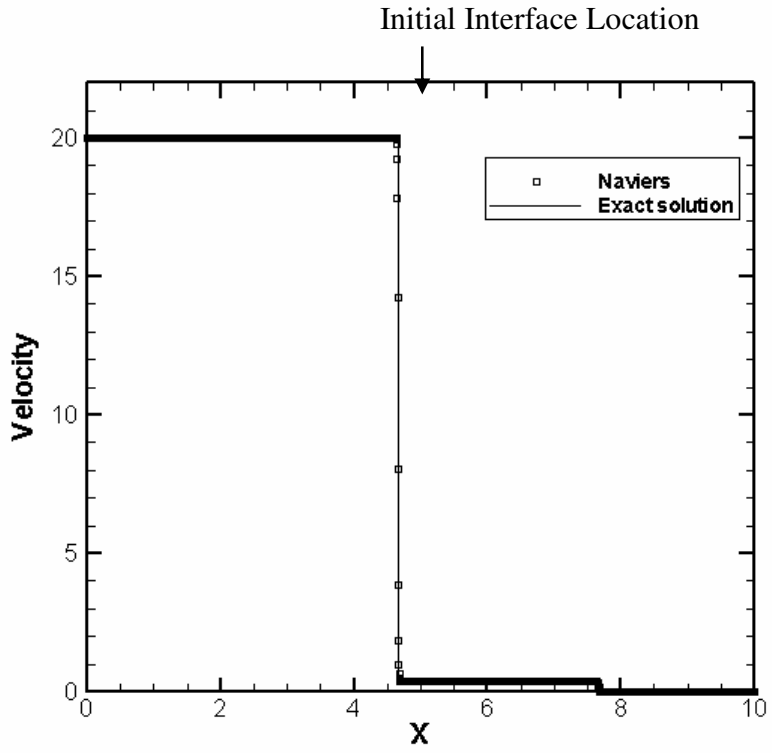

Figure 4-5b: The distribution of velocity obtained for comparison against the analytical solution (Case 4.5 Gas-solid)

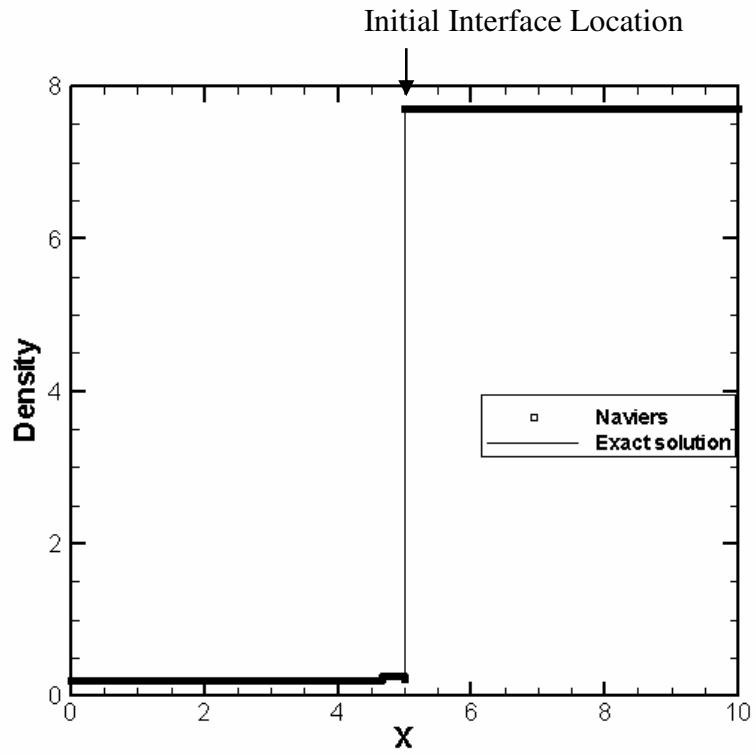

Figure 4-5c: The distribution of density obtained for comparison against the analytical solution (Case 4.5 Gas-solid)

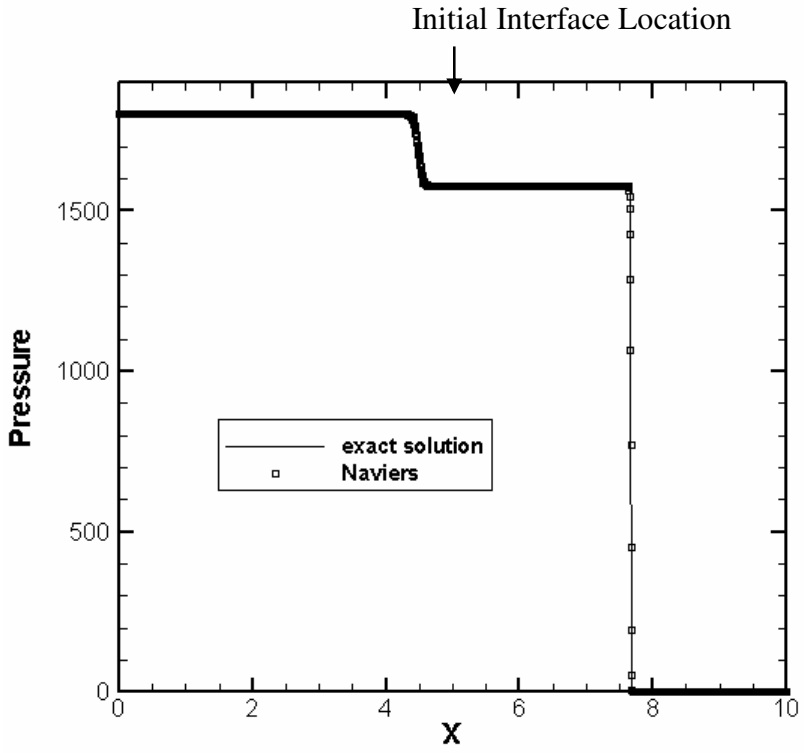

Figure 4-6a: The distribution of pressure obtained for comparison against the analytical solution (Case 4.6 Gas-solid)

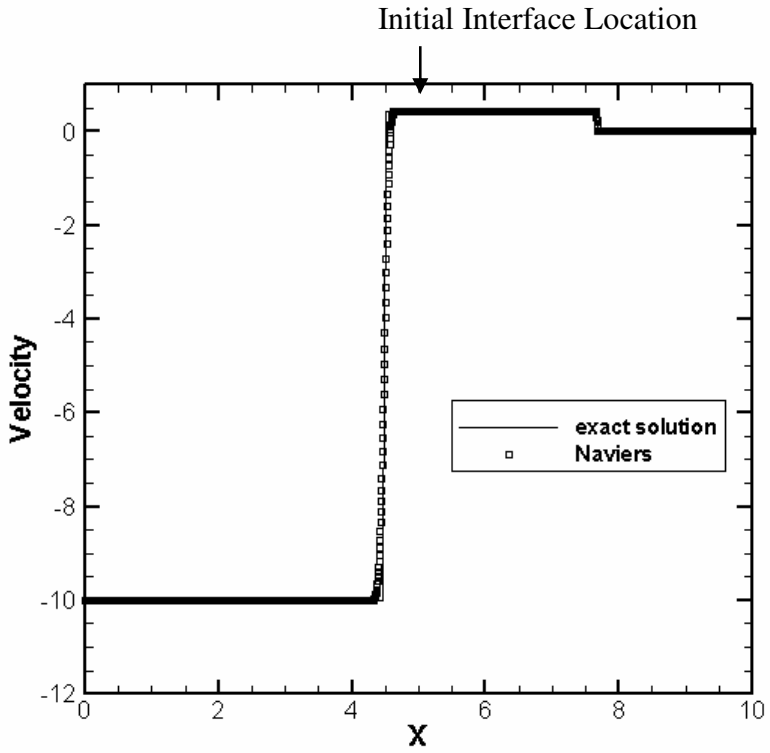

Figure 4-6b: The distribution of velocity obtained for comparison against the analytical solution (Case 4.6 Gas-solid)

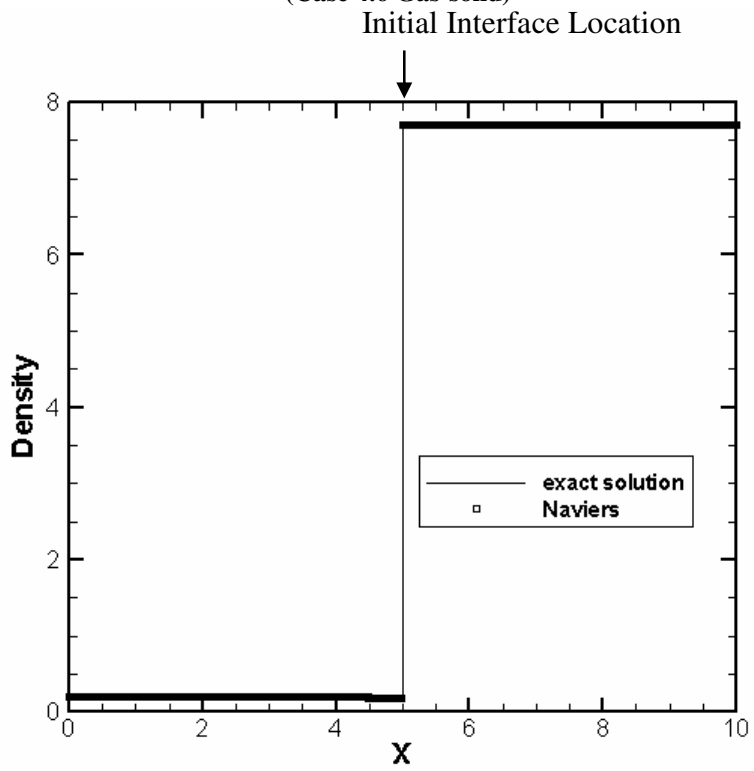

Figure 4-6c: The distribution of density obtained for comparison against the analytical solution (Case 4.6 Gas-solid)

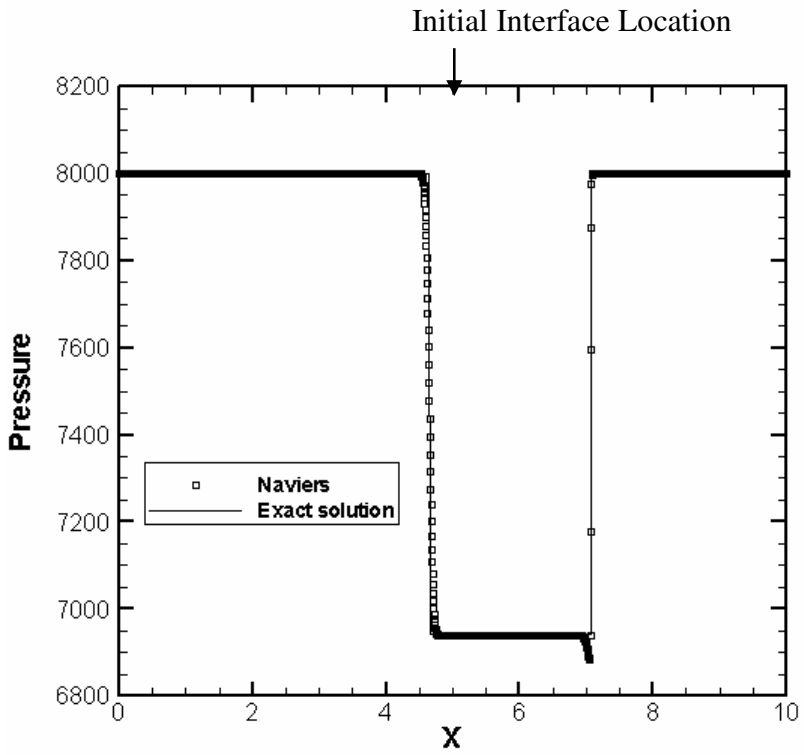

Figure 4-7a: The distribution of pressure obtained for comparison against the analytical solution (Case 4.7 Gas-solid)

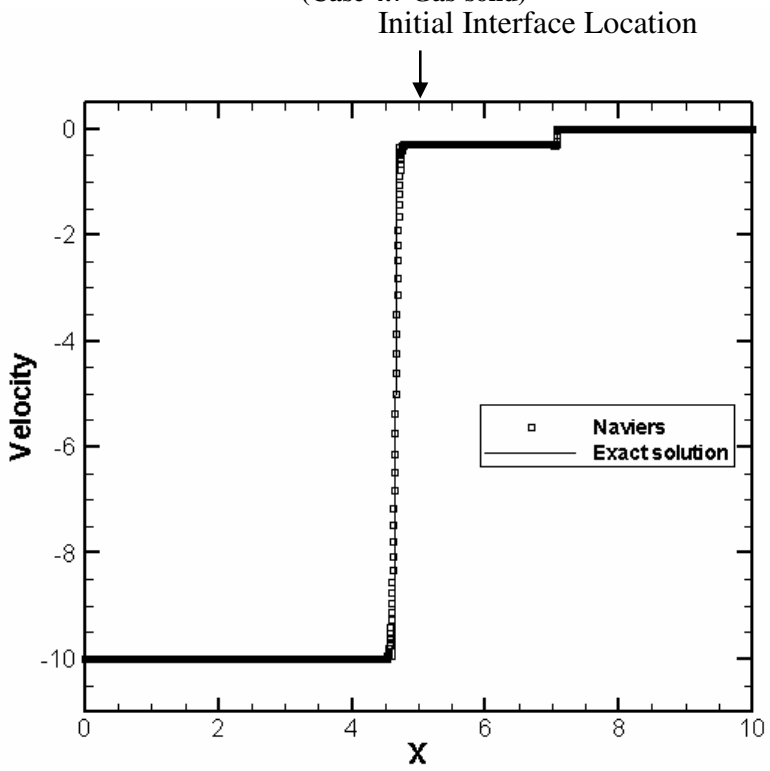

Figure 4-7b: The distribution of velocity obtained for comparison against the analytical solution (Case 4.7 Gas-solid)

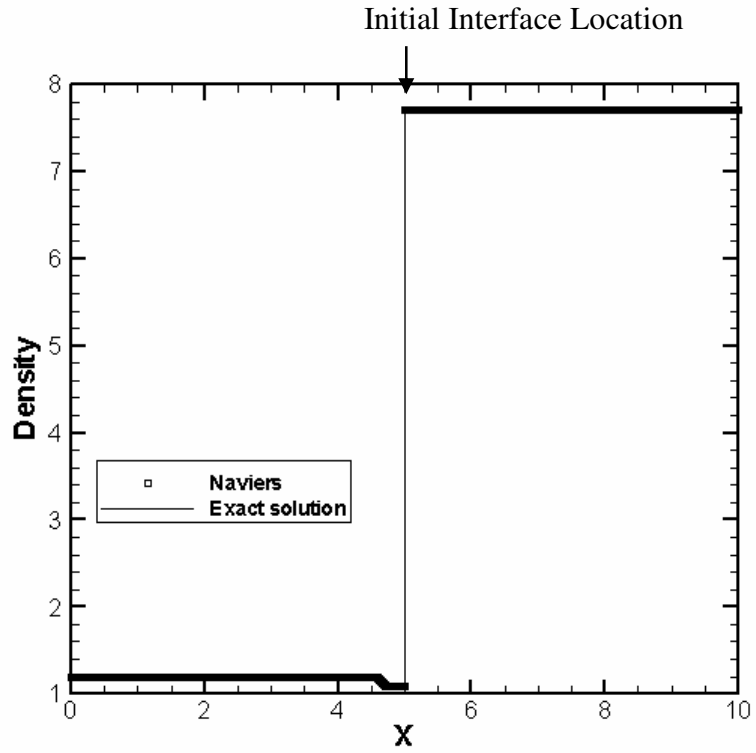

Figure 4-7c: The distribution of density obtained for comparison against the analytical solution (Case 4.7 Gas-solid)

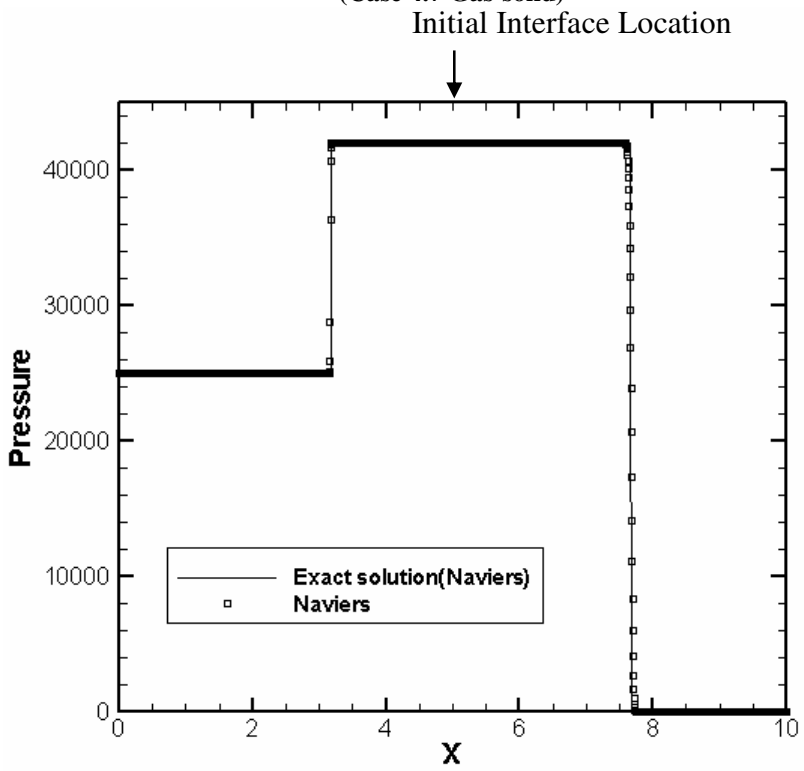

Figure 4-8a: The distribution of pressure obtained for comparison against the analytical solution (Case 4.8 Water-solid)

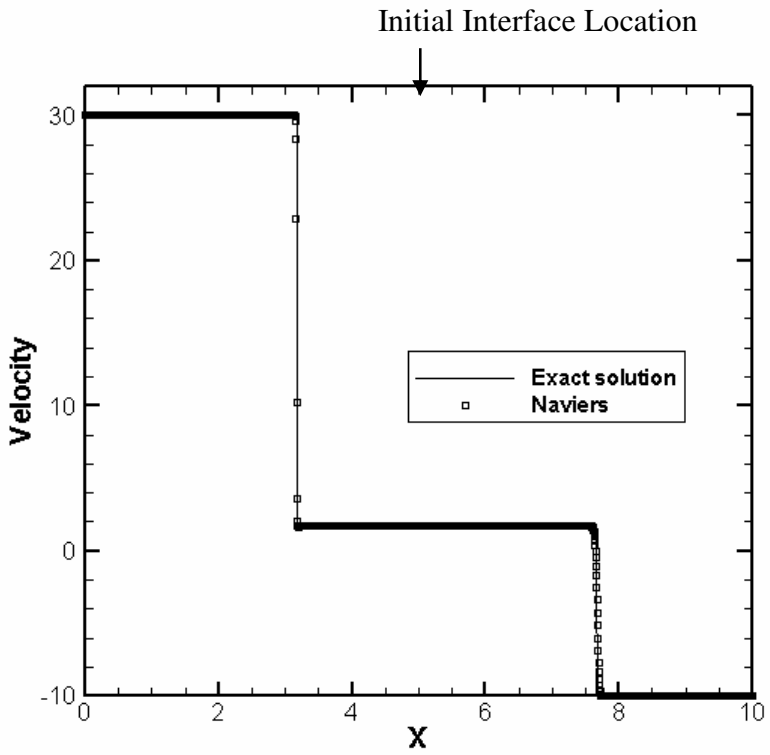

Figure 4-8b: The distribution of velocity obtained for comparison against the analytical solution (Case 4.8 Water-solid)

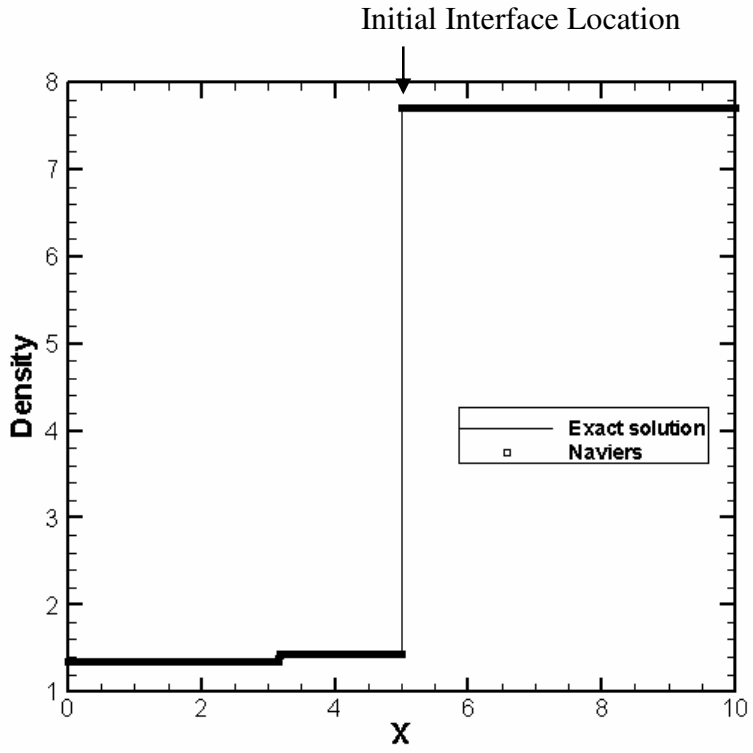

Figure 4-8c: The distribution of density obtained for comparison against the analytical solution (Case 4.8 Water-solid)

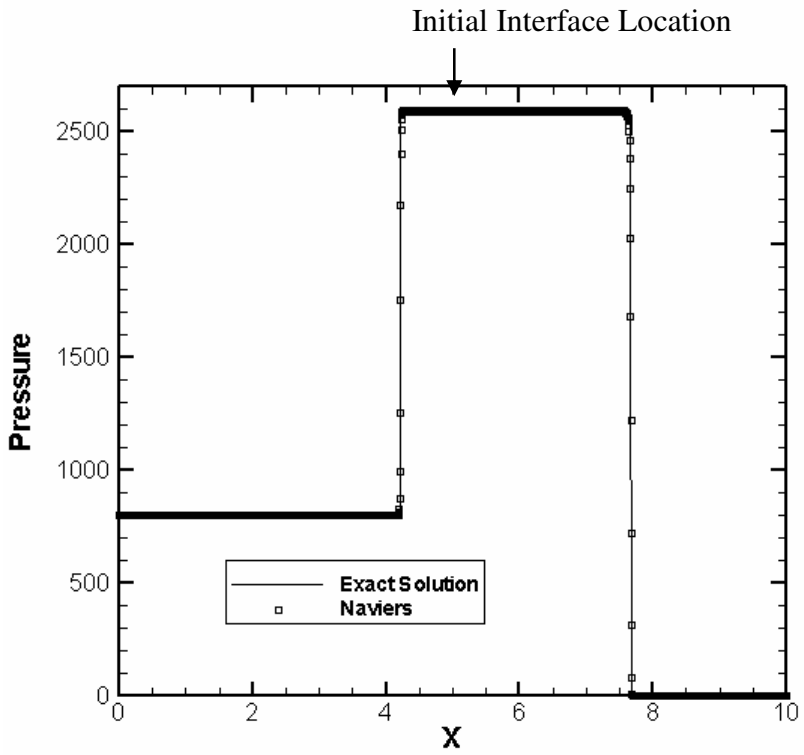

Figure 4-9a: The distribution of pressure obtained for comparison against the analytical solution (Case 4.9 Water-solid)

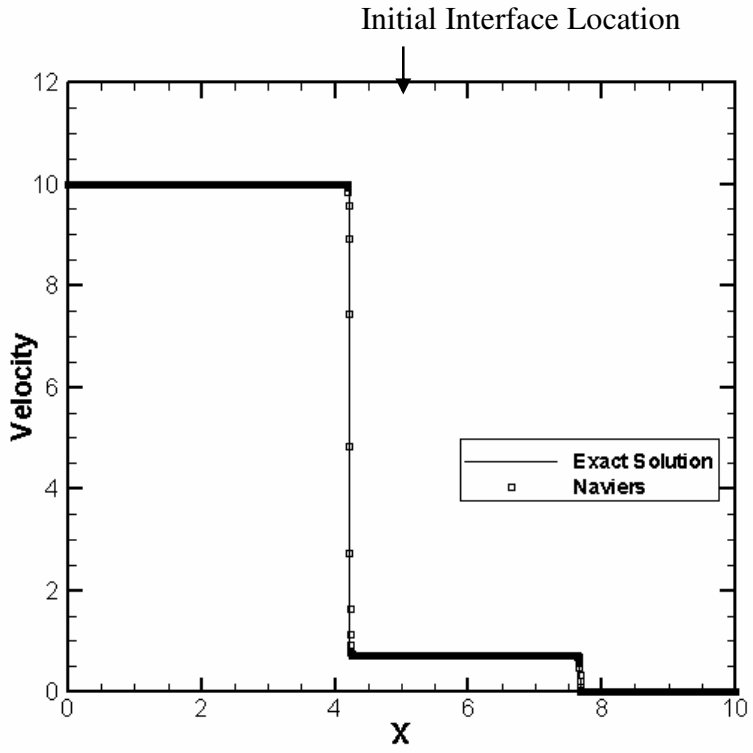

Figure 4-9b: The distribution of velocity obtained for comparison against the analytical solution (Case 4.9 Water-solid)

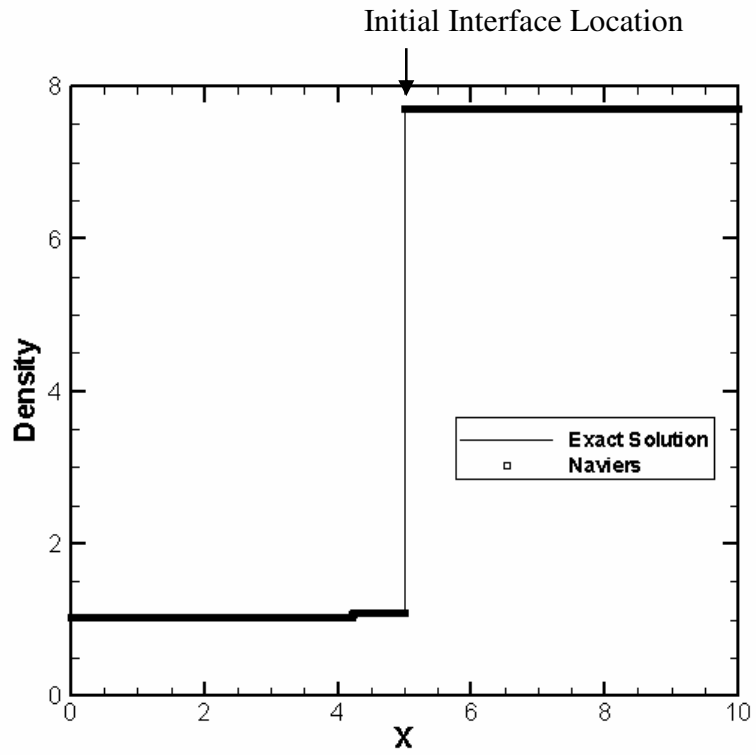

Figure 4-9c: The distribution of density obtained for comparison against the analytical solution (Case 4.9 Water-solid)

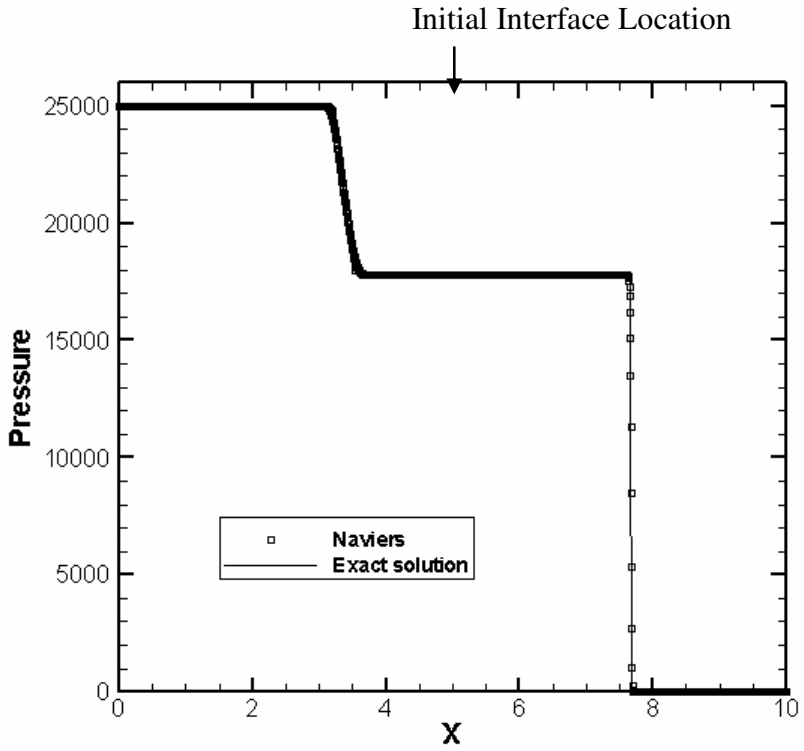

Figure 4-10a: The distribution of pressure obtained for comparison against the analytical solution (Case 4.10 Water-solid)

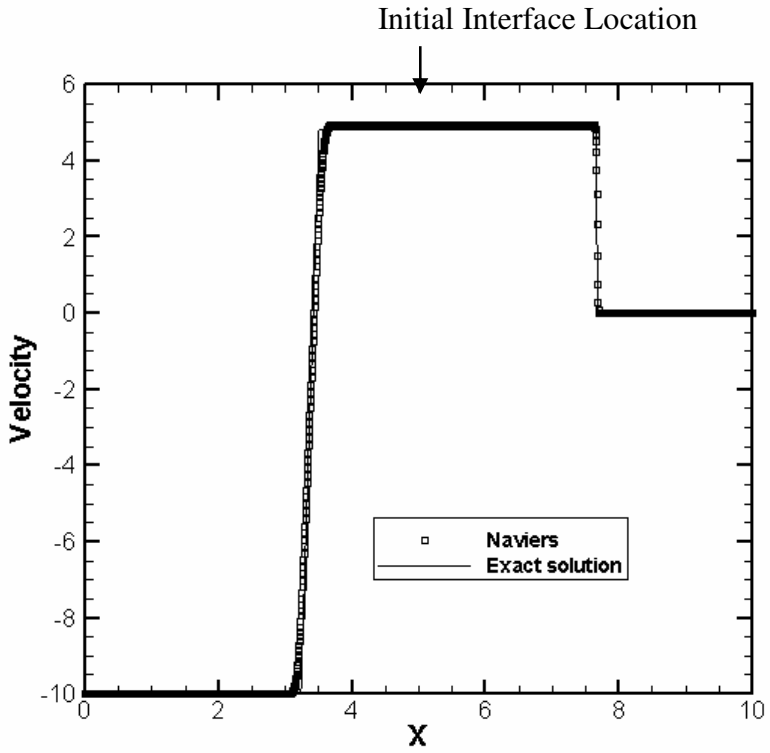

Figure 4-10b: The distribution of velocity obtained for comparison against the analytical solution (Case 4.10 Water-solid)

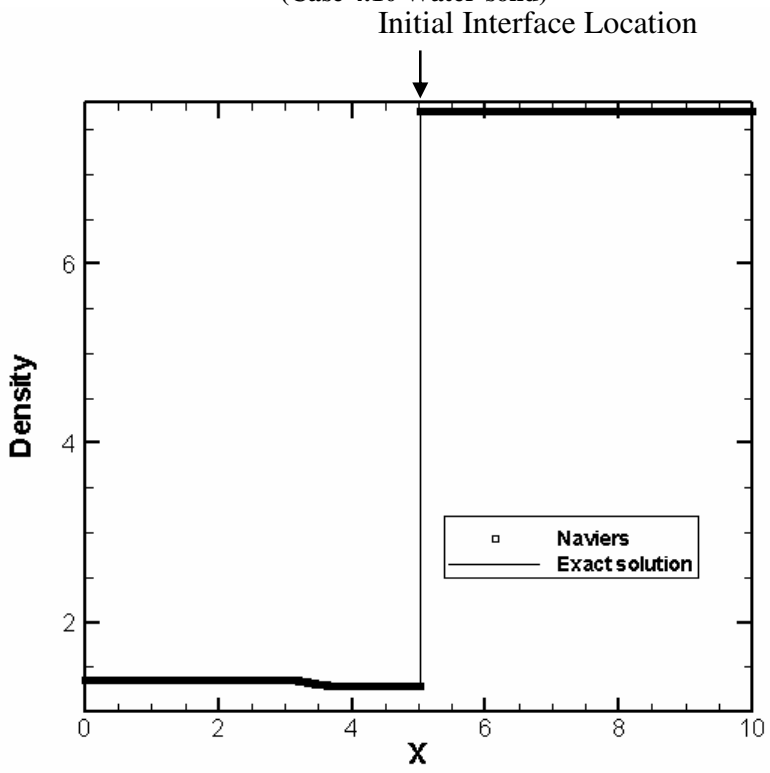

Figure 4-10c: The distribution of density obtained for comparison against the analytical solution (Case 4.10 Water-solid)

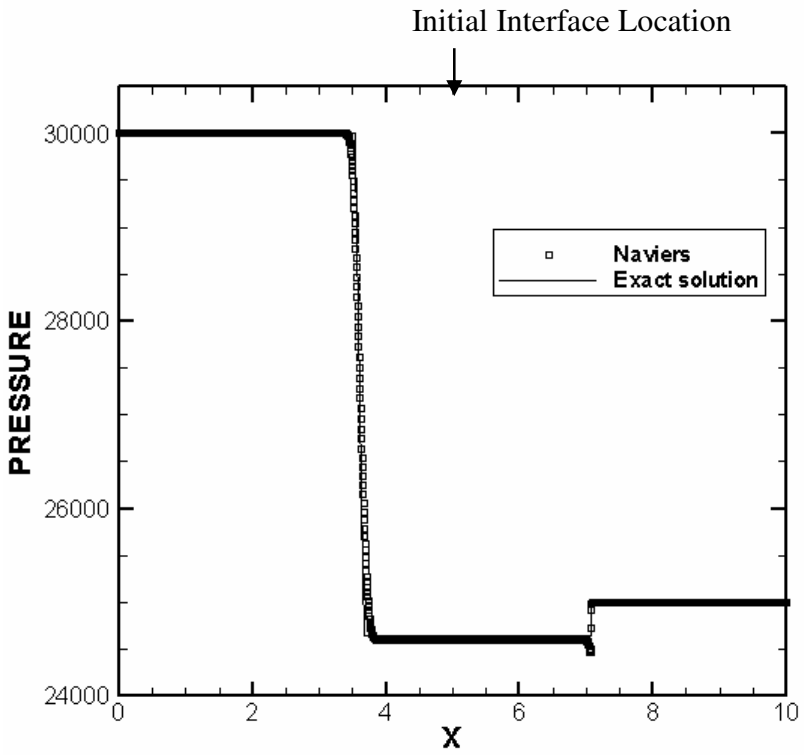

Figure 4-11a: The distribution of pressure obtained for comparison against the analytical solution (Case 4.11 Water-solid)

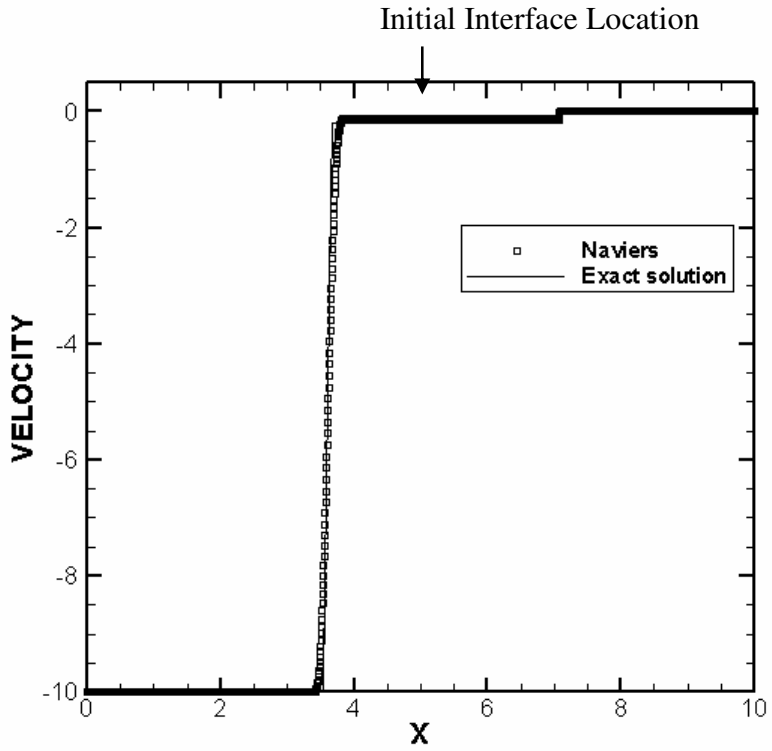

Figure 4-11b: The distribution of velocity obtained for comparison against the analytical solution (Case 4.11 Water-solid)

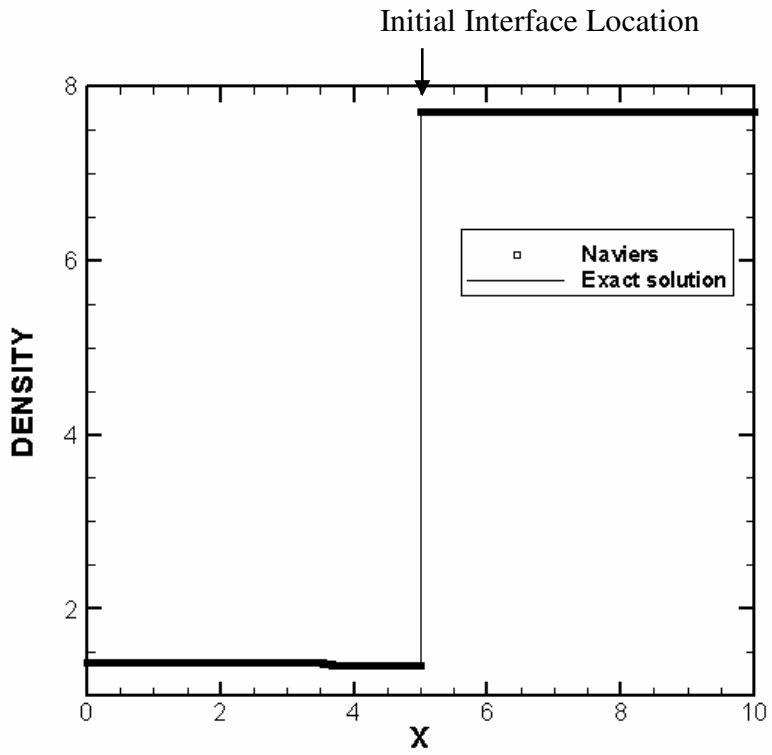

Figure 4-11c: The distribution of density obtained for comparison against the analytical solution (Case 4.11 Water-solid)

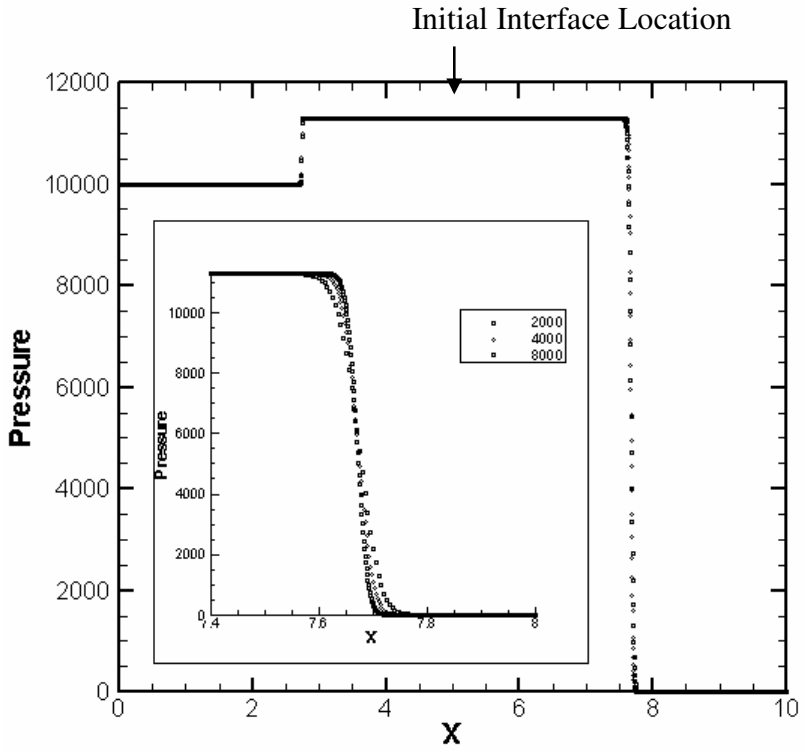

Figure 4-12: Mesh refinement of the pressure profile for gas-solid (Mesh sizes: 2000, 4000, 8000)

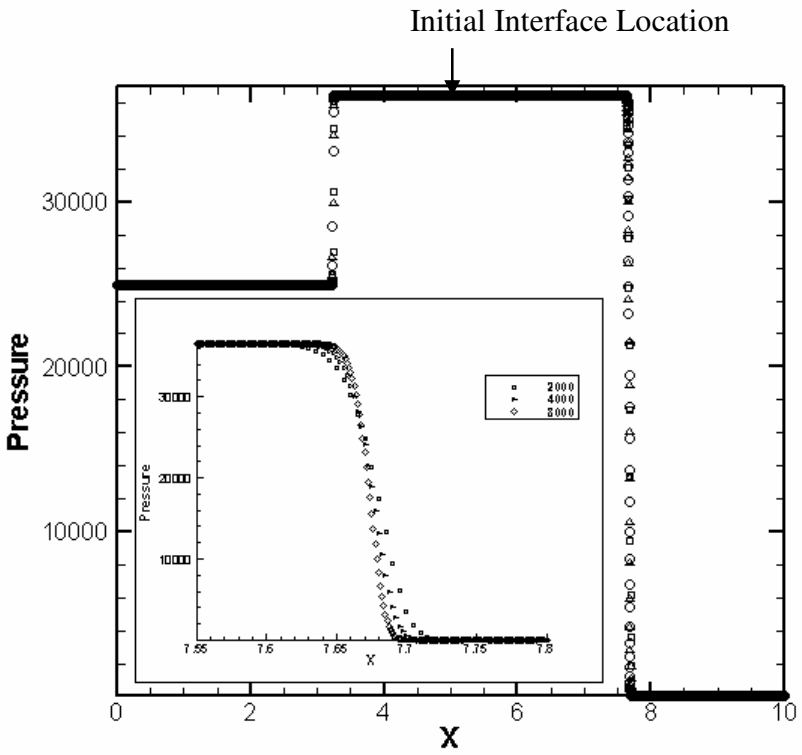

Figure 4-13: Mesh refinement of the pressure profile for water-solid (Mesh sizes: 2000, 4000, 8000)

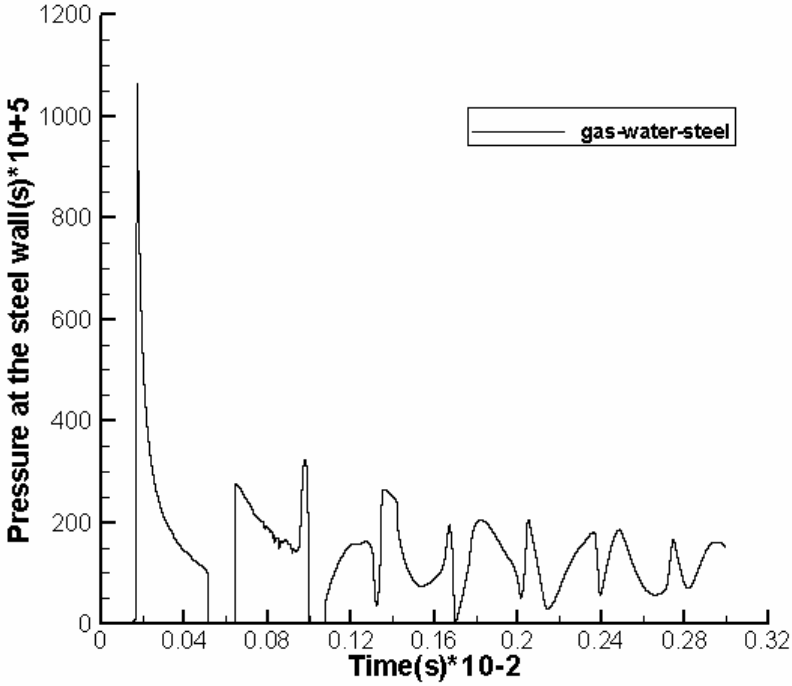

Figure 4-14a: Pressure profile at the surface of the steel wall

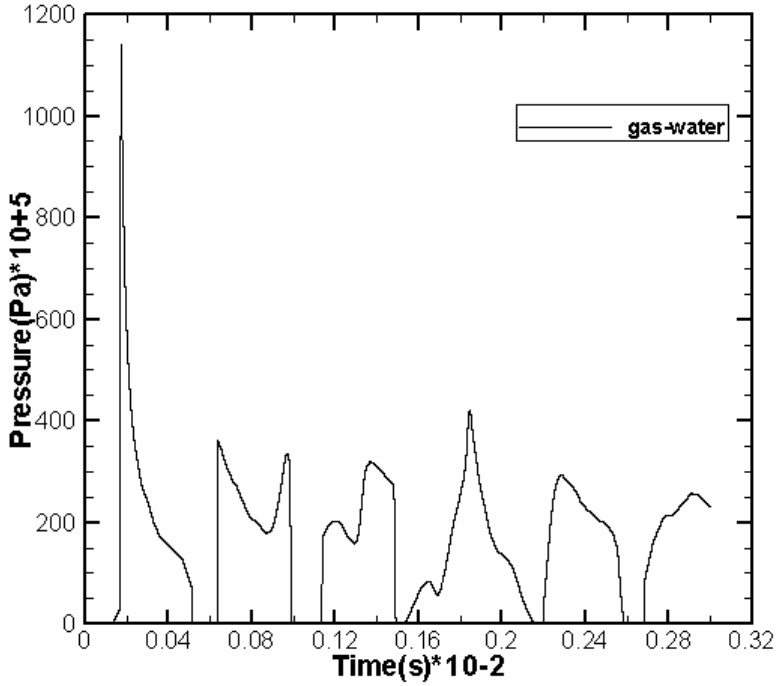

Figure 4-14b: Pressure profile at the rigid reflecting-end of tube (without steel)

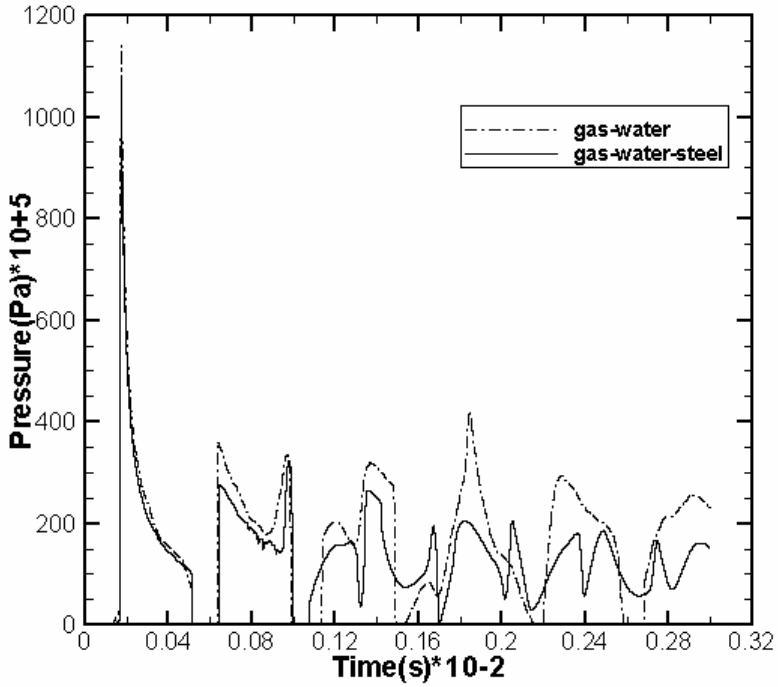

Figure 4-14c: Overlapping pressure plots for gas-water and gas-water-steel

Chapter 5 2-D Naviers Equation

5.1 General Formulation

Using the equation of motion in the absence of body forces for a volume element *V* with surface area *S*, we have

$$\vec{F} = m\vec{a} \Rightarrow \nabla \cdot \vec{\sigma} = \rho \frac{\partial^2 \vec{\varepsilon}}{\partial t^2}. \tag{5.1}$$

Next, using the relationship between stress and strain in an isotropic elastic medium, we have

$$\sigma_{ij} = \lambda \Delta \delta_{ij} + 2\mu e_{ij}, \tag{5.2}$$

where Δ is the dilatational strain and is defined by $\Delta = e_{xx} + e_{yy} + e_{zz}$ and e_{ij} represents the strain in the various directions. δ_{ij} is the dirac operator in Eqn. (5.2) and is given as.

$$\delta_{ij} = \begin{cases} 0 & if\ i \neq j \\ 1 & if\ i = j \cdot \end{cases} \tag{5.3}$$

And substituting into the equation of motion yields

$$\rho \ddot{\varepsilon} = \nabla \lambda (\nabla \cdot \vec{\varepsilon}) + \nabla \mu \cdot \left[\nabla \vec{\varepsilon} + (\nabla \vec{\varepsilon})^T \right] + (\lambda + 2\mu) \nabla (\nabla \cdot \vec{\varepsilon}) - \mu \nabla \times \nabla \times \vec{\varepsilon} + \rho f \ . \tag{5.4}$$

This is the complete elastic wave equation as seen in Rawlinson N.'s lecture notes. The first two terms on the right-hand side of the above equation contain gradients of the Lame parameters. They are non-zero if the material is inhomogeneous and non-isotropic. For homogeneous, isotropic medium, the elastic wave equation reduces to the general Naviers equation.

$$(\lambda + 2\mu) \nabla (\nabla \cdot \vec{\varepsilon}) - \mu \nabla \times (\nabla \times \vec{\varepsilon}) - \rho \frac{\partial^2 \vec{\varepsilon}}{\partial t^2} + \rho f = 0 . \tag{5.5}$$

5.2 Specific 2-D formulation

In textbooks such as Filonenko-Borodich (1968) , the two-dimensional form of the Naviers equation for elastic solids is expressed in the form given as:

$$\rho\frac{\partial^2\varepsilon_1}{\partial t^2}=(\lambda+2\mu)\frac{\partial^2\varepsilon_1}{\partial x^2}+\mu\frac{\partial^2\varepsilon_1}{\partial y^2}+(\lambda+\mu)\frac{\partial^2\varepsilon_2}{\partial x\partial y}+\rho F_1, \tag{5.6a}$$

$$\rho\frac{\partial^2\varepsilon_2}{\partial t^2}=(\lambda+2\mu)\frac{\partial^2\varepsilon_2}{\partial y^2}+\mu\frac{\partial^2\varepsilon_2}{\partial x^2}+(\lambda+\mu)\frac{\partial^2\varepsilon_1}{\partial x\partial y}+\rho F_2, \tag{5.6b}$$

where ε_1 is the displacement in the x-direction and ε_2 is the displacement in the y-direction and F_1 and F_2 are the respective body force in the x and y direction. The body forces are considered negligible in our derivation. Through some simple mathematical manipulation, we have

$$\begin{cases}\dfrac{\partial^2\varepsilon_1}{\partial t^2}=\alpha^2\dfrac{\partial^2\varepsilon_1}{\partial x^2}+(\alpha^2-\beta^2)\dfrac{\partial^2\varepsilon_2}{\partial x\partial y}+\beta^2\dfrac{\partial^2\varepsilon_1}{\partial y^2}, & (5.7a)\\ \dfrac{\partial^2\varepsilon_2}{\partial t^2}=\beta^2\dfrac{\partial^2\varepsilon_2}{\partial x^2}+(\alpha^2-\beta^2)\dfrac{\partial^2\varepsilon_1}{\partial x\partial y}+\alpha^2\dfrac{\partial^2\varepsilon_2}{\partial y^2}, & (5.7b)\end{cases}$$

where

$$\alpha=\sqrt{\frac{2\mu+\lambda}{\rho}}\ ,\ \beta=\sqrt{\frac{\mu}{\rho}}\ . \tag{5.8}$$

So we can also express the equation in terms of velocity-stress via the following relations between displacement and velocity,

$$u=\frac{\partial\varepsilon_1}{\partial t},\ V=\frac{\partial\varepsilon_2}{\partial t}\ . \tag{5.9}$$

The Naviers equations are actually obtained from Newton's 2nd law and the stress-strain relationships. α and β are the compressional or longitudinal and shear wave speeds respectively. In geophysics, they are termed as the P-wave and S-wave, respectively. For the P-wave, the displacements occur along the direction of

propagation whereas for an S-wave, the displacements occur perpendicular to the direction of propagation.

When Newton's 2nd law: ($\vec{F} = m\vec{a}$) is applied to the isotropic, homogeneous solid material, we have

$$\begin{cases} \rho \dfrac{\partial^2 \varepsilon_1}{\partial t^2} = \dfrac{\partial \sigma_{xx}}{\partial x} + \dfrac{\partial \sigma_{xy}}{\partial y}, & (5.10a) \\ \rho \dfrac{\partial^2 \varepsilon_2}{\partial t^2} = \dfrac{\partial \sigma_{xy}}{\partial x} + \dfrac{\partial \sigma_{yy}}{\partial y}. & (5.10b) \end{cases}$$

In many engineering applications, complex three-dimensional problems may be simplified to two-dimensional or plane problems. There are the usual two types of plane problems: plane stress or plane strain.

In the case of plane stress, one of the dimensions is much smaller compared with the other dimensions and we can then assume that the stress in the direction of the small dimension is negligible. Thus, we can simply ignore the 'small' dimension and perform our analysis for the two-dimensional plane of the larger dimensions only (Fig. 5-1(a)). From Chung (1996), $\sigma_{xz} = 0, \sigma_{yz} = 0, \sigma_{zz} = 0, \dfrac{\partial \varepsilon_3}{\partial z} \neq 0$. (5.11)

For plane strain, one dimension is extremely large in comparison with the other two dimensions and hence, it is possible that the strain in this direction is negligible. We may then perform two-dimensional analysis on a sliced plane with unit thickness along the axis of the extremely large dimension as seen in Fig. 5-1(b). In mathematical terms,

$$\frac{\partial \varepsilon_3}{\partial x} = 0, \frac{\partial \varepsilon_3}{\partial y} = 0, \frac{\partial \varepsilon_3}{\partial z} = 0, \sigma_{zz} \neq 0.$$

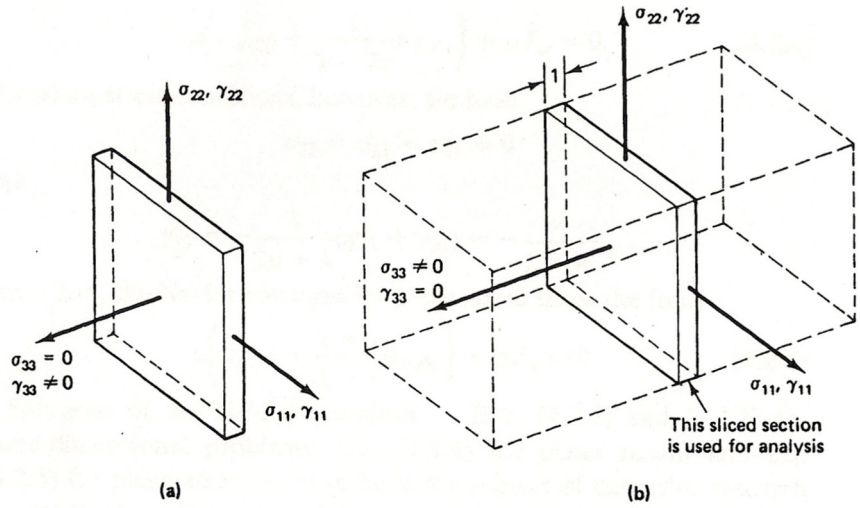

Figure 5-1(a): Plane stress, (b): Plane Strain

For plane strain conditions, the stress-strain relations are given by:

$$\begin{bmatrix} \sigma_{xx} \\ \sigma_{yy} \\ \sigma_{xy} \end{bmatrix} = \frac{E(1-\upsilon)}{(1+\upsilon)(1-2\upsilon)} \begin{bmatrix} 1 & \frac{\upsilon}{1-\upsilon} & 0 \\ \frac{\upsilon}{1-\upsilon} & 1 & 0 \\ 0 & 0 & \frac{1-2\upsilon}{2(1-\upsilon)} \end{bmatrix} \begin{bmatrix} e_{xx} \\ e_{yy} \\ e_{xy} \end{bmatrix} \tag{5.12}$$

Using Cauchy's equations which give the relation between displacements and strains, we can then determine the stress-displacement relations from Filonenko-Borodich (1968),

$$\begin{cases} e_{xx} = \dfrac{\partial \varepsilon_1}{\partial x}, & (5.13a) \\ e_{yy} = \dfrac{\partial \varepsilon_2}{\partial y}, & (5.13b) \\ e_{xy} = \dfrac{\partial \varepsilon_2}{\partial x} + \dfrac{\partial \varepsilon_1}{\partial y}. & (5.13c) \end{cases}$$

Thus, the stress-displacement relations for plane strain are given by

$$\begin{bmatrix}\sigma_{xx}\\ \sigma_{yy}\\ \sigma_{xy}\end{bmatrix}=\frac{E(1-\upsilon)}{(1+\upsilon)(1-2\upsilon)}\begin{bmatrix}1 & \frac{\upsilon}{1-\upsilon} & 0\\ \frac{\upsilon}{1-\upsilon} & 1 & 0\\ 0 & 0 & \frac{1-2\upsilon}{2(1-\upsilon)}\end{bmatrix}\begin{bmatrix}\frac{\partial\varepsilon_1}{\partial x}\\ \frac{\partial\varepsilon_2}{\partial y}\\ \frac{\partial\varepsilon_1}{\partial y}+\frac{\partial\varepsilon_2}{\partial x}\end{bmatrix}. \tag{5.14}$$

Combining with the definitions of Lame constants in Eqns. (3.7), the stress-displacement relations can be written with just the Lame constants as

$$\begin{cases}\sigma_{xx}=(\lambda+2\mu)\frac{\partial\varepsilon_1}{\partial x}+\lambda\frac{\partial\varepsilon_2}{\partial y}\Rightarrow\frac{\partial\sigma_{xx}}{\partial t}=\alpha^2\frac{\partial(\rho u)}{\partial x}+(\alpha^2-2\beta^2)\frac{\partial(\rho V)}{\partial y}, & (5.15a)\\ \sigma_{yy}=\lambda\frac{\partial\varepsilon_1}{\partial x}+(\lambda+2\mu)\frac{\partial\varepsilon_2}{\partial y}\Rightarrow\frac{\partial\sigma_{yy}}{\partial t}=(\alpha^2-2\beta^2)\frac{\partial(\rho u)}{\partial x}+\alpha^2\frac{\partial(\rho V)}{\partial y}, & (5.15b)\\ \sigma_{xy}=\mu\left(\frac{\partial\varepsilon_1}{\partial y}+\frac{\partial\varepsilon_2}{\partial x}\right)\Rightarrow\frac{\partial\sigma_{xy}}{\partial t}=\beta^2\left(\frac{\partial(\rho u)}{\partial y}+\frac{\partial(\rho V)}{\partial x}\right). & (5.15c)\end{cases}$$

By substituting Eqns. (5.15a) to (5.15c) into Eqns. (5.10a) and (5.10b), we can derive the concise form of the Naviers equations as seen in Eqns. (5.7a) and (5.7b) and noted by Toro and Clarke (1998).

The same approach in defining the Euler equations for fluid media is applied to the Naviers equations. Here, the Naviers equations are formulated in a quasi-linear form. Similarly to the Euler equations, the Naviers equations contain only first-order derivatives and hence the system is first order in the variables *U* where *U* is defined below.

In the explicit form, the quasi-linear form of equations is written as

$$\frac{\partial U}{\partial t}=\left(\frac{\partial\vec{F}}{\partial U}\right)\cdot\nabla\vec{U}+Q,\qquad\vec{F}=(f,g)^T, \tag{5.16}$$

$$\frac{\partial U}{\partial t}=\frac{\partial f}{\partial x}+\frac{\partial g}{\partial y}+Q. \tag{5.17}$$

Here Q is the source term and is equivalent to zero in the case of the homogeneous 2D Naviers equations. The flux vector $\vec{F}$ is also defined in such a way that the flux components are homogeneous functions of the conservative variables in *U*.

This meant that the flux components can be decomposed into

$$f = AU, \qquad g = BU\ , \tag{5.18}$$

where A and B are the two Jacobian matrices of the flux vector.

Hence, the equations can be written as

$$\frac{\partial U}{\partial t} = A\frac{\partial U}{\partial x} + B\frac{\partial U}{\partial y}, \tag{5.19}$$

Where $U = \left(\rho u,\ \rho V,\ \sigma_{xx},\ \sigma_{yy},\ \sigma_{xy}\right)^T$ and $f = \left[\sigma_{xx},\ \sigma_{xy},\ \alpha^2\rho u,\ \left(\alpha^2 - 2\beta^2\right)\rho u,\ \beta^2\rho V\right]^T$,

$g = \left[\sigma_{xy},\ \sigma_{yy},\ \left(\alpha^2 - 2\beta^2\right)\rho V,\ \alpha^2\rho V,\ \beta^2\rho u\right]^T$.

The related Jacobian matrices from Toro and Clarke (1998), are thus

$$A = \frac{\partial f}{\partial U},$$

$$A = \begin{bmatrix} 0 & 0 & 1 & 0 & 0 \\ 0 & 0 & 0 & 0 & 1 \\ \alpha^2 & 0 & 0 & 0 & 0 \\ \alpha^2 - 2\beta^2 & 0 & 0 & 0 & 0 \\ 0 & \beta^2 & 0 & 0 & 0 \end{bmatrix}, \tag{5.20}$$

$$B = \frac{\partial g}{\partial U},$$

$$B = \begin{bmatrix} 0 & 0 & 0 & 0 & 1 \\ 0 & 0 & 0 & 1 & 0 \\ 0 & \alpha^2 - 2\beta^2 & 0 & 0 & 0 \\ 0 & \alpha^2 & 0 & 0 & 0 \\ \beta^2 & 0 & 0 & 0 & 0 \end{bmatrix}. \tag{5.21}$$

To determine the eigenvalues, $\left|A - \lambda I\right| = 0$ and $\left|B - \theta I\right| = 0$.

The characteristic equation for both *A* and *B* are the same. .i.e.

$$\lambda\left[\lambda^4-\left(\alpha^2+\beta^2\right)\lambda^2+\alpha^2\beta^2\right]=0, \tag{5.22}$$

Hence, the eigenvalues for both *A* and *B* are $0, \alpha, -\alpha, \beta \; or \; -\beta$. In this case, since one of the eigenvalues is zero, we are unable to derive generalized eigenvectors as was done previously for the 2D Euler equation. Instead, explicit eigenvectors for the x and y directions have to be found individually.

According to linear algebra theory, when $\lambda=0$, $AX=0$ where *X* is a 5x1 matrix and its elements are $\left[x_1,x_2,x_3,x_4,x_5\right]^T$, we have

$$\begin{bmatrix} 0 & 0 & 1 & 0 & 0 \\ 0 & 0 & 0 & 0 & 1 \\ \alpha^2 & 0 & 0 & 0 & 0 \\ \alpha^2-2\beta^2 & 0 & 0 & 0 & 0 \\ 0 & \beta^2 & 0 & 0 & 0 \end{bmatrix}\begin{bmatrix} x_1 \\ x_2 \\ x_3 \\ x_4 \\ x_5 \end{bmatrix}=0, \tag{5.23}$$

$$\begin{cases} x_3=0 \\ x_5=0 \\ \alpha^2x_1=0 \\ \left(\alpha^2-2\beta^2\right)x_1=0 \\ \beta^2x_2=0 \end{cases} \Rightarrow X=\begin{bmatrix} 0 \\ 0 \\ 0 \\ x_4 \\ 0 \end{bmatrix}. \tag{5.24}$$

With $x_4=1$, we have

$$X=\begin{bmatrix} 0 \\ 0 \\ 0 \\ 1 \\ 0 \end{bmatrix}. \tag{5.25}$$

When $\lambda\neq 0$, $A\overline{X}=0$ and hence

$$\begin{cases} \overline{x_3}=\lambda\overline{x_1}, & (5.26a) \\ \overline{x_5}=\lambda\overline{x_2}, & (5.26b) \\ \alpha^2\overline{x_1}=\lambda\overline{x_3}, & (5.26c) \\ \left(\alpha^2-2\beta^2\right)\overline{x_1}=\lambda\overline{x_4}, & (5.26d) \\ \beta^2\overline{x_2}=\lambda\overline{x_5}. & (5.26e) \end{cases}$$

From Eqn. (5.26a) and Eqn. (5.26c), $\begin{cases} \overline{x_3} = \lambda \overline{x_1} \\ \overline{x_3} = \dfrac{\alpha^2 \overline{x_1}}{\lambda} \end{cases} \Rightarrow$ these 2 equations can only be

solved when $\lambda = \pm\alpha$.

From Eqn. (5.26b) and Eqn. (5.26e), $\begin{cases} \overline{x_5} = \lambda \overline{x_2} \\ \overline{x_5} = \dfrac{\beta^2 \overline{x_2}}{\lambda} \end{cases} \Rightarrow$ these 2 equations can only be

solved when $\lambda = \pm\beta$.

Hence, when $\lambda = \alpha,\ \overline{x_2} = 0, \overline{x_5} = 0$, and we have

$$\overline{X_{\alpha+}} = \overline{x_1} \begin{bmatrix} 1 \\ 0 \\ \lambda \\ \dfrac{1}{\lambda}\left(\alpha^2 - 2\beta^2\right) \\ 0 \end{bmatrix} \Rightarrow let\ \overline{x_1} = \alpha, \quad \overline{X_{\alpha+}} = \begin{bmatrix} \alpha \\ 0 \\ \alpha^2 \\ \alpha^2 - 2\beta^2 \\ 0 \end{bmatrix}. \tag{5.27}$$

When $\lambda = -\alpha,\ \overline{x_2} = 0, \overline{x_5} = 0$, we have

$$\overline{X_{\alpha-}} = \overline{x_1} \begin{bmatrix} 1 \\ 0 \\ \lambda \\ \dfrac{1}{\lambda}\left(\alpha^2 - 2\beta^2\right) \\ 0 \end{bmatrix} \Rightarrow let\ \overline{x_1} = -\alpha, \quad \overline{X_{\alpha-}} = \begin{bmatrix} -\alpha \\ 0 \\ \alpha^2 \\ \alpha^2 - 2\beta^2 \\ 0 \end{bmatrix}. \tag{5.28}$$

When $\lambda = \beta,\ \overline{x_1} = 0, \overline{x_3} = 0 \Rightarrow \overline{x_4} = 0$, we have

$$\overline{X_{\beta+}} = \overline{x_2} \begin{bmatrix} 0 \\ 1 \\ 0 \\ 0 \\ \lambda \end{bmatrix} \Rightarrow let\ \overline{x_2} = \beta, \quad \overline{X_{\beta+}} = \begin{bmatrix} 0 \\ \beta \\ 0 \\ 0 \\ \beta^2 \end{bmatrix}. \tag{5.29}$$

When $\lambda = -\beta,\ \overline{x_1} = 0, \overline{x_3} = 0 \Rightarrow \overline{x_4} = 0$, we have

$$\overline{X_{\beta-}} = \overline{x_2}\begin{bmatrix}0\\1\\0\\0\\\lambda\end{bmatrix} \Rightarrow let\ \overline{x_2} = -\beta, \quad \overline{X_{\beta-}} = \begin{bmatrix}0\\-\beta\\0\\0\\\beta^2\end{bmatrix}. \tag{5.30}$$

Therefore, the right eigenvector of *A* is determined as

$$R_A = \begin{bmatrix}0 & \alpha & -\alpha & 0 & 0\\ 0 & 0 & 0 & \beta & -\beta\\ 0 & \alpha^2 & \alpha^2 & 0 & 0\\ 1 & \alpha^2-2\beta^2 & \alpha^2-2\beta^2 & 0 & 0\\ 0 & 0 & 0 & \beta^2 & \beta^2\end{bmatrix}. \tag{5.31}$$

In a similar manner, the right eigenvector for *B* can be determined as

$$R_B = \begin{bmatrix}0 & 0 & 0 & \beta & -\beta\\ 0 & \alpha & -\alpha & 0 & 0\\ 1 & \alpha^2-2\beta^2 & \alpha^2-2\beta^2 & 0 & 0\\ 0 & \alpha^2 & \alpha^2 & 0 & 0\\ 0 & 0 & 0 & \beta^2 & \beta^2\end{bmatrix}. \tag{5.32}$$

The left eigenvectors may be determined by finding the inverse of the right eigenvectors and given as

$$R_A^{-1} = \frac{1}{|R_A|} AdjR_A, \tag{5.33a}$$

$$AdjR_A = \begin{bmatrix}\overline{\overline{x_{11}}} & \overline{\overline{x_{12}}} & \overline{\overline{x_{13}}} & \overline{\overline{x_{14}}} & \overline{\overline{x_{15}}}\\ \overline{\overline{x_{21}}} & \overline{\overline{x_{22}}} & \overline{\overline{x_{23}}} & \overline{\overline{x_{24}}} & \overline{\overline{x_{25}}}\\ \overline{\overline{x_{31}}} & \overline{\overline{x_{32}}} & \overline{\overline{x_{33}}} & \overline{\overline{x_{34}}} & \overline{\overline{x_{35}}}\\ \overline{\overline{x_{41}}} & \overline{\overline{x_{42}}} & \overline{\overline{x_{43}}} & \overline{\overline{x_{44}}} & \overline{\overline{x_{45}}}\\ x_{51} & x_{52} & x_{53} & x_{54} & x_{55}\end{bmatrix}^T, \tag{5.33b}$$

where $\overline{\overline{x_{jk}}}$ is the cofactor given by the formula

$$\overline{\overline{x_{jk}}} = (-1)^{j+k} M_{jk}, \tag{5.33c}$$

and M_{jk} is the determinant of the sub-matrices. The left eigenvector for A is thus found to be

$$R_A^{-1} = \begin{bmatrix} 0 & 0 & -\frac{(\alpha^2-2\beta^2)}{\alpha^2} & 1 & 0 \\ \frac{1}{2\alpha} & 0 & \frac{1}{2\alpha^2} & 0 & 0 \\ -\frac{1}{2\alpha} & 0 & \frac{1}{2\alpha^2} & 0 & 0 \\ 0 & \frac{1}{2\beta} & 0 & 0 & \frac{1}{2\beta^2} \\ 0 & -\frac{1}{2\beta} & 0 & 0 & \frac{1}{2\beta^2} \end{bmatrix}. \quad (5.34)$$

And the left eignvector for B is described below as

$$R_B^{-1} = \begin{bmatrix} 0 & 0 & 1 & -\frac{(\alpha^2-2\beta^2)}{\alpha^2} & 0 \\ 0 & \frac{1}{2\alpha} & 0 & \frac{1}{2\alpha^2} & 0 \\ 0 & -\frac{1}{2\alpha} & 0 & \frac{1}{2\alpha^2} & 0 \\ \frac{1}{2\beta} & 0 & 0 & 0 & \frac{1}{2\beta^2} \\ -\frac{1}{2\beta} & 0 & 0 & 0 & \frac{1}{2\beta^2} \end{bmatrix}. \quad (5.35)$$

The variable matrix, flux matrix, left and right eigenvectors determined can thus be used in the two-dimensional MUSCL scheme for the simulation of the two-dimensional solid.

Chapter 6 Conclusion and Future Directions

6.1 Conclusion

To simulate the shock-cavitation interaction with solid structure, Naviers equation was used to model the structure rather than any of the existing solid EOS such as Mie-Gruneisen EOS which has been utilized quite extensively in the simulation of solid material as attested by Miller and Puckett (1996) and the hydro-elasto-plastic solid model in Tang and Sotiropoulos (1999). Naviers equation is based on structural mechanics involving elastic continuum and constitutive stress-strain relations. The only material parameters required are the Young's Modulus and the Poisson Ratio which are common parameters available in material handbooks. No other experimental material parameters are needed and this makes the Naviers equation model very attractive to use as it can be utilized for many different materials from data already collated in handbooks. The limitations would be problems involving large deformations of the solid, and also problems involving plastic flow whereby due to the non-linear constitutive stress-strain relations, the system of governing equations becomes non-linear as well.

Though there were many models using the Naviers equation, this is the first time that the Naviers equation model is used to simulate shock-cavitation interaction between a fluid and solid media. This novel approach also uses the Modified Ghost Fluid method which is based on the approximate Riemann problem solver at the fluid-solid interface and tracked using the Level Set method. The MUSCL scheme which is a high order, upwind scheme, is used for both the fluid and solid solver. The analytical solutions for the 1D test cases were also derived for the first time using Euler equation for the fluid and Naviers equation for the solid media. From the test cases 4.3 and 4.4 which are

typical shock impedance tests, the smooth transition at the fluid-solid interface indicates that the interface solver developed in this thesis has accurately dealt with the 1D interface characteristics. The results of various other test cases involving shock-shock, rarefraction-shock and rarefraction-rarefraction interaction were also shown and discussed. The 1D numerical solutions for majority of the cases fit very well with the analytical solutions with a few exceptions in cases 4.7 and 4.11. In test cases 4.7 and 4.11, rarefraction waves occur in both the fluid and solid medium. However, pressure undershoots are seen near the solid rarefraction wave in both test cases. From Lin and Ballmann (1993a), the solid rarefraction wave comes from a family of centered plastic waves and the authors were able to successfully simulate the rarefraction waves in the solid media by solving the Riemann Problem for the waves. This could mean that plasticity effects have to be considered in modeling the rarefraction waves in solid materials. In the test case 4.14, the results from the gas-water-steel cavitation interaction show similar general effects as Wardlaw et al. (2000) in the comparisons between deformable and rigid walls. In our results, it is noted that the pressure pulses drop to a lower mean value compared to the case with rigid boundary, though the magnitude of the drop may not be the same as for the 3D experimental results used in the paper. Also, there appear to be less number of cavitation zones in the case with steel structure. However, as the simulations here are only one-dimensional and can only reflect a limited behaviour, the extension to multi-dimensions would be required to further validate the one-dimensional results. The formulation of the eigensystem of the re-written Naviers equation in two dimensions was also achieved in this thesis.

6.2 Future directions

The next area of work would be extending the 1D methodology to multi-dimensions. Even though the mathematical formulae for the two-dimensional Naviers equation has been worked out, more work still needs to be done in solving the Approximate Riemann problem at the interface and working out any Eulerian-Lagrangian mesh problems. Another possible area to work on would be the consideration of plasticity effects, in which case, the linear Naviers equation would not be suitable for use as the plasticity effects are often non-linear. Instead, the non-linear form of the Naviers equation would have to be used and further mathematical treatment is needed to express the non-linear equation in eigensystem form.

References

Aanhold van J.E., Meijer G.J. and Lemmen P.P.M., "Underwater shock response analysis of a floating vessel," Shock and Vibration, Vol. 5, pp. 53-59, 1998

Allaire G., Clerc S. and Kokh S., "A five-equation model for the simulation of interfaces between compressible fluids," J. Comput. Physics, Vol. 181, pp. 577-616, 2002

Ashgriz N., Poo J. Y., "FLAIR: Flux Line-Segment Model for Advection and Interface Reconstruction", J. Comput. Physics, Vol. 92, pp. 449, 1991

Benson D., "A new two-dimensional flux-limited shock viscosity for impact calculations," Comput. Methods Appl. Mech. Eng.,Vol. 93, pp. 39, 1991

Benson D., "Computational methods in Lagrangian and Eulerian hydrocodes," Comput. Methods Appl. Mech. Eng., Vol. 99, pp. 235, 1992

Bose Roy P. and Bose Roy S., "An isothermal equation of state for solids," Physica B, Vol. 350, pp. 375, 2004

Chen S., Merriman B., Osher S., and Smereka P., "A simple level set method for solving Stefan problems", J. Comput. Physics, Vol. 134**,** 1997

Cohen G., Halpern L. and Joly P., "Mathematical and numerical aspects of wave propagation phenomena," Society for Industrial and Applied Mathematics, pp.190-198, 1991

Chung T.J., "Applied continuum mechanics", Cambridge University Press, pp. 112-114, 1996

Davis J.R, "Concise Metals Engineering Data Book", ASM International, pp. 48-124, 1997

Fedkiw R.P., Aslam T., Merriman B., Osher S., "A non-oscillatory Eulerian approach to interfaces in multimaterial flows(the Ghost Fluid Method)", J. Comput. Physics, Vol. 152, pp. 457-492, 1999

Fedkiw R.P., "Coupling an Eulerian Fluid Calculation to a Lagrangian Solid Calculation
with the Ghost Fluid Method", Journal of Computational Physics, Vol. 175, pp. 200-224, 2002

Filonenko-Borodich M., "Theory of Elasticity", MIP Publishers, pp. 94, 1968

Flores J. and Holt M., "Glimm's method applied to underwater explosions", J. Comp. Phys., Vol. 44, pp. 377-387, 1981

Giese G. and Fey M., “A dynamic high-resolution simulation of 2D elastic-plastic crack problems”, Computational Mechanics, Vol. 34, pp. 503-509, 2004

Harten A., “High resolution schemes for hyperbolic conservation laws”, J. Comp. Physics, Vol. 49, pp. 357-393, 1983

Harten A., Engqust B., Osher S. and Chakaravarthy S.R., “Some results on uniformly high-order accurate essentially non-oscillatory schemes”, J. Appl. Num. Math, Vol. 24, pp. 347-377, 1986

Harten A., Engqust B., Osher S. and Chakaravarthy S.R., “Uniformly high order accurate essentially non-oscillatory scheme III”, J. Comp. Physics, Vol. 71, pp. 231-303, 1987

Harten A., “ENO schemes with subcell resolution”, J. Comp. Physics, Vol. 83, pp. 148-184, 1989

He X., Chen S., Zhang R., “A Lattice–Boltzmann scheme for incompressible multiphase flow and its application in simulation of Rayleigh–Taylor instability”, J. Comput. Physics, Vol. 152, pp. 642, 1999

Hirsch C., “Numerical computation of internal and external flows”, Vol.2, John Wiley & Sons Ltd, pp. 204, 1992

Hirt C. W., Nicholas B. D., “Calculating three-dimensional free surface flows in a vicinity of submerged and exposed structures”, J.Comput. Physics, Vol. 12, pp. 234, 1973

Hirt C.W. and Nichols B.D., “Volume of fluid(VOF) method for the dynamics of free boundaries”, J. Comp. Physics, Vol. 39, pp.201, 1981

Kobayashi R., “Modeling and numerical simulation of dendritic crystal growth”, Physica D, Vol. 63, pp. 410, 1993

Kochupillai J., Ganesan N., Padmanabhan C., “A new finite element formulation based on the velocity of flow for water hammer problems”, Int. J. Pressure Vessels and Piping, pg. 1-14, 2004

Lin X. and Ballmann J., “A Riemann solver and a Second-Order Godunov method for Elastic-Plastic wave propagation in solids”, Int. Journal of Impact Engineering, Vol. 13, No. 3, pp. 463-478, 1993a

Lin X. and Ballmann J., “Numerical method for elastic-plastic waves in cracked solids”, Archive of Applied Mechanics Vol. 63, pp.261–282 and pp. 283–295, 1993b

Lin X. and Ballmann J., “Reconsideration of Chen’s problem by finite difference method”, Engineering Fracture and Mechanics Vol 44, No.5, pp.735–739, 1993c

Liu T.G., Khoo B.C. and Yeo K.S., "The Numerical Simulations of Explosion and Implosion in Air: Use of a Modified Harten's TVD Scheme", International Journal For Numerical Methods in Fluids, Vol. 31, pp 661-680, 1999

Liu T.G., Khoo B.C. and Yeo K.S., "The simulation of compressible multi-medium flow I: A new methodology with test applications to 1D gas-gas and gas-water cases," Computers & Fluids, Vol. 30, pp. 291-314, 2001

Liu T.G., Khoo B.C. and Yeo K.S, "Ghost fluid method for strong shock impacting on material interface", J. Comp. Physics, Vol. 190, pp. 651-681, 2003

Liu T.G., Khoo B.C. and Xie W.F., "Isentropic one-fluid modeling of unsteady cavitating flow," J. Comput. Physics, Vol. 201, pp. 80-108, 2004

Liu T.G., Khoo B.C. and Wang C.W., "The ghost fluid method for compressible gas–water simulation," J. Comput. Physics, Vol. 204, pp. 193-221, 2005

Miller G.H. and Puckett E.G., "A high-order Godunov method for multiple condensed phases", Journal of Computational Physics, Vol. 128, pp. 134, 1996

Minkoff S.E., "Spatial parallelism of a 3D finite difference velocity-stress elastic wave propagation code," SIAM J. Sci. Comput., Vol. 24, No. 1, pp. 1-19, 2002

Noh W. and Woodward P., "SLIC(Simple Line Interface Calculation)" from the Proceedings of the 5th International Conference on Fluid Dynamics, Lecture Notes in Physics, Vol. 59, Springer, Berlin, pp.330, 1976

Osher S. and Sethian J.A., "Fronts propagating with curvature-dependent speed: algorithms based on Hamilton-Jacobi formulations", J. Comp. Physics, Vol. 79, pp. 12-49, 1988

Owis F.M. and Nayfeh A.H., "Numerical simulation of 3-D incompressible, multi-phase flows over cavitating projectiles", European Journal of Mechanics B/Fluids, Vol. 23, pp. 339-351, 2004

Qin J.R., Yu S.T.J. and Lai M.C., "Direct calculations of cavitating flows in fuel delivery pipe by the Space-Time CE/SE method," Society of Automotive Engineer, 1999-01-3554, 1999

Rawlinson N., Lecture notes on Seismology and seismic imaging: 3.The elastic wave equation, Research school of Earth Sciences, ANU, http://rses.anu.edu.au/~nick/teachdoc/lecture3.pdf#search='elastic%20wave%20equation'

Rudman M., "A volume tracking method for incompressible multifluid flows with large density variations", Int. J. Numerical Methods in Fluids, Vol. 28, pp. 357, 1998

Saurel R. and Abgrall R., "A multiphase Godunov method for compressible multifluid and multiphase flows," J. Comput. Physics, Vol. 150, pp. 425-467, 1999a

Saurel R. and Abgrall R., “A simple method for compressible multifluid flows”, SIAM J. Sci. Comput., Vol 21, No. 3, pp. 1115, 1999b

Schmidt D.P., Rutland C.J. and Corradini M.L., “A fully compressible, two-dimensional model of small, high speed, cavitating nozzles,” Atomization Sprays, Vol. 9, pp. 255-276, 1999

Sethian J.A., “Level-Set methods: evolving interfaces in geometry, fluid mechanics, computer vision and materials science”, Cambridge Univ. Press., pp. 25-32, 1996

Shyue K.M., “An efficient shock-capturing algorithm for compressible multicomponent problems”, J. Comput. Physics, Vol. 142, pp. 208, 1998

Takano Y., Hayashi K., Goto T., “A computational procedure for interaction of shock waves with solid materials in liquid.” Houwing AFP (ed) Proceedings of 21st International Symposium on Shock Waves (Great Keppel Island, Australia, July 20–25, 1997). Panther Publishing, vol. 2, pp. 1039–1044, 1997a

Takano Y., Hayashi K., Goto T., “Simulations for stress waves induced in solid material by reflection of strong shock waves.” Proceedings of JSME Centennial Grand Congress, International Conference of Fluid Engineering,Tokyo, Japan, July 13–16, 1997, pp. 413–416, 1997b

TakanoY., Mizushiri Y., GotoT., “Stress waves induced in an acrylic block by shock waves.” Ball GJ, Hillier R, Roberts GT (eds) ”Shock Waves”, Proc. of the 22nd Int. Symp. on Shock Waves (London, UK, 18-23 July, 1999). University of Southhampton, vol.2, pp. 1399–1404, 1999

Tang H.S. and Huang D., “A second-order accurate capturing scheme for 1D inviscid flows of gas and water with vacuum zones,” J. Comput. Physics, Vol. 128, pp. 301-318, 1996

Tang H.S. and Sotiropoulos F., “A Second-Order Godunov Method for Wave Problems in Coupled Solid-water-gas systems”, Journal of Computational Physics, Vol. 151, pp. 790-815, 1999

Toro E.F., “Riemann solvers and numerical methods for fluid dynamics”, Springer-Verlag Berlin Heidelberg, pp. 70-76, 1997

Toro E.F. and Clarke J.F., “Numerical Methods for wave propagation”, Fluid Mechanics and Its Applications, Vol. 47, pp. 197-210, 1998

Udaykumar H.S., Tran L., Belk D.M., Vanden K.J., “An Eulerian method for computation of multimaterial impact with ENO shock-capturing and sharp interfaces”, J. Comput. Physics, Vol. 186, pp. 136-177, 2003

Van Leer B., “Towards the ultimate conservative difference scheme V: A second0order sequel to Godunov’s method”, J. Comp. Physics, Vol. 32, pp. 101-136, 1979

Ventikos Y. and Tzabiras G., “A numerical method for the simulation of steady and unsteady cavitating flows”, Computers & Fluids, Vol. 29, pp. 63-88, 2000
Knapp R.T., Daily J.W. and Hammit F.G., “Cavitation”, McGraw-Hill, pp. 1-2,1970

Voller V.R. and Prakash C., “A fixed grid numerical modeling methodology for convection-diffusion mushy region phase-change problems”, Int. J. Heat Mass Transfer, Vol. 30, pp. 1709, 1987

Voinovich P., Merlen A., Timofeev E., Takayama K., “A Godunov-type finite-volume scheme for unified solid-liquid elastodynamics on arbitrary two-dimensional grids”, Shock Waves Vol. 13, pp. 221-230, 2003

Wardlaw A.B., Alan Luton J. and Jr., “Fluid-structure interaction mechanisms for close-in explosions”, Shock and Vibration Vol 7, pp.265-275, 2000

Xie W.F., Liu T.G. and Khoo B.C., “Application of a One-Fluid model for large scale homogeneous unsteady cavitation: the modified Schmidt’s model”, Computers & Fluids, In Press, 2005